Helsinki University of Technology Control Engineering

Espoo 2009 Report 160

MACHINE VISION IN MEASUREMENT AND CONTROL OF MINERAL CONCENTRATION PROCESS

Jani Kaartinen

TEKNILLINEN KORKEAKOULU
TEKNISKA HÖGSKOLAN
HELSINKI UNIVERSITY OF TECHNOLOGY
TECHNISCHE UNIVERSITÄT HELSINKI
UNIVERSITE DE TECHNOLOGIE D´HELSINKI

Helsinki University of Technology Control Engineering

Espoo June 2009 Report 160

MACHINE VISION IN MEASUREMENT AND CONTROL OF MINERAL CONCENTRATION PROCESS

Jani Kaartinen

Dissertation for the degree of Doctor of Science in Technology to be presented with due permission of the Faculty of Electronics, Communications and Automation, for public examination and debate in Auditorium AS1 at Helsinki University of Technology (Espoo, Finland) on the 26th of June, 2009, at 12 noon.

Helsinki University of Technology

Faculty of Electronics, Communications and Automation

Department of Automation and Systems Technology

Distribution:
Helsinki University of Technology
Department of Automation and Systems Technology
P.O. Box 5500
FI-02015 TKK, Finland
Tel. +358-9-451 5201
Fax. +358-9-451 5208
E-mail: control.engineering@tkk.fi
http://autsys.tkk.fi/

ISBN 978-951-22-9954-6 (printed)
ISBN 978-951-22-9955-3 (pdf)
ISSN 0356-0872

Yliopistopaino
Helsinki 2009

Available on net at http://lib.tkk.fi/Diss/2009/isbn9789512299553

ABSTRACT OF DOCTORAL DISSERTATION

HELSINKI UNIVERSITY OF TECHNOLOGY
P.O. BOX 1000, FI-02015 TKK
http://www.tkk.fi

Author Jani Kaartinen

Name of the dissertation
Machine Vision in Measurement and Control of Mineral Concentration Process

Manuscript submitted February 27, 2009 | Manuscript revised May 28, 2009

Date of the defence June 26, 2009

☐ Monograph | ☒ Article dissertation (summary + original articles)

Faculty Faculty of Electronics, Communications and Automation
Department Department of Automation and Systems Technology
Field of research Control Engineering
Opponent(s) Prof. Sirish Shah, Prof. Raimo Ylinen
Supervisor Prof. Heikki Koivo
Instructor Prof. Heikki Hyötyniemi

Abstract

This thesis considers machine vision in the context of the mining, mineral and metal industry (MMMI). Even though MMMI might be seen as a rather conservative industry branch, in many cases it is not. One motivation for constant research and development is the large amount of ore processed on a yearly basis, which means that even a slight improvement in performance can lead to substantial economical benefits. Another point, related more closely to the thesis, is that the development in camera and information technology has enabled the integration of machine vision based applications into many different industry branches, MMMI being one of them.

Machine vision and its utilization in measurement and control of a modern flotation plant is studied in detail. The research was started in the late 90's with the development of an image analysis platform for flotation froths, which was later extended to cover multiple flotation cells. The resulting image analysis based variables were studied and new results regarding their usefulness both in single and multi-camera settings were obtained. The most important variables are shown to the plant operators and used in closed loop control. Furthermore, an image history database and a tool for its utilization were created, as well as a new type of froth level measurement technique introduced.

The research done with the image analysis of flotation froths provided strong evidence of the importance of the froth colour as an indicator of grade. This motivated further studies carried out with a spectrophotometer, which is a more accurate instrument for colour measurements. As a result, a new type of on-line measurement technique was created to be used as a supplement to existing X-Ray fluorescence (XRF) analyzers to reduce their typical sampling interval of 10-20 minutes to a virtually continuous measurement.

Another field of research presented is the particle size distribution analysis of crushed ore from a moving conveyor belt in a contact-free manner, for which two new measurement techniques are presented. This information, when measured already in the mine, can be used in the flotation plant to gain better grinding results, and geologists can use it in mine planning.

Keywords machine vision, mine, mining, flotation, control

ISBN (printed) 978-951-22-9954-6 | ISSN (printed) 0356-0872

ISBN (pdf) 978-951-22-9955-3 | ISSN (pdf)

Language English | Number of pages 111 + 87

Publisher Helsinki University of Technology, Department of Automation and Systems Technology

Print distribution Helsinki University of Technology, Department of Automation and Systems Technology

☒ The dissertation can be read at http://lib.tkk.fi/Diss/

VÄITÖSKIRJAN TIIVISTELMÄ	TEKNILLINEN KORKEAKOULU PL 1000, 02015 TKK http://www.tkk.fi

Tekijä Jani Kaartinen

Väitöskirjan nimi
Konenäkö mineraalien rikastusprosessin mittauksessa ja säädössä

Käsikirjoituksen päivämäärä 27.2.2009	Korjatun käsikirjoituksen päivämäärä 28.5.2009

Väitöstilaisuuden ajankohta 26.6.2009

☐ Monografia	☒ Yhdistelmäväitöskirja (yhteenveto + erillisartikkelit)

Tiedekunta	Elektroniikan, tietoliikenteen ja automaation tiedekunta
Laitos	Automaatio- ja systeemitekniikan laitos
Tutkimusala	Systeemitekniikka
Vastaväittäjä(t)	Prof. Sirish Shah, Prof. Raimo Ylinen
Työn valvoja	Prof. Heikki Koivo
Työn ohjaaja	Prof. Heikki Hyötyniemi

Tiivistelmä

Tämä väitöskirja käsittelee konenäköä ja sen hyödyntämistä kaivos- ja rikastusprosesseissa. Vaikka tämän tyyppiset prosessit usein mielletäänkin melko konservatiivisiksi, todellisuudessa niissä usein tehdään jatkuvaa tutkimus- ja tuotekehitystyötä. Luonnollinen motiivi tähän on raha; vuositasolla prosessoidut malmimäärät ovat tyypillisesti niin suuria, että jo pienelläkin suorituskyvyn suhteellisella parannuksella on suuri taloudellinen merkitys. Toinen, lähemmin tähän väitöskirjaan liittyvä asia, on kamera- ja informaatioteknologioiden kehitys, jonka ansiosta konenäkösovelluksia voidaan hyödyntää yhä useammassa teollisuuden haarassa.

Työssä tutkitaan erityisesti konenäön hyödyntämistä modernin rikastusprosessin mittauksen ja säädön kannalta. Tutkimus alkoi 90-luvun lopulla erityisen vaahdotusprosessin rikastusvaahtojen monitorointiin ja mittaamiseen tarkoitetun konenäköalustan kehitystyöllä. Alusta kehitettiin aluksi yhteen rikastuskennoon ja laajennettiin myöhemmin kattamaan useita kennoja. Näin saatuja vaahdotusprosessia kuvaavia suureita sekä niiden hyödynnettävyyttä tutkittiin sekä yksi- että monikameraympäristössä. Tärkeimmiksi havaittuja suureita hyödynnetään valvomossa tehtaan operaattoreiden toimesta, sekä suljetussa säädössä. Lisäksi työssä luotiin erillinen kuvahistoriatietokanta ja työkalut sen hyödyntämiseksi valvomossa, sekä uuden tyyppinen vaahtopinnan korkeusmittaus.

Vaahtoihin liittynyt konenäkötutkimus osoitti, että vaahdon väri indikoi pitoisuutta. Tämän johdosta väriin liittyvää tutkimusta jatkettiin kameran sijaan spektrofotometrilla, joka on erityisesti värin mittaamiseen tarkoitettu instrumentti. Tämä tutkimus johti uudentyyppiseen mittaustekniikkaan, joka voidaan liittää osaksi olemasssa olevia röntgenfluoresenssi (XRF)-analysaattoreita. Tuloksena on, että XRF-analysaattoreiden tyypillinen 10-20 minuutin mittausväli voidaan lyhentää käytännössä nollaan, jatkuvaksi mittaukseksi.

Toinen väitöskirjassa käsitelty tutkimusala on kuljetinhihnalta tehtävä kosketukseton murskatun malmin raekokojakaumamittaus. Tämän toteuttamiseksi työssä esitetään kaksi uutta mittaustekniikkaa. Jos mittaus tehdään jo kaivoksessa, niin sen avulla saatavaa jakaumatietoa voidaan hyödyntää rikastamon jauhatustulosten parantamisessa, sekä geologien toimesta louhinnan suunnittelussa.

Asiasanat konenäkö, kaivos, louhinta, vaahdotus, säätö

ISBN (painettu) 978-951-22-9954-6	ISSN (painettu) 0356-0872
ISBN (pdf) 978-951-22-9955-3	ISSN (pdf)
Kieli Englanti	Sivumäärä 111 + 87

Julkaisija Teknillinen korkeakoulu, Automaatio- ja systeemitekniikan laitos

Painetun väitöskirjan jakelu Teknillinen korkeakoulu, Automaatio- ja systeemitekniikan laitos

☒ Luettavissa verkossa osoitteessa http://lib.tkk.fi/Diss/

Q: "When is your thesis going to be ready?"

A: "I've been having some printing problems..."

Preface

In the spring of 1999 I started as a research assistant in the Control Engineering Laboratory, now called the Control Engineering Research Group. The first project I got to choose to be assigned to was the EU funded ChaCo-project that had started few years earlier and was dealing with utilization of machine vision in the context of mineral flotation. This seemed like an interesting research topic – and when Jean-Peter Ylén (who was interviewing me) mentioned that "furthermore, you get to travel a lot" – I was sold. Had I chosen another topic, this thesis would not have been made, not in this form at least.

The research was carried out under supervision of Professor Heikki Koivo, to whom I am grateful for so many things. I guess that the most important one is his "way of doing business", meaning that the atmosphere is always relaxed and inspiring, and that he is always on a good mood (which catches to others also). Professor Heikki Hyötyniemi contributed also greatly to this thesis, especially in the early phases of the work. Other important contributors from the lab (past and present) are: Dr. Jari Hätönen, Dr. Vesa Hasu, Mr. Martti Larinkari, Mr. Olli Ojala, Mr. Olli Haavisto, Mr. Timo Roine and Mr. Janne Pietilä. Another important group of people that should not go unnoticed are the members of the three shovelling teams that helped me with the "data mining" in Pyhäsalmi. They are: Martti L., Olli O., Mikael M., Antti H., Kalle K., Olli H., Timo R., Janne P. and Antti T. Thanks a lot guys!

Furthermore, I would like to thank Prof. Pentti Lautala from Tampere University of Technology and Prof. Sirish Shah from the University of Alberta for a thorough pre-examination that resulted in many improvements at the final stage. Similar thanks apply also to Prof. Koivo, Prof. Hyötyniemi, Dr. Jean-Peter Ylén, Dr. Kai Zenger and to Mr. Olli Haavisto for pre-pre-examination, to Mr. Pauli Sipari for the help with the practical issues and to Mr. William Martin for proofreading the thesis.

I have been financially supported by Finnish Foundation for Technology Promotion, Walter Ahlström Foundation, Emil Aaltonen Foundation, Outokumpu Foundation and the Automation Foundation. Their support is gratefully acknowledged. Furthermore, I would like to thank The Finnish Funding Agency for Technology and Innovation (TEKES) for supporting – as it has turned out – a very fruitful cooperation between the academic and private sectors.

During the years, the level of interest and involvement from the private sector has been praiseworthy, which is mainly due to the enthusiastic people of Pyhäsalmi Mine Oy and Outotec Minerals Oy. The list would be too long to be included here, so I will mention only the key people involved with the projects and the research. They are: Mr. Seppo Lähteenmäki, Mr. Jorma Miettunen, Mr. Aki Tuikka and Mr. Jarmo Huuskonen from Pyhäsalmi Mine Oy and Dr. Kari Saloheimo and Mr. Matti Kongas from Outotec Minerals Oy.

Finally, I would like to thank my parents Jaakko and Leena, my brother Jarkko and his family, my wife Anu and our beautiful children Aleksi and Emilia for constant source of support and stability that was needed to be able to concentrate also on other things, such as this thesis.

Jani Kaartinen

List of Publications

[P1] Kaartinen J., Koivo H., "Machine vision based measurement and control of zinc flotation circuit", Studies in Informatics and Control, 2002, Vol. 11, No. 1, pp. 97-105.

[P2] Kaartinen J., Hyötyniemi H., "Determination of ore size distribution with image analysis", IASTED International Conference on Intelligent Systems and Control, Salzburg, Austria, June 25-27, 2003, pp. 406-411.

[P3] Kaartinen J., Hyötyniemi H., "Combining multi-camera-data of flotation circuit with PCA and PLS", Centenary of Flotation Symposium, Brisbane, Australia, 6-9 June, 2005, pp. 121-125.

[P4] Kaartinen J., Hätönen J., Larinkari M., Hyötyniemi H., Miettunen J., "Image analysis based control of copper flotation", 16th IFAC World Congress, Prague, Czech Republic, July 4-8, 2005.

[P5] Kaartinen J., Hätönen J., Hyötyniemi H., Miettunen J., "Machine-vision-based control of zinc flotation – A case study", Control Engineering Practice, 2006, Vol. 14, No. 12, pp. 1455-1466.

[P6] Kaartinen J., Haavisto O., Hyötyniemi H., "On-line colour measurement of flotation froth", The Ninth IASTED International Conference on Intelligent Systems and Control, Honolulu, Hawaii, USA, August 14-16, 2006, pp. 164-169.

[P7] Kaartinen, J., Tolonen A., "Utilizing 3D height measurement in particle size analysis", The 17th IFAC World Congress, Seoul, Korea, July 6-11, 2008.

[P8] Haavisto O., Kaartinen J., Hyötyniemi H., "Optical spectrum based measurement of flotation slurry contents", International Journal of Mineral Processing, 2008, Vol. 88, No. 3-4, pp. 80-88.

Contributions of the Author – Publications

[P1], [P5] The author wrote the article and provided the results regarding the operator tools and participated strongly in the development of the analyzer. In addition, the author was responsible for the development of the multi-camera analysis system.

[P2] The author carried out all the work related to the publication. H. Hyötyniemi contributed on the idea level and assisted with modelling.

[P3] The author wrote the article, carried out the data analysis and provided all the results, H. Hyötyniemi contributed at the idea stage and helped with the interpretation of the modelling results.

[P4] The author wrote roughly half of the article in co-operation with J. Hätönen and participated in the generation of the results. J. Miettunen made the modifications to the control logic.

[P6] O. Haavisto wrote the chapter regarding the modelling and validation and provided most of its results. The author carried out the rest of the work. H. Hyötyniemi supervised the research.

[P7] A. Tolonen wrote the chapter regarding the data analysis and provided most of its results. The author carried out the rest of the work.

[P8] The author was responsible for the laboratory measurements, developed the on-line prototype and the results related to it. O. Haavisto generated the data analysis and modelling results.

Nomenclature

In general, scalars are presented in non-bolded (typically lowercase) symbols. All vectors are column vectors unless otherwise stated and are presented in bolded lowercase symbols. All matrices are in bolded uppercase symbols.

Operators

$\mathbf{X}^T$	Transpose of $\mathbf{X}$
$\|\mathbf{x}\|$	Euclidean norm of $\mathbf{x}$
$\mathbf{X}^+$	Pseudoinverse of $\mathbf{X}$
$f * g$	Convolution of f and g
Δ	The Laplace operator
$\frac{\partial^n f(\cdot)}{\partial x^n}$	nth order partial derivative of f with respect to x
$G(\cdot)$	Gaussian filter

Symbols

$\gamma_{s/a}$	Solid-air surface energy [J/m^2]
$\gamma_{s/w}$	Solid-water surface energy [J/m^2]
$\gamma_{w/a}$	Water-air surface energy [J/m^2]
θ	Contact angle
$W_{s/a}$	Work of adhesion [J/m^2]
I	Two dimensional greyscale image
I_{binary}	Two dimensional binary image
K	Thresholding value
N_R	Number of rows in a two dimensional image
N_C	Number of columns in a two dimensional image

I_C	Threshold calibration image
$\mathbf{v}_S$	Shadow length histogram
x_R	Horizontal place of a rock in an image [pixels]
l	Shadow length [pixels]
l_C	Compensated shadow length [pixels]
L_1	Lamp distance from the edge of imaging area [m]
L_2	Length of imaging area [m]
$\mathbf{x}$	A data vector of predictor variables
$\mathbf{X}$	A data matrix of predictor variables
y	Predicted variable
$\mathbf{y}$	A data vector of predicted variables
$\hat{\mathbf{y}}$	Estimate of $\mathbf{y}$
$\mathbf{Y}$	A data matrix of predicted variables
$\hat{\mathbf{Y}}$	Estimate of $\mathbf{Y}$
Z^1	Subspace orientation
k	Subspace dimension
$\mathbf{t}$	X-block score vector
$\mathbf{T}$	X-block score matrix
$\mathbf{p}$	X-block loading vector
$\mathbf{P}$	X-block loading matrix
$\mathbf{u}$	Y-block score vector
$\mathbf{U}$	Y-block score matrix
$\mathbf{q}$	Y-block loading vector
$\mathbf{Q}$	Y-block loading matrix
$\mathbf{E}$	X-block residual matrix
$\mathbf{F}$	Y-block residual matrix
λ	Eigenvalue *or* wavelength
$\mathbf{w}$	Weight vector
$\mathbf{W}$	Weight matrix
b	Regression coefficient for inner relation
g	Two dimensional image presenting 3D data
f	Gradient image
h	Directional kernel

e	Euler's number
σ	Standard deviation
$\mathbf{b}_R$	Regression vector
$\mathbf{B}_R$	Regression matrix
R	Correlation coefficient
R^2	Coefficient of determination
i, j, m, n	Indices

Abbreviations

AC	Alternating Current
AG	Autogenous Grinding
A/D	Analog/Digital
CAD	Computer-Aided Design
CCD	Charge-Coupled Device
CCIR	Comité Consultatif International des Radiocommunications (commonly used name for a grayscale image standard)
COM	Component Object Model
CPU	Central Processing Unit
CUMPRESS	CUMulative Predictive Residual Error Sum of Squares
DC	Direct Current
DFT	Discrete Fourier Transform
DLL	Dynamic Link Library
DTR	Data Terminal Ready (signal in serial port communications)
ESPRIT	European Strategic Programme on Research in Information Technology
EU	European Union
EXE	Executable File
HD	Horizontal Drive
HSV	Hue Saturation Value (one type of colour image presentation)
IP	Internet Protocol
LHD	Load Haul Dump (machine type used in mining operations)
LoG	Laplacian of Gaussian
LTR	Long Term Research
LV	Latent Variable
MB	Mega Bytes (1024^2 bytes)
MLR	Multiple Linear Regression

MMMI	Mining, Mineral and Metal Industry
NaIBX	Sodium Isobutyl Xanthate
NIC	Network Interface Card
NIPALS	Algorithm for calculating PLS
OLE	Object Linking and Embedding
OPC	OLE for Process Control
PAL	Phase Alternate Line (colour image standard)
PC	Principal Component *or* Personal Computer
PCA	Principal Component Analysis
PCR	Principal Component Regression
PGP	Prism-Grating-Prism
PLS	Partial Least Squares *or* Projection to Latent Structures
RAM	Random Access Memory (volatile memory with direct access)
RGB	Red Green Blue (image)
RMS	Root Mean Square
ROI	Region Of Interest
rPLS	recursive Partial Least Squares
SAG	Semi Autogenous Grinding
SC	Solids Content
SIMPLS	Algorithm for calculating PLS
SSH	Secure Shell
TCP	Transmission Control Protocol
TEKES	Finnish Funding Agency for Technology and Innovation
UI	User Interface
UPS	Uninterruptible Power Supply
USB	Universal Serial Bus
VD	Vertical Drive
WLAN	Wireless Local Area Network
VNIR	Visible and Near InfraRed
XML	eXtensible Markup Language
XRF	X-Ray Fluorescence

Chemical Symbols and Compounds

Au	Gold
Cu	Copper
Fe	Iron
Pb	Lead
S	Sulphur
Zn	Zinc

$BaSO_4$	Barite mineral
CaOH	Calcium Hydroxide
$CuFeS_2$	Chalcopyrite mineral
$CuSO_4$	Copper sulphate
$Fe_{(0.8\text{-}1)}S$	Pyrrhotite mineral
FeS_2	Pyrite mineral
Fe_2O_3	Hematite mineral
Fe_3O_4	Magnetite mineral
PbS	Galena mineral
(Zn,Fe)S	Sphalerite mineral

Contents

1. Introduction

1.1. Background and Motivation

Since the beginning of civilization people have used metals and other minerals from the earth's crust to make life easier by the use of manufactured tools, for example. The oldest known mine, called *"Lion Cave"* in Swaziland, was used about 43 000 years ago by paleolithic humans to extract the hematite mineral (Fe_2O_3) for red ochre pigment production [109]. In the world today, the mining, mineral and metal industry (MMMI) is an important part of the global industry sector. Even though people may not have to encounter the MMMI in their daily lives, they certainly enjoy the results of it all the time. For example, mined metals are present everywhere; in the ribbed bars that are used to strengthen the concrete structures of our houses, in our cars, silverware, computers, TVs, cell phones, etc. The list is endless, and this list was only concerning metals.

The drawback of the MMMI is that it often exploits exhaustible sources and the production phase may leave a big ecological footprint. Thus, many of the world's nations have regulations for mining operations [109]. However, as the technology evolves, it enables more efficient operation of the MMMI. Although the drivers for this are often economical, the improved efficiency usually means reduced negative impacts on the natural environment. A good example is the *flotation* technique which is an essential part of this thesis; over the years the technology has evolved so much that currently there are flotation plants running economically viable operations by treating the waste that was produced with the older technology [110]. In other words, the *recovery* (see Subsection 3.3.2 for a detailed description) was so low that significant amounts of valuable minerals were lost because the technology used was not able to separate the valuables from the invaluable gangue.

This thesis aims to add to this evolution of the technology, and it is the author's firm opinion that it has done so by utilizing the evolvement of another field, namely computer and vision technology. The thesis shows an application oriented approach for utilization of machine vision technologies in the context of the MMMI. Naturally, an application environment is needed for this type of approach,

and in the case of this thesis it has been a zinc, copper and sulphur mine located in Pyhäsalmi (Finland), owned by the Canadian Inmet Mining Corporation.

Machine vision technologies covered in this thesis are:

- Imaging done on the visible wavelength range (λ=380-760nm) with traditional greyscale and colour cameras.
- Spectral measurements on the *visible and near-infrared* (VNIR) range (λ=400-1000nm) [9].
- 3D imaging.

These technologies are applied to contact-free particle size analysis of material that is moving on a conveyor belt and to machine vision based measurement and control of flotation.

The work presented in this thesis proves that machine vision techniques are a valuable asset in the measurement and control of a mineral enrichment process; the presented results show improved performance in terms of control and economics. Furthermore, a new technique is presented for improving the measurement capabilities of current *X-Ray fluorescence* (XRF) analyzers that often are the backbone in the control of a modern flotation process. The work carried out in this thesis has enabled new ways of combining traditional XRF measurements with optical spectroscopy methods, as presented in Chapter 6.

1.2. Objectives

The main objective of the study is to examine the usefulness of machine vision techniques in the context of the mining, mineral and metal industry (MMMI). This can be divided into following sub-objectives:

- To evaluate the possible application domains for machine vision within the MMMI, and their importance.
- To study machine vision in the context of the mineral enrichment process by using Pyhäsalmi mine as a case example. And specifically; to gain information on the potential of machine vision in the control of the flotation process.
- To evaluate the dependencies between froth characteristics and process variables.
- To obtain information about the dependencies between froth or slurry colour characteristics and mineral grades.
- To utilize the above mentioned information in order to gain increased control performance.

1.3. Summary of Publications

This thesis covers over ten years of machine vision related research which was initiated in 1997 by a collaborative venture between the Helsinki University of Technology and the University of Oulu in Finland, the University of Rome "La Sapienza" in Italy, the Royal Institute of Technology in Sweden and two mining companies; Outokumpu Mining Oy – Pyhäsalmi Mine in Finland (currently owned by the Inmet Mining Corporation, as mentioned before) and Boliden Minerals AB in Sweden. The project was called *"Characterisation of Flotation Froth Structure and Colour by Machine Vision (ChaCo)"*. It was funded by the European Union and ended in 2000. The author joined this project in the spring of 1999 and started working with the on-line analyzer that was built for the zinc rouger circuit of Pyhäsalmi mine. The objectives of the project and some of the results, especially the ones conserning the Pyhäsalmi case, are reported in [P1].

After the ChaCo project, the research continued with three consecutive national projects, that were supported by the Finnish Funding Agency for Technology and Innovation (TEKES). These were: *"Intelligent, Machine Vision Based Control for a Flotation Process (VÄSY)"* in 2001-2004, *"Intelligent Methods in Mining Environment (ÄKSY)"* in 2005-2006 and *"Performance Improvement for Concentration Process (RIKE)"* in 2007-2008. During these projects, the single cell analyzer was extended to multi-camera version and the new image variables were utilized in the zinc circuit, as reported in [P3] and [P5]. Later, the copper circuit was included in the analysis and the image variables obtained from the flotation cell producing the final copper product were utilized in closed loop control [P4].

Research done with traditional *RGB cameras* suggested that the colour of the froth gives a good indication of grade changes in a flotation cell. This phenomenon was further studied with a more accurate instrument to obtain spectral measurements of the froth. The measurements were recorded simultaneusly with an RGB camera and a *spectrophotometer*, the results showing that both devices were able to predict grade based on colour information, although the spectral measurements were more accurate [P6].

This research was continued with laboratory analysis of spectral measurements that were made from *slurries*. As this pilot analysis showed good results, a prototype capable of continous on-line analysis was constructed and installed to measure the concentrate grades of the final zinc product in Pyhäsalmi, and again excellent prediction results were obtained, as reported in [P8].

In addition, another field of research presented in this thesis is the particle size distribution analysis of crushed ore, which was started based on the initiative of Pyhäsalmi Mine Oy, since there was a real need for information about the particle size distribution formed at the primary crusher in the mine. This information can be used in the flotation plant to achieve better grinding results. Thus, a new type of measurement was realized with a shadow based image analysis method that was

used to calculate the particle size distribution in a contact-free manner from a moving conveyor belt [P2], and was later replaced with a more sophisticated measurement technique based on 3D measurements of the moving ore bed [P7].

1.4. Contributions of the Author – Thesis

The contributions of the author presented in this thesis can be summarized as follows:

- A novel multi-camera image analysis platform was developed and the new image based variables obtained with it were studied and used in closed loop control.
- New results regarding the measurement capabilities of image variables in a multi-camera setting were obtained.
- A new type of froth level measurement that can be used to accurately measure the location of the froth layer and thus to gain an accurate froth thickness measurement was developed.
- A tool for flotation plant operators, which can be used to check the current and previous appearance of different flotation cells, was developed. This information, together with conventional process measurements, helps to get a more detailed picture of the state of the process and can be used both in process control and for educational purposes (i.e., for learning from the history information).
- Results regarding the usefulness of froth colour in predicting grades were obtained and a comparison between a traditional RGB colour camera and a more accurate spectrophotometer was carried out.
- A new type of on-line measurement technique used to supplement existing X-Ray fluorescence (XRF) analyzers for reducing their typical sampling interval of 10-20 minutes to a virtually continuous measurement was created. The author was responsible for the initial laboratory tests, where the usefulness of the new technique was verified. Also, he implemented the on-line prototype that was used in the first practical tests.
- Two new measurement techniques for realizing contact-free particle size distribution analysis were developed. These are applicable to analysis of a material that is moving on a conveyor belt.

1.5. Structure and Organisation of the Thesis

This thesis is organized as follows. Chapter 2 discusses the current status of the image analysis work related to the mining, mineral and metal industry (MMMI), and to work carried out in this thesis. Then, in order to give the reader a better understanding of the application environment, the mineral enrichment process of the Pyhäsalmi mine is described in Chapter 3.

The work related to the publications of this thesis is presented in Chapters 4-6. Chapter 4 discusses the particle size distribution analysis that was developed to provide information on the size distribution generated by the primary crusher in the mine. Chapter 5 introduces a machine vision based analysis platform for flotation froths, its evolution to a multi-camera analyzer, and the obtained results in terms of new scientific information and practical applications, such as closed loop control. The results presented in Chapter 5 led to a thorough analysis of the dependency between colour and grade. This work eventually resulted in a new measurement technique for improved grade analysis, which is discussed in Chapter 6.

Finally, the conclusions are presented in Chapter 7.

2. State of the Art in Machine Vision within MMMI

The mining, mineral and metal industry (MMMI) has been making use of advances in camera and information technology, which have resulted in better cameras and computers. An overview of some common systems related to the scope of this thesis is presented in the following.

In recent years, the development in camera and information technology has produced better cameras and better computers with significantly increased capabilities in storage and computational power (i.e. CPU power). These advances have led to the integration of machine vision based applications into many branches of industry, such as the MMMI. The MMMI often sets quite strict requirements on new technology; including, for example, harsh environmental conditions, dust that can be electrically conductive, moisture and direct water contact, vibrations, shocks in air-pressure (due to blasting), power outages, etc. Because of these challenges there has been extensive research on the subject. A few commercial products available on the market will be presented in this chapter.

The following subsections outline some of the aforementioned developments in two parts: *Particle Size Measurement Systems* and *Flotation Analysis Systems*. The first part presents particle size analyzers and related research. The common feature in the research and devices considered in this part is that they possess non-contact measuring capabilities and can therefore be used in a similar setting as the analyzer to be described in Chapter 4. The second part refers to the research to improve flotation performance using image analysis techniques.

2.1. Particle Size Measurement Systems

There are several commercial imaging systems that are able to measure particle size distribution from a moving conveyor belt. These include: the Split Imaging

System (see [20] and [21]), WipFrag Imaging System (see [68]), FragScan Imaging System (see [94] and [95]), VisioRock Imaging System (see [25]), PowerSieve Imaging System (see [62]) and PlantVision Imaging System (see [54]). A screen capture from the Split-Online® imaging system is shown as an example in Fig. 2.1 below. Common to all of these systems is that they are based on photographic images taken of the target. This image is then processed and typically converted into binary image, from which the particle segments are extracted and size distribution calculated. There are also scientific studies around the subject, where a greyscale image has been used as a starting point for particle size analysis (see e.g. [10], [12], [93], [105] and [106]). Some approaches make also volume estimations based on greyscale images (see e.g. [67] and [91]). These types of systems have been shown to work fairly well when the lighting conditions are good. Conversely, they are sensitive to changes in lighting conditions and especially to disturbing shadows [105]. Furthermore, the slow drift in intensity (due to dusting, for example) can cause problems in the long run, when considering on-line applications. The shadow based analysis technique presented in Section 4.2 was designed to overcome these issues.

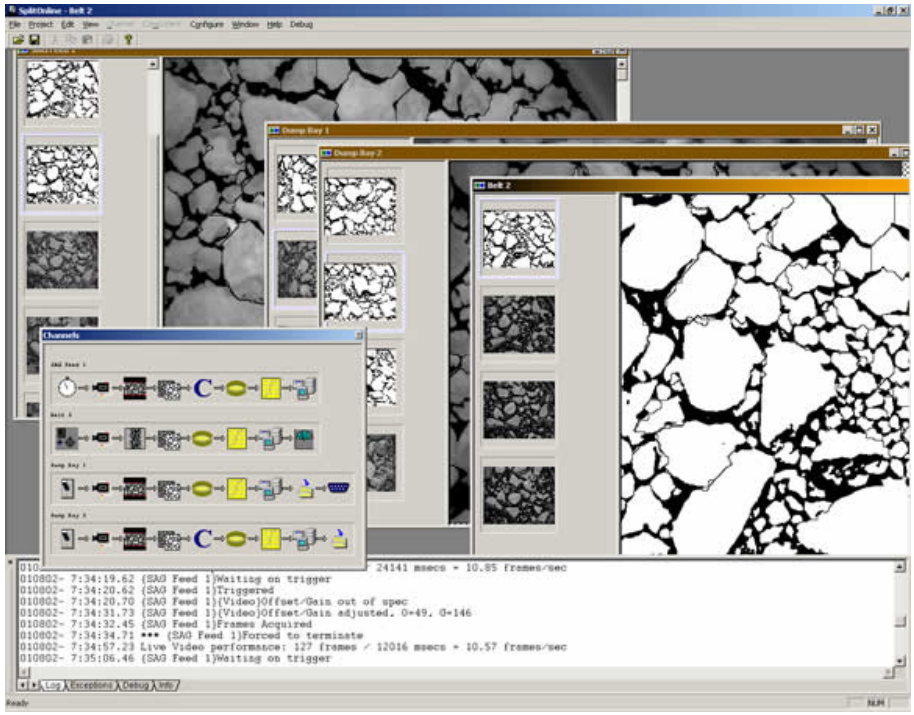

Fig. 2.1 An example of the image based segmentation system; Split-Online® by Split Engineering. (www.spliteng.com)

Another possibility is to use a 3D image as the starting point for the segmentation analysis. Lee *et al.* [63], [64] show a laser triangulation method and discuss the advantages of the 3D approach. Kim *et al.* [52] demonstrate an aggregate testing

system built around a laser profiler mounted on a horizontal gantry system. Thurley demonstrates 3D imaging in his thesis [105] by using so called "Monash Shape Measurement System" which is applicable to laboratory tests only. More recently, Thurley and Andersson [106] have presented an on-line implementation for iron ore green pellets based on structured light and camera triangulation. These approaches are very close to the method described in Section 4.3 and reported for the first time in [51]. The main difference is that the method presented in this thesis is based on a direct 3D measurement and a belt weigher is located on the same cross directional axis as the laser scanner. This enables the use of the weight information, not only in scaling back the calculated proportions to real life mass flow values, but also in the calibration model.

2.2. Flotation Analysis Systems

Woodburn *et al.* [117] introduced machine vision aided flotation control to the MMMI in late 1980s [103]. Since that time, several studies have proven the fact that the visual appearance of flotation froth can be used as an indicator of metallurgical performance (see e.g. [1], [8], [11], [75], [76], [77], [80] and [81] in addition to the publications presented in this thesis). One important contribution to the research in this area was the EU funded *ChaCo* project, mentioned in Section 1.3. It was an international ESPRIT LTR (Long Term Research) project, which was active from 1997 to 2000. A considerable number of scientific results were published based on the work carried out during this project (see e.g. [4], [5], [32], [38], [39], [41], [42], [57] , [58] and [107]). As mentioned, the author had the privilege to contribute to that research and most of the ground work regarding Chapter 5 was completed at that time.

Since then, several machine vision applications regarding mineral flotation have been reported (see e.g. [2], [8], [35], [48], [65] and [79]). However, only a few systems are commercially available:

- *FrothMaster™ by Outotec Minerals Oy* (Fig. 2.2)

  The FrothMaster is based on image analysis of colour images obtained with an RGB PAL camera. An optional protective hood is available for protection against ambient lighting and other environmental factors. Calculations are semi-distributed; every group of four cameras processes their own images. The calculated variables are: froth speed and direction, bubble size distribution, froth stability and colour histogram. In addition, statistical information is calculated for these variables (when applicable). Each group includes a video server that is able to send a video feed to a web browser through a TCP/IP network. [83]

  FrothMaster installations can be found in several plants. This includes also Pyhäsalmi since the prototype version of the FrothMaster 2™ was originally tested there. Also, some of the calculated variables were compared against the image analyzer presented later in this thesis. The

most famous case example of the performance improvements obtained with the aid of FrothMaster is the Cadia Hills Gold Mine in New South Wales (Australia), reported by van Olst *et al.* [108] and by Brown *et al.* [7].

Fig. 2.2 FrothMaster™ 2 flotation froth analyzer. [83]

- *VisioFroth™ by Metso Minerals Oy* (Fig. 2.3)

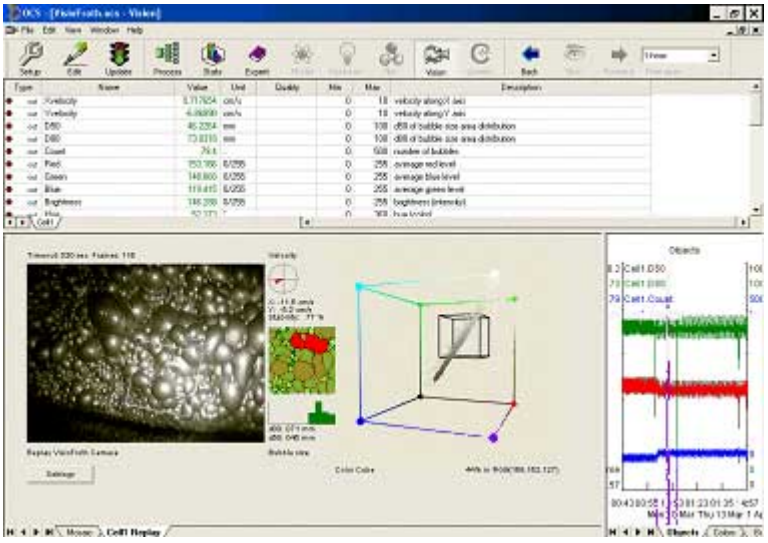

Fig. 2.3 VisioFroth™ analyzer. (www.metsominerals.com)

The VisioFroth imaging system is typically based on multiple USB cameras and centralized computing. At the website of the Metso Minerals corporation (www.metsominerals.com) it is stated that: *"VisioFroth measures real time froth velocity, bubble size distribution, color and other froth properties"*. In addition, at least froth stability is measured [90]. The VisioFroth system has been installed at various locations around the world. The largest installation (at least known to the author) is at PT Freeport Indonesia, where 172 froth cameras are used [103].

- *PlantVision™ by KnowledgeScape Inc.* (Fig. 2.4)

  To the author's best knowledge, there is no published literature available where the details or usage of PlantVision for flotation has been reported. According to KnowledgeScape's own brochure [55], PlantVision supports multiple camera types (analog, IP, Firewire and USB) and centralized computing. The calculated variables are: bubble size, colour components (R, G, B and gray), froth velocity, froth texture and froth stability. Software cycles through cameras, processes the video streams and makes the data available via OPC (OLE for Process Control).

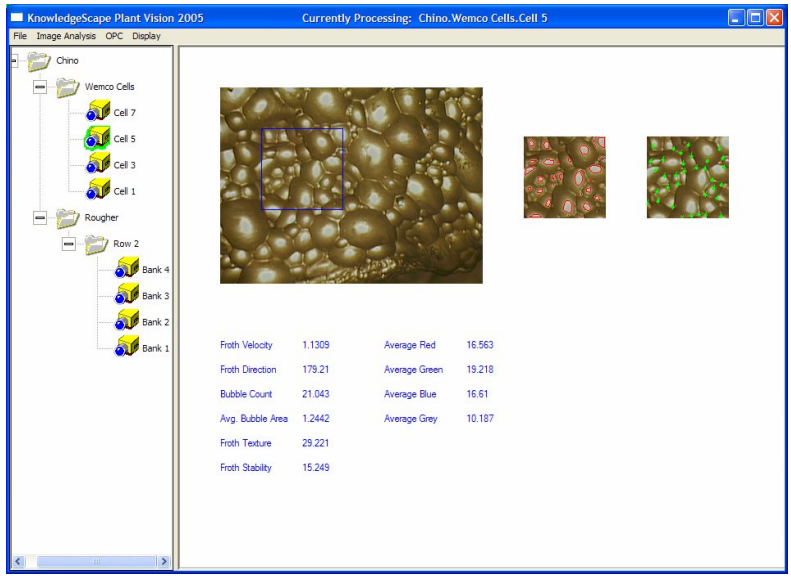

Fig. 2.4 KnowledgeScape PlantVision 2005. [55]

- *METCAM FC by SGS Minerals Services Inc.* (Fig. 2.5)

  The flotation camera technology of the SGS Group was obtained through a corporate acquisition of MinnovEx Technologies Inc. in 2005. According to the SGS website (www.met.sgs.com), the camera is able to measure directional froth velocity, froth stability, bubble size distribution and 6 image colour variables. It also includes a wireless network option for data transfer. As with PlantVision, the author found no references describing applications and possible results obtained with this system.

Fig. 2.5 METCAM FC. (www.met.sgs.com)

- In addition to the ones mentioned above:
  - WipWare Inc. is bringing a new product to the market called WipFroth™ [112]. The company is best known for their work on optical granulometry of fragmented material and especially from their WipFrag product [68] which is related to particle size measurements considered in Section 2.1.
  - The IMSOC Froth Image Analyzer (FIA) software, used also in Pyhäsalmi during this research, is described in Subsection 5.3.1

When considering the optical spectrum based methods that are used for grade prediction, that is to say systems similar to the one described in Chapter 6 of this thesis, only three publications (see [16], [17] and [88]) appear, and they are all based on a technology developed by a South African company called *Blue Cube Systems* (Pty) Ltd. Their product is called the *Instant Mineral Quantifier* (IMQ) and it is based on spectral measurements in the visible and near-infrared (VNIR) range (λ=400-1000 nm). The IMQ has been reported to work relatively accurately with dry mineral samples by Reyneke *et al.* [88] and the system can be used also for slurry measurements, as reported by de Waal [17]. However, similar validation reports as presented for dry samples are not available to assess performance in the case of slurries. Furthermore, the IMQ requires calibration samples that are used

for informing the system about the mineralogical properties of the material being analyzed. Based on these samples, a fixed model will be implemented and used for prediction. As new samples arrive, they can be used to re-calibrate the model.

The technique presented in Chapter 6 is also operating on the VNIR range but differs from the IMQ, because it is a supplement to existing X-Ray fluorescence (XRF) analyzers and thus the modelling can be (and is) automated by utilizing the XRF results. What is more important, the model is continuously updated in order to compensate for the changes in ore properties.

Finally, in the middle of 2007, ABB introduced a spectrum based bulk material analyzer called the *SpectraFlow CM 100*, which is based on technique called the *Safe On-Line Bulk Analysis System* (SOLBAS™) [70]. The system is operating on a wavelength range of 350-2500 nm and can predict elemental components of bulk material running on conveyor belts. According to ABB, the device can also be used for flotation froth analysis (when imaged from above). The measurement is carried out by combining spectra from different wavelength ranges (measured with separate devices) and mapping spectral data into elemental compositions with a multi-variable linear regression model, which is calibrated with 20 to 70 known samples, depending on the complexity of the application.

The author found no published literature describing the SOLBAS™ technology or its usage. According to the ABB website (www.abb.com), the technology is utilized in cement manufacturing and has also been adopted for sinter composition analysis in a steel factory in Bremen, Germany. To the author's best knowledge, the SOLBAS™ technology is not available for slurry analysis in a similar setting to that described in Chapter 6.

3.
The Test Bench – Pyhäsalmi Mine

The on-site development for this thesis was carried out in the Pyhäsalmi mine, located in the town of Pyhäjärvi in central Finland. The main products, *copper* (Cu), *zinc* (Zn) and *sulphur* (S), are extracted from 1050-1421 meters below ground level. In the early phases of this study, the mine was still owned by the Finnish Outokumpu Corporation, but it was sold in 2002 to the Canadian based Inmet Mining Corporation. The Pyhäsalmi mine is well suited to the type of research carried out in this thesis, because it is a modern and well instrumented plant, and is claimed to be one of the best performing mines worldwide [46]. Also, the flotation circuit is used as a text book example for flotation of copper-zinc and copper-lead-zinc ores [110]. Consequently, at least for the most part, the results presented in this thesis can be generalized to other plants and processes of similar characteristics. This chapter describes the history and production of the mine, giving a description of the process and indication of the places where the research was carried out. A significant part of this chapter, especially in the first two sections, is adopted from [46].

3.1. History & Geology

The massive zinc-copper-pyrite (sulphur is mainly contained in the *pyrite mineral*, FeS_2) deposit in Pyhäsalmi contained originally 54 million tonnes of ore. The main ore body is located underground and reaches the surface via a narrow vertical extension, as shown in Fig. 3.1 and Fig. 3.2. The ore is massive and coarse grained, which helps in the grinding phase of the process (grinding is covered in Subsection 3.3.2). Also, the contact between the ore and waste rock is sharp, which reduces the amount of *gangue* (i.e. invaluable rock) that needs to be processed. The ore contains 75% *sulphides*, which consist of; *chalcopyrite* – $CuFeS_2$ (3%), *sphalerite* – (Zn, Fe)S (4%), *pyrrhotite* – $Fe_{(0.8\text{-}1)}S$ (2%), *pyrite* – FeS_2 (66%) and a small amount of *galena* – PbS and *sulphosalts*. The main gangue minerals are *barite* – $BaSO_4$ and *carbonates*.

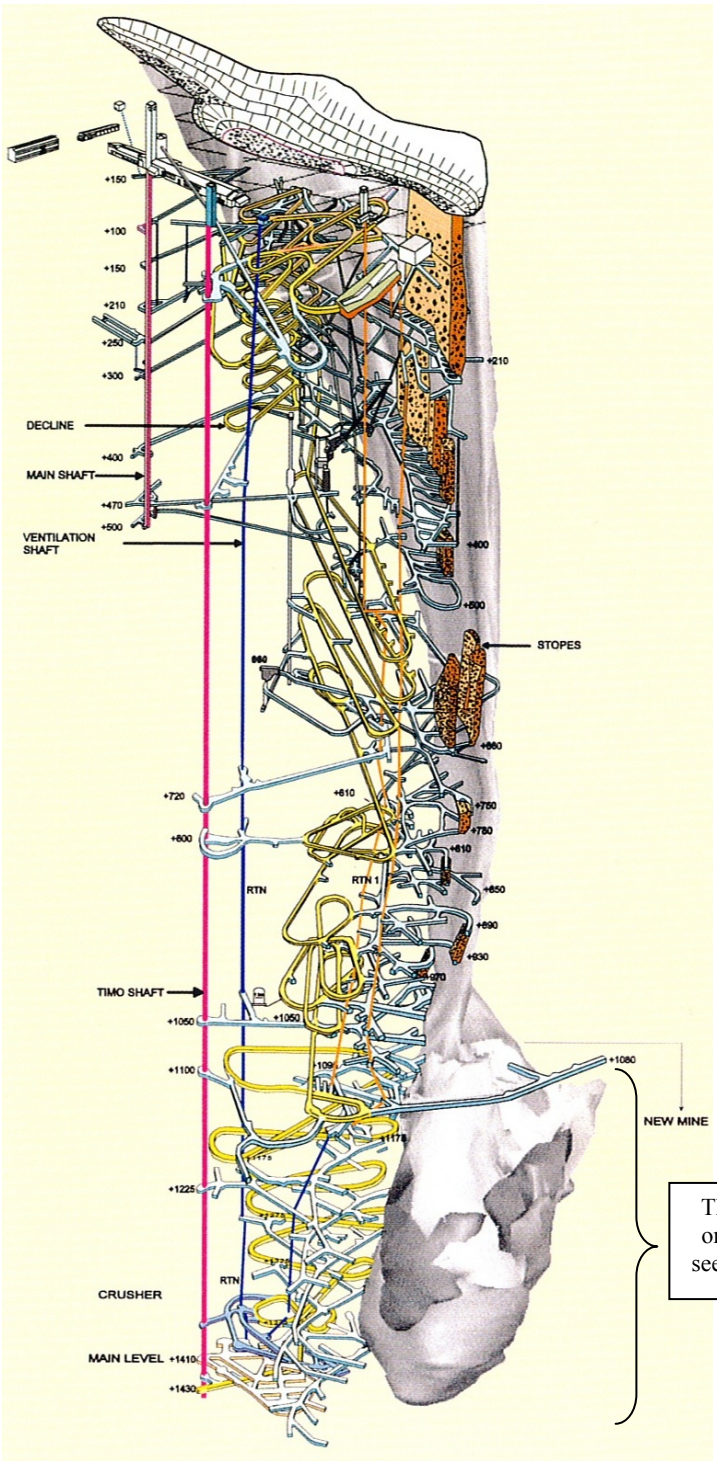

Fig. 3.1 Pyhäsalmi ore deposit and tunnel network. (courtesy of Pyhäsalmi Mine Oy)

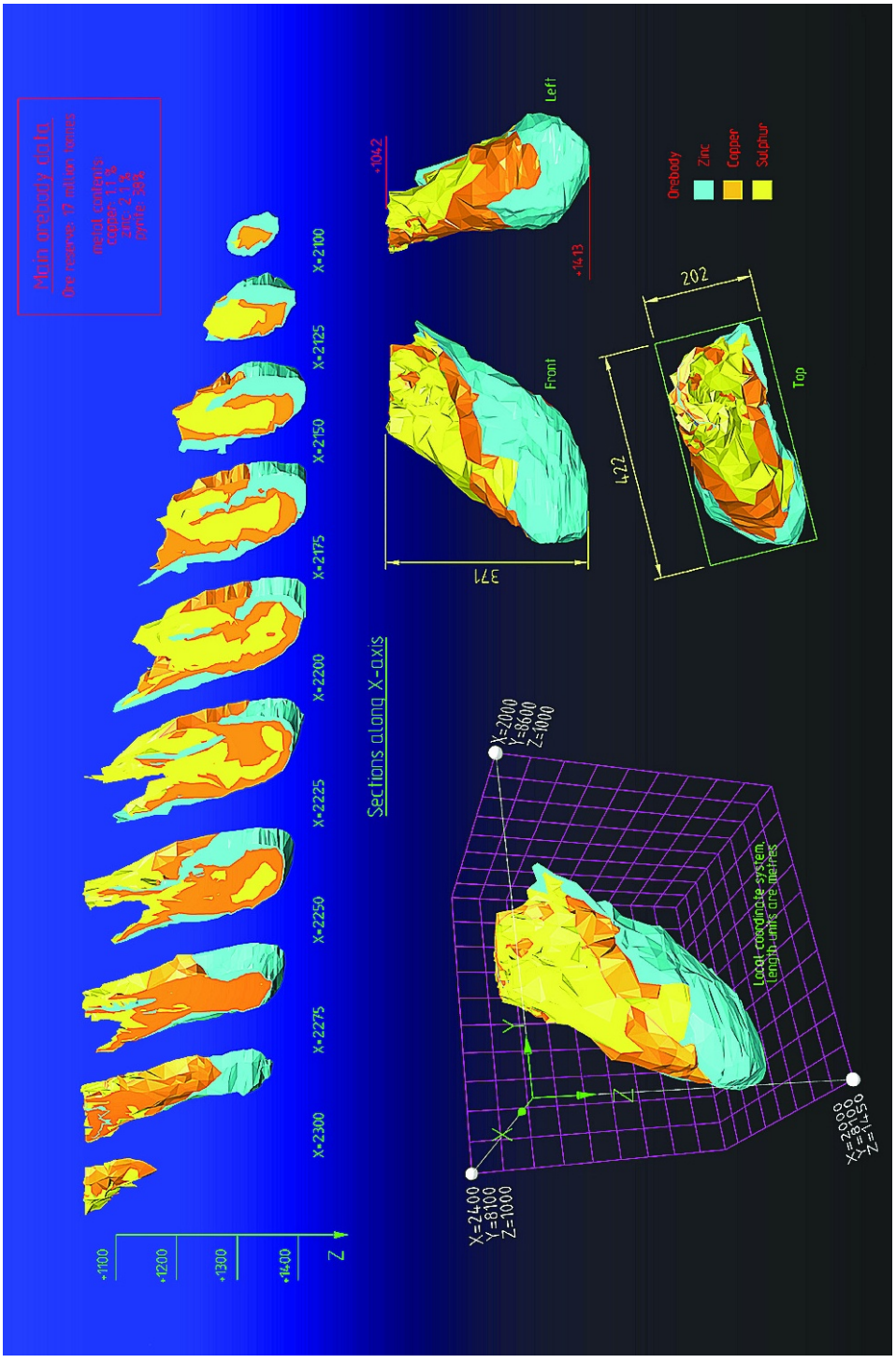

Fig. 3.2 The main ore body. (courtesy of Pyhäsalmi Mine Oy)

The ore deposit was found by accident in 1958, when a local farmer was digging a well for fresh water. Outokumpu Oy conducted thorough geological surveys and decided to open a mine in Pyhäsalmi, which eventually was started on March 1, 1962 as an open pit operation. Five years later, in 1967, underground operations were started and operated jointly with open pit mining until the open pit was completely exhausted in 1975.

To ensure efficient underground operations, a blind shaft called the *"Olli shaft"*, extending to a depth of 730 meters, was opened in 1985. The mine was gradually deepened as it was noticed that the ore body extends as a narrow band. A depth of one kilometre was reached in the spring of 1996.

For a while it looked as if the mine would be completely exhausted by the year 2000, but fortunately a new large lens shaped deep ore body was found in 1996 [45]. In order to utilise this finding a new 1440 meter deep shaft was constructed and named as the *"Timo shaft"* after the chief geologist Timo Mäki. At the same time the mine was thoroughly modernised and, after three years of construction, a completely new mine was opened in 2001. As an anecdote, it could be mentioned that the world's deepest sauna[1] is located in the new mine at 1410 meters below the ground level.

3.2. Production

The mine's production between 1962 and 2007 is shown in Fig. 3.3. As it can be seen the production rate has steadily increased to roughly 1.4 million tons per year. The amount of final products achieved on a yearly basis is shown in Table 3.1.

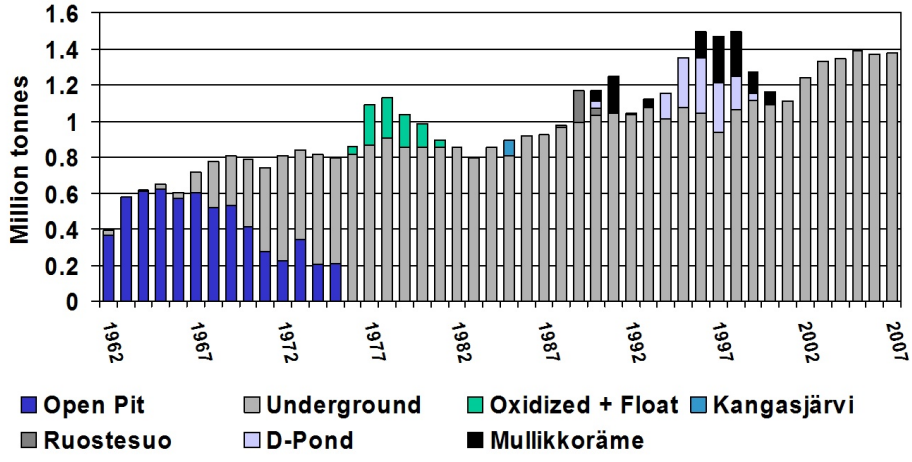

Fig. 3.3 Ore production 1962-2007. (courtesy of Pyhäsalmi Mine Oy)

[1] The author is still waiting an invitation to go and test it.

All concentrates are transported via railroad at an approximate rate of 2500 tons per day. Copper and zinc are sold to domestic smelters. Pyrite concentrate is sold partly to Finnish refiners and partly abroad.

Table 3.1 Annual amounts of different final products.

Product	**Annual amount**	**Grade**
Copper concentrate	50 000 t	29.0% Cu
Zinc concentrate	70 000 t	54.0% Zn
Pyrite concentrate	600 000 t	51.0% S
Gold	260 kg	
Silver	12 000 kg	

3.3. Process Description

This section gives a general process description, in which the process stages where measurements and control actions related to this work are described in detail. Measurement points are indicated for later reference in the text.

As stated earlier, in its current state Pyhäsalmi mine is getting its ore from 1050-1421 meters below ground level. This means that the ore must be pre-treated for transportation already in the mine and there must be an effective ore transportation chain from the mine to the surface. The main parts of the transportation chain can be seen in Fig. 3.4; first, the ore is transported with *load-haul-dump* (LHD) machines (see Fig. 3.5) to ore passes or tipped directly to the jaw crusher for pre-treatment. Jaw crusher ensures that the largest particles are small enough – typically less than 50 cm in diameter – to flow smoothly along the rest of the ore transportation chain.

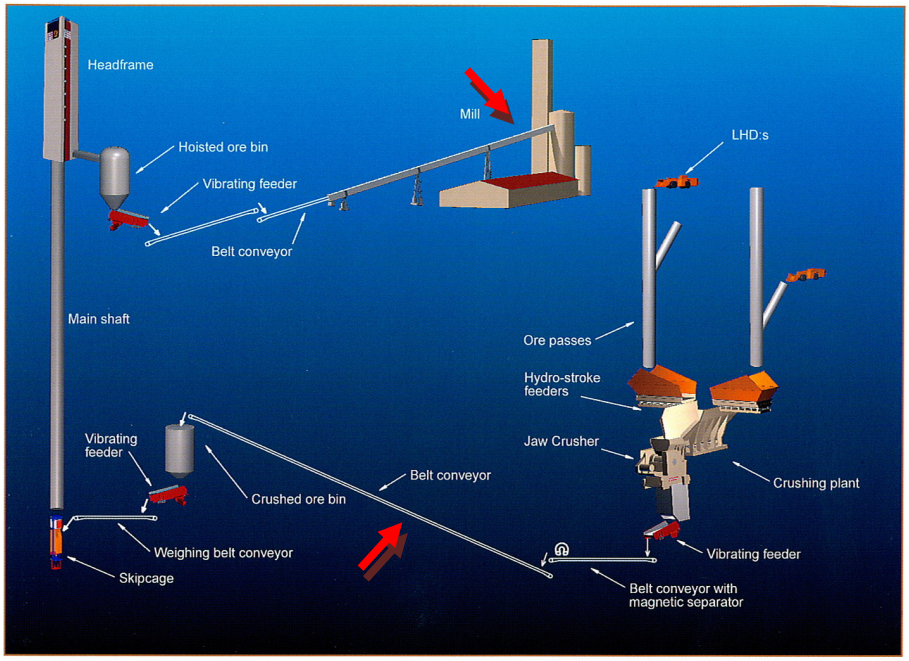

Fig. 3.4 Overall description of the mining process. Measurement points for the particle size measurements are indicated with arrows. (courtesy of Pyhäsalmi Mine Oy)

After the crusher, there is a magnetic separator that removes almost all metallic objects that could cause problems for transportation and should not be mixed with the ore in the first place. An example of such objects is the metal rods that are used when reinforcing the tunnel walls and ceilings. However, this separation is not perfect as discussed later in Chapter 4. After separation, there is a long conveyor belt leading to the underground crushed ore bin which has a capacity of 2000 tons. From this silo the ore is hoisted to an 8000 ton ore bin that is located just below ground level and transported to the mill's screening station (and to further processing, described later in this section).

The measurement points for the particle size distribution analysis (see Chapter 4) are indicated with arrows in Fig. 3.4. As it can be seen, the first analysis point is located almost right after the crushing and the second just before the mill's mechanical screening station. Typical time delay between these points is 1-3 days.

Fig. 3.5 A LHD loader with 21t capacity. (courtesy of Pyhäsalmi Mine Oy)

3.3.1. Underground Operations

The mining methods used in Pyhäsalmi are sublevel stoping and benching. A general illustration of the stoping method is displayed in Fig. 3.6. It is a mining method in which the ore is blasted from different levels of elevation but removed from one level at the bottom of the mine. In Pyhäsalmi, the stopes are 15-25 meters wide, 25-50 meters high and 30-40 in length. This leads to an ore capacity of 50 000-150 000 tonnes per stope. A typical fan distance for the blasting is 3-4 meters. [46]

During (and partly due) to the particle size distribution research (see Chapter 4) a larger fan distance was successfully tested and taken into use in Pyhäsalmi [60]. This gives not only cost savings in drilling and explosives, but also a way to control the larger end of the particle size distribution coming from the jaw crusher. Therefore, the results of the particle size distribution analysis can also be used in mining.

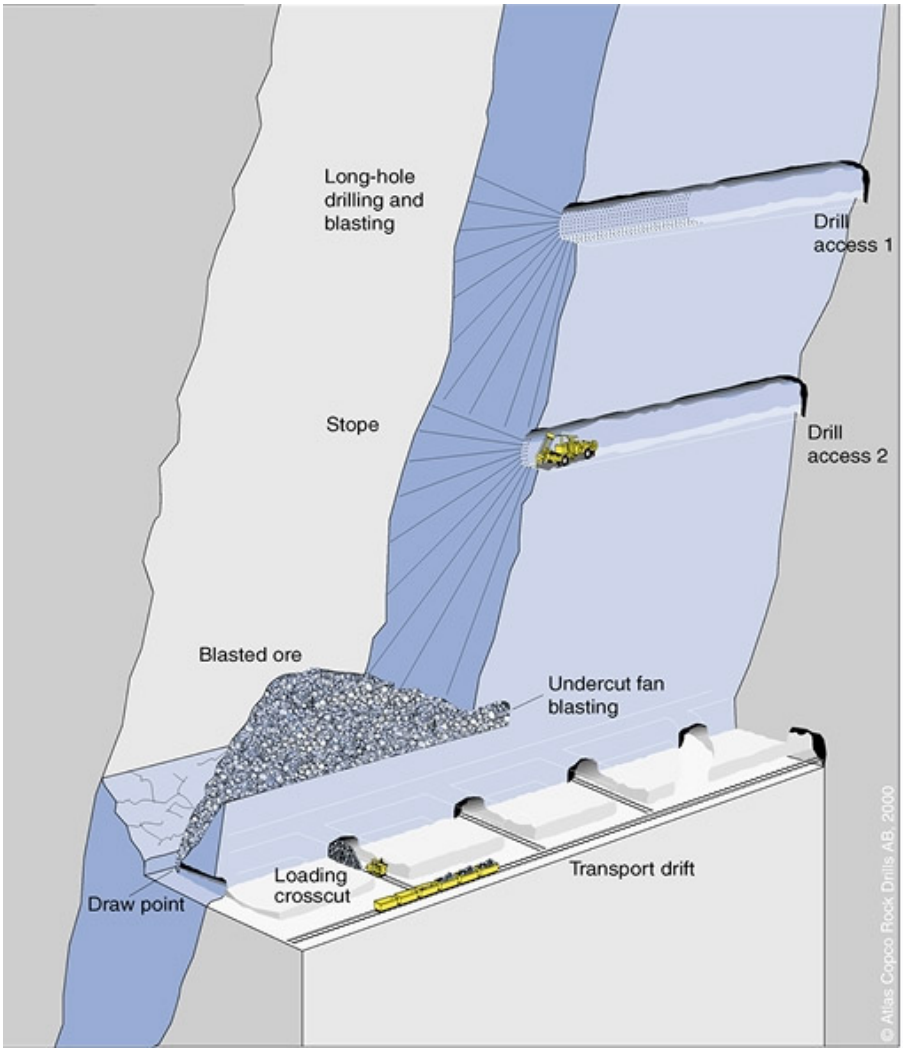

Fig. 3.6 Sublevel stoping method. (courtesy of Atlas Copco)

3.3.2. Concentration Plant

The basic objective of mineral processing is always the same; to separate the minerals into at least two products so that the valuable mineral(s) are present in the *concentrate(s)* and the invaluable particles (i.e. gangue) in the *tailing(s)*. Obviously, this type of process is never perfect; for example, the locked particles where the valuable mineral is attached to or is inside of an invaluable particle should not go to either class. If these types of particles are taken into the concentrate, they will decrease the *concentrate grade* because of the invaluable particles that will be introduced to the *concentrate flow*. On the other hand, valuable minerals will be lost if these particles are taken into the tailings and thus the *recovery* of the valuable minerals from the ore to the concentrate will suffer.

This leads to *grade-recovery dependency*, which is an elementary concept in mineral processing and illustrated in Fig. 3.7 below.

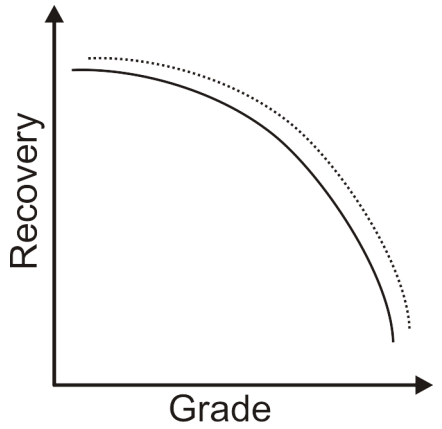

Fig. 3.7 An example of a typical grade-recovery curve shape.
An improved curve is illustrated with dotted line.

Generally, the concentration plant moves along the non-linear grade-recovery curve and it is the operators' duty to run the plant as near as possible to the optimal point in the curve. The selection of this point is dependent on many things such as the quality of the fed ore, quality of the process equipment, desired production rate and so on. Economics have also their own effect; the market prices for specific minerals, shipping costs, desired grade, penalties for lower grades, etc. influence on whether to emphasise grade over recovery or vice versa.

However, if the process can be improved, for example, with a more intelligent copper sulphate ($CuSO_4$) controller (as will be seen later in this thesis) then the grade-recovery curve can be shifted to a higher level so that both measures will improve. This is illustrated in Fig. 3.7 with a dotted line.

In Pyhäsalmi, the grade-recovery curve is realised with three stage grinding circuit, followed by three cascaded flotation circuits (Copper, Zinc and Pyrite) each consisting of several interconnected flotation stages (see Fig. 3.8). After flotation, the final product is dried and transferred by train for further processing. The main process stages are described in the following.

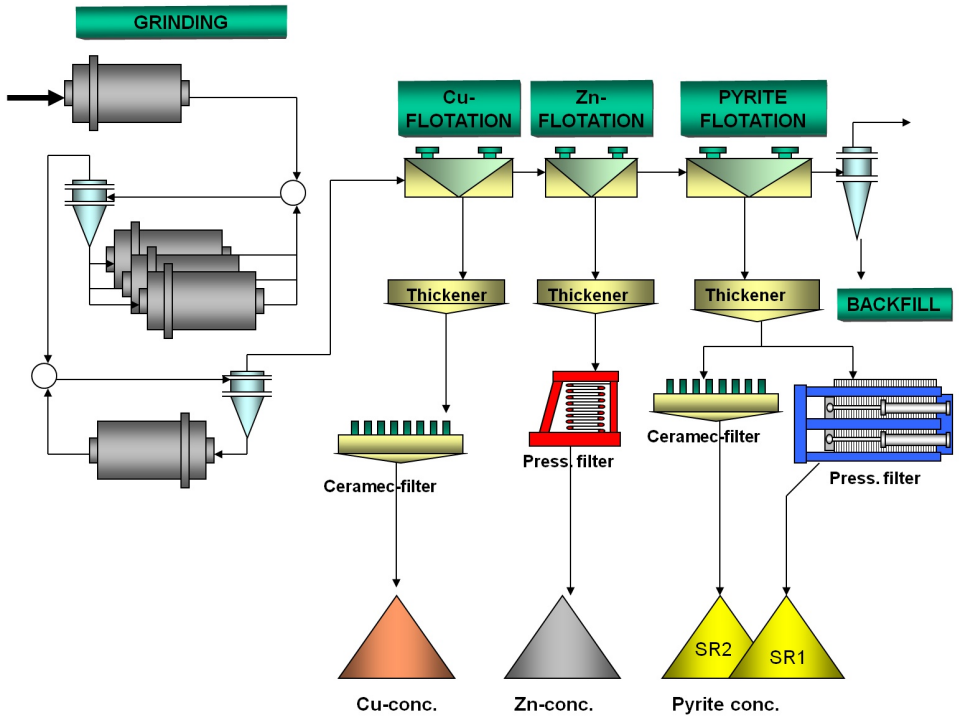

Fig. 3.8 Schematic diagram of the grinding and flotation process. (courtesy of Pyhäsalmi Mine Oy)

Screening

When the raw ore arrives at the mill it is fed to a mechanical screening station (see Fig. 3.9) which separates the ore into five fractions called *fines, pebbles, middle fraction*, *lumps* and *oversized*. These names will be used later in this thesis to describe the fraction sizes shown in Table 3.2.

Table 3.2 Screened size fractions and their names.

Size Class	**Fraction Name**
0 – 30 mm	Fines
30 – 80 mm	Pebbles
80 – 100 mm	Middle fraction
100 – 200 mm	Lumps
>200 mm	Oversized (re-crushed and fed to fines)

The separation must be done for an efficient operation of the grinding circuit. The screened ore is then stored in three ore bins, namely the *fine ore bin*, the *pebble ore*

bin and the *lump ore bin*. The oversized fraction is re-crushed to fines and the middle fraction can be stored either as lumps or pebbles. A typical operation mode is illustrated in Fig. 3.9, where the middle fraction is combined with the lumps.

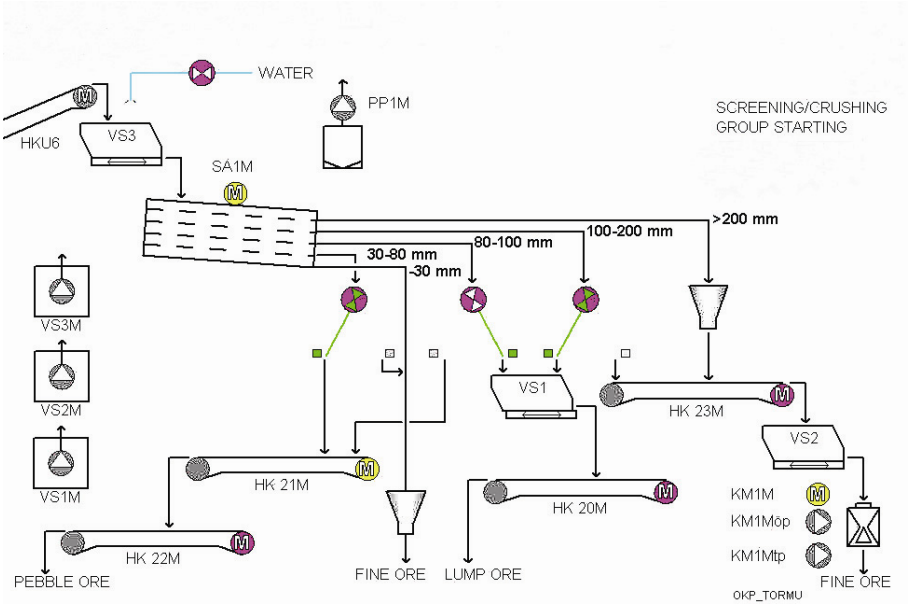

Fig. 3.9 Screening station and ore bins. (courtesy of Pyhäsalmi Mine Oy)

During normal operation the amount of oversized particles is very small, less than 1 ton/h, whereas the feed rate for the flotation plant is typically 160-170 tons/h.

Grinding

Grinding is carried out in rotating mills (see Fig. 3.10), where the ore is mixed with water. In the first of the three phases, the lumps and fine ore are mixed together (LM2 in Fig. 3.11). The larger particles receive more kinetic energy and act as *grinding media* while grinding the ore. This is called *autogenous grinding* (AG). However, for the impacts to be efficient there must be different particles sizes colliding with each other in correct proportions. This is why iron balls are added to the first stage, leading to *semi autogenous grinding* (SAG).

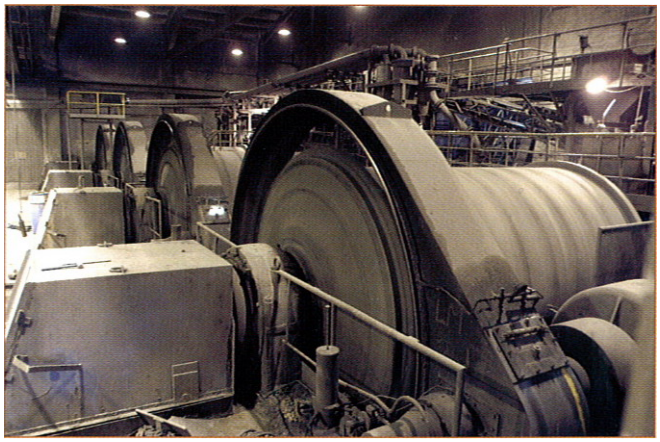

Fig. 3.10 Grinding mills used in Pyhäsalmi. (courtesy of Pyhäsalmi Mine Oy)

The second grinding stage consists of three mills (PM1, PM2 and PM3 in Fig. 3.11). This stage is fed with the output of the first phase and additional pebble ore is used as grinding media. Iron balls are typically used also in this stage but, if the ore coming from the mine is favourable in terms of particle size distribution and mineralogy, the second stage can be driven in completely autogenous mode. This is one of the motivations for the development of the particle size distribution analysis system, described in Chapter 4.

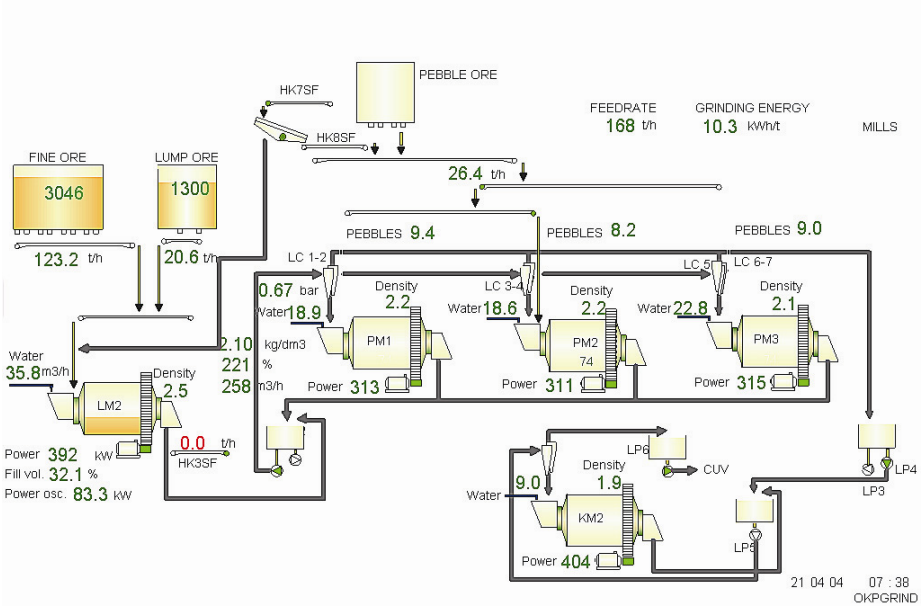

Fig. 3.11 Grinding circuit. (courtesy of Pyhäsalmi Mine Oy)

The coarsest particles are separated with hydro-cyclones and returned back to the second stage. Fines continue to the third stage (KM2 in Fig. 3.11, which is an overflow ball mill). The purpose of the last stage is to ensure that 65% of the ground ore is less than 74 μm in size [60]. This will ensure good product quality for the subsequent copper circuit in the flotation stage.

Flotation

The grinding stage is followed by a three phase flotation circuit, where copper, zinc and sulphur are floated respectively. Flotation is a complex physico-chemical process where surface properties of the floated minerals are modified in a way that they will become *hydrophobic* and attach to the surfaces of rising air bubbles. This takes place in a flotation cell (see Fig. 3.12), where the minerals are mixed with water as well as other chemicals and air is dispersed through a rotating axle in order to form an evenly rising bubble flux. When the valuable mineral is floated and the invaluable gangue is left in the tailings, which is the more common case, then one is dealing with *direct flotation*. The opposite where invaluable material is floated, like ink in waste paper recycling, for example, is called *reverse flotation*.

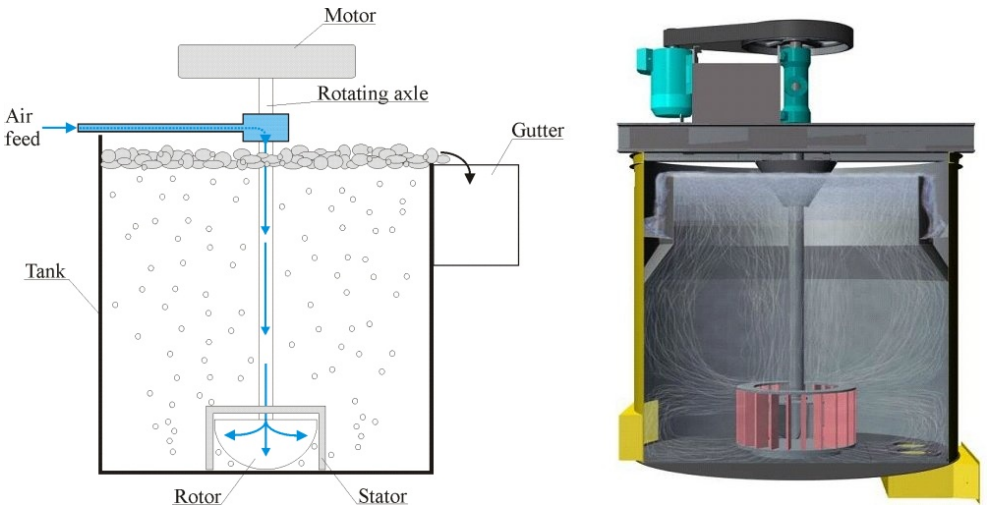

Fig. 3.12 Main parts of a flotation cell (left) and a CAD image of a modern flotation cell (right). (CAD image courtesy of Outotec Minerals Oy)

Flotation as a minerals processing method was originally patented in 1906 and the subject has been studied intensively ever since (see e.g. [13], [22], [47], [53], [87], [104]). This is mainly because flotation takes place in three phases (solids, water, and air) and is so complex in nature that all interactions and phenomena related to it are not fully understood. The following discussion gives a brief introduction to the very basics at the particle level.

To get an individual mineral particle to the concentrate stream, that particular particle must attach itself on the surface of a rising air bubble, as mentioned earlier.

In order to do that the forces acting on the bubble in the pulp must be in favour of the attachment. The *tensile forces* acting between an air bubble and a particle in an aqueous medium, shown in Fig. 3.13, are dependent on solid-air (s/a), water-air (w/a) and solid-water (s/w) surface energies.

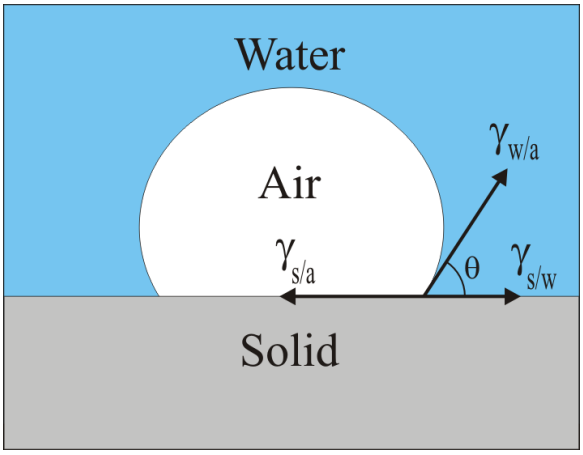

Fig. 3.13 Tensile forces and contact angle between bubble and particle. (reproduced from [110])

At equilibrium, the following equation holds

$$\gamma_{s/a} = \gamma_{s/w} + \gamma_{w/a}\cos(\theta) \tag{1}$$

where $\gamma_{s/a}$, $\gamma_{s/w}$ and $\gamma_{w/a}$ are the above mentioned surface energies and θ is the contact angle between the mineral particle and the air bubble. In order to remove the particle from the surface of the air bubble, the solid-air interface must be broken and new water-air and solid-water interfaces must be formed. This is defined by *work of adhesion* $W_{s/a}$ [110] as

$$W_{s/a} = \gamma_{w/a} + \gamma_{s/w} - \gamma_{s/a} \tag{2}$$

and when combined with (1) yields

$$W_{s/a} = \gamma_{w/a}\left(1 - \cos(\theta)\right) \tag{3}$$

From this it can be seen that as the contact angle increases also the force that is required to break the bond is increased. Consequently, the contact angle can be used as a measure of hydrophobicity. The term *aerophilic* is also often used in this context, meaning that hydrophobic (or aerophilic) particles favour air over water, which in turn leads to a stronger bond and to a higher contact angle. [110]

The hydrophobicity of the floated particles is controlled by *flotation reagents*. *Frothers* are used to produce stable froth. Pine oil is used in Pyhäsalmi as a frother. *Collectors* are used to selectively render the desired particles hydrophobic and thus cause them to attach to the rising bubbles. This is achieved by adsorbing to the

surface of the particle and causing hydrophobicity. In Pyhäsalmi, *Sodium Isobutyl Xanthate (NaIBX)* is used as a collector. However, Xanthate molecules do not naturally attach themselves to the surface of the zinc mineral particles. This is why the zinc particles are first treated with *copper sulphate* ($CuSO_4$), which is used as an *activator*. The purpose is to get the particles coated with copper ions, which can be collected with Xanthate. The final group of flotation reagents are *regulators* which are used to control the flotation process. They can be used, for example, to depress unwanted particles from attaching to the surfaces of the air bubbles. In Pyhäsalmi, *Calcium hydroxide* (CaOH) is used in this manner to control the pH of the pulp. [40], [110]

Copper, Zinc and Pyrite Circuits

Snapshots from the mine's automation system presenting the copper, zinc and pyrite flotation circuits are shown in Fig. 3.14, Fig. 3.15 and Fig. 3.16, respectively. Copper and pyrite circuits are briefly introduced and a more thorough description of the zinc circuit is given because most of the work related to flotation was carried out in the zinc circuit. The reader should note that a common notation in the images is that concentrates are leaving downwards (often from a tip of a triangular shape) and tailings to the left or right.

The copper circuit (Fig. 3.14) consists of conventional *rougher* (CuEV) and *scavenger* (CuRV) banks that are followed by several *cleaning* stages, resulting in a final copper product extracted from final cleaner cell (VK39, indicated with an arrow). The VK39 is equipped with a camera that is used for closed loop control as will be shown later in this thesis. The tailings are collected into one flow and together they form a feed flow for the following zinc circuit (ZnV near the right edge of the image).

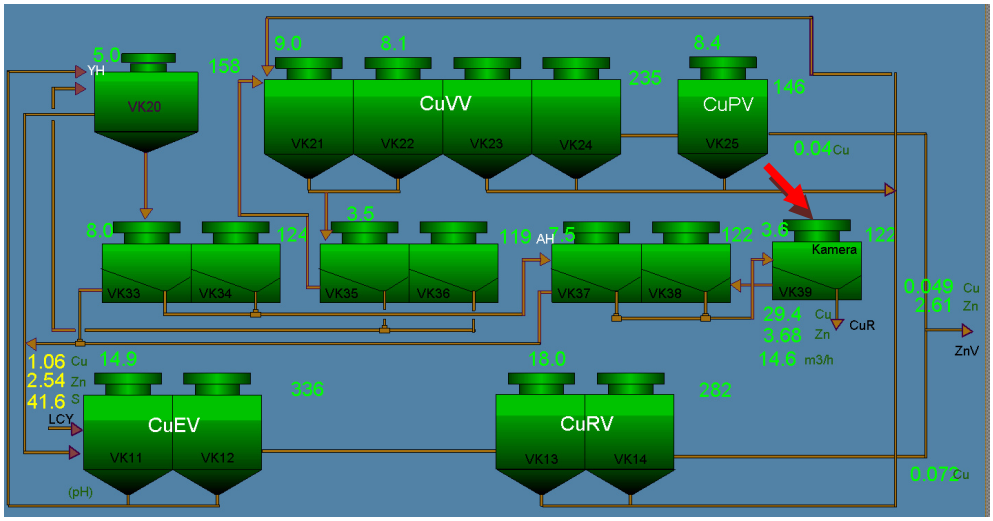

Fig. 3.14 Copper flotation circuit. Camera location for the final copper product is marked with an arrow. (courtesy of Pyhäsalmi Mine Oy)

The zinc circuit consists of the following stages: *roughing*, *scavenging*, *mid-roughing*, *mid-scavenging*, *re-grinding* and *cleaning*, as indicated in Fig. 3.15. The purpose of the rougher bank (four cells) is to recover as much zinc as possible, meaning that recovery is preferred over grade. The concentrate from the first two cells is fed directly to the cleaning stage (i.e. from A to C) and the remaining two cells are used for scavenging, where the recovery of the whole circuit is maximized.

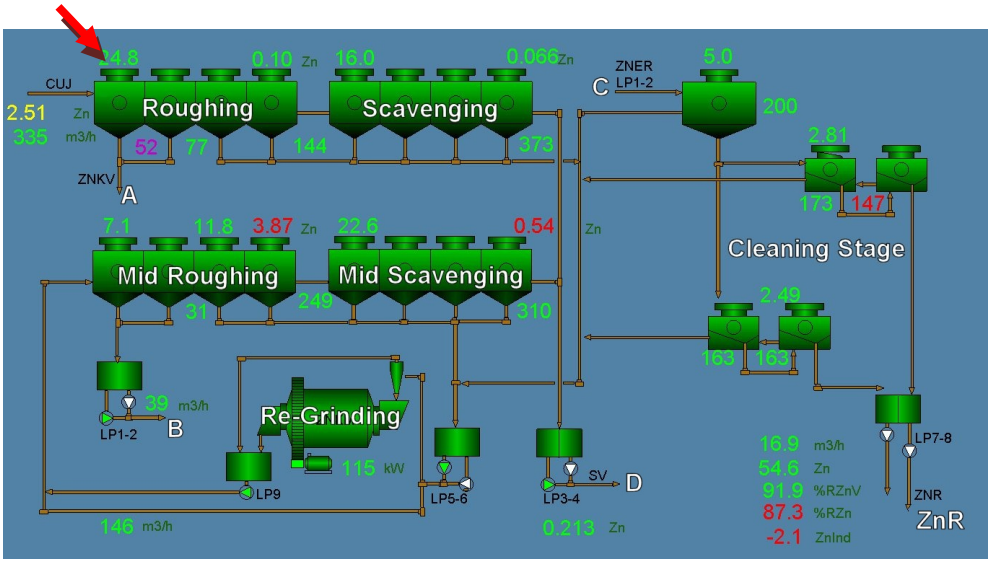

Fig. 3.15 Zinc flotation circuit. Camera location of the single cell analysis point is marked with an arrow. (courtesy of Pyhäsalmi Mine Oy)

The mid-roughing and mid-scavenging circuits are a part of a re-grinding loop where the material flow is classified into coarse and fine fractions with hydrocyclones and the resulting coarse fraction is re-ground to a smaller particle size. Feed flow for the cleaning leaves from the first two cells of the mid-roughing circuit (i.e. from B to C).

In the cleaning stage the grade is emphasized over recovery. As shown in Fig. 3.15, there are two cells producing the final product (ZnR). The tailings of those cells are circulated back to the previous cells and the tailings of the remaining cells are returned to the classification stage.

The tailings of the zinc circuit (D) are routed to the following pyrite circuit (Fig. 3.16), which is included here only to have a complete picture of the flotation process. The work presented in this thesis does not include research on the pyrite circuit.

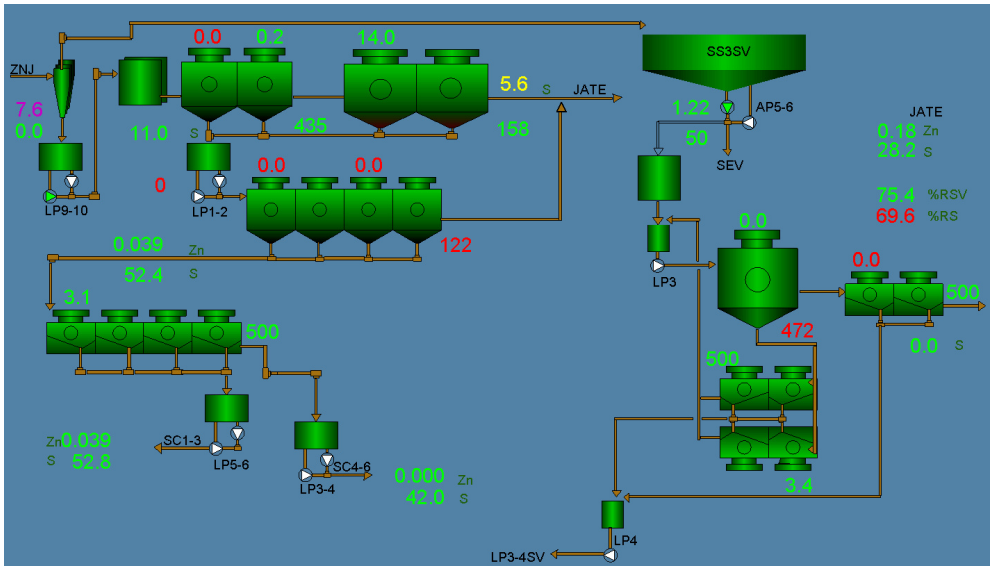

Fig. 3.16 Pyrite flotation circuit. (courtesy of Pyhäsalmi Mine Oy)

Dewatering

After flotation, all concentrates are dried to a 5-7% moisture content. For all concentrates the dewatering procedure starts by thickening, where the solid material settles to bottom (see Fig. 3.8). Most of the water is removed in this phase. After this, separate methods are used for the three concentrates. Copper concentrate is dried by using ceramic filters (see Fig. 3.17), which are based on under pressurized micro porous ceramic discs and capillary action. The discs are slowly rotated in the concentrate slurry, leaving a relatively dry concentrate on the surface of the disks from where it is finally scraped off as a copper concentrate.

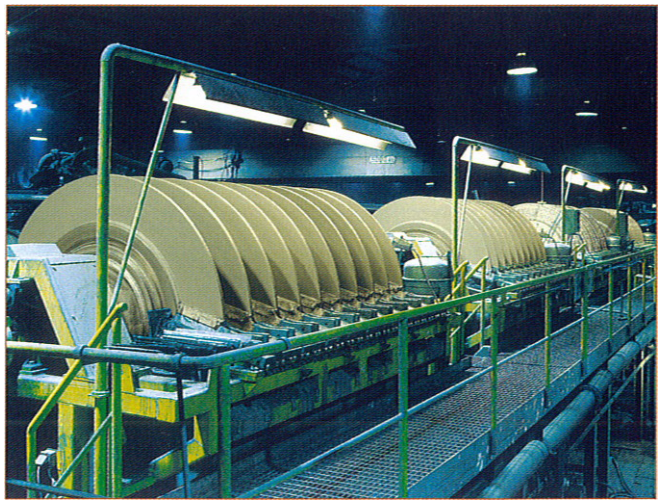

Fig. 3.17 Ceramic filters. (courtesy of Pyhäsalmi Mine Oy)

In addition to ceramic filters, a press filter is used to remove water from the pyrite concentrate. The press filter removes water by applying a large compressing force and a compressed air flow to a 10 ton concentrate batch at a time. The total capacity of the filter is 50 tons/h.

The zinc concentrate is dried by using a similar press filter.

Tailings Disposal

Since the litospherical forces acting on the earth's crust in Pyhäsalmi are roughly twice as high as the pressure caused by 1400 meters of rock from above, all openings in the mine must be quickly supported or backfilled. Therefore, the coarser fraction of the flotation tailings (see Fig. 3.8) is transported back to the mine and used for filling. The finer part is pumped in sequence into three settling ponds with a total area of 110 hectares, where the solids are settled into the bottom and the remaining clarified and the neutralized effluent can be released into Lake Pyhäjärvi [46].

4.
Particle Size Distribution Analysis

This chapter describes the shadow based particle size analysis system and the evolution to its current state, where the measurement is based on commercial 3D laser scanner and a belt weigher. The size range considered in this thesis covers particle sizes that are typically present on moving conveyor belts in the mining, mineral and metal industry (MMMI), say 1 mm to 500 mm in diameter. Thus, the title must not be confused with the particle size analysis and analyzers covering flotation streams (like the Outotec PSI 500™ analyzer [56], for example). The text is based on publications [P2] and [P7]. The additional neural network validation reported in Section 4.2.5 was carried out by M. Larinkari.

4.1. Motivation & Initial Considerations

Particle size distribution is important information in the MMMI. However, it is especially important in the context of autogenous- or semi autogenous grinding processes, because the crushed ore itself is used as a grinding media (see e.g. [30] and [71]). Different size classes must be available and must be fed to grinding mills in correct proportions in order to maintain effective autogenous grinding performance. If this is not the case, additional grinding media must be added or decreased performance will lead to substantial economical losses. In Pyhäsalmi, differently sized iron balls are used as additional grinding media.

As explained in Subsection 3.3.2, the secondary grinding circuit in Pyhäsalmi can be run in completely autogenous fashion, provided that the particle size distribution coming from the mine is favourable. This would lead to savings in iron ball consumption. In fact, the grinding experts in Pyhäsalmi have estimated that some 20% savings could be achieved from the 1 000 000 Euros per annum used for iron balls if there would be correct size classes in the silos at all times.

In order to be able to know, and possibly influence, the size distribution that will be accumulated into the fine ore, pebble ore and lump ore silos after the screening station, one would need an indication of the size distribution that is coming from

the mine. Since the ore transportation chain from the mine to the surface contains intermediate silos with a total capacity of around 10 000 tons, and since the average feed rate to the concentrator plant is close to 160 ton/h, the delay caused by the ore transportation system varies in the range of 1-3 days, depending on the silo levels and the utilization rate of the hoist. Thus, the best possible place to make size distribution measurements would be right after the first crushing stage that is located in the mine, since it is the place where the size distribution is formed. If this distribution would be known, it would give an indication of the future changes in the size distribution at the grinding station some 1-3 days in advance. With this information the silo levels could be predicted and, if needed, possible corrective actions made in advance. The corrective actions were initially supposed to be made by controlling the jaw distance of the crusher, but during the research it was noted that the fan distance used in blasting had a significant effect on the size distribution, as reported by Larinkari [60]. Therefore, the control should be based on a combination of the fan distance and the jaw setting, meaning that the new information could be utilized also in mine planning.

For these reasons Pyhäsalmi Mine Oy made an initiative for the development of a new instrument that would be capable of measuring the size distribution of ore coming from the primary crusher.

4.1.1. Considered approaches

Based on the initial studies regarding the crusher and the mine in general, it was clear that the new measurement system would have to endure harsh conditions including dust, moisture, vibrations, and shocks caused by blasting. This, combined with the importance of imaging in machine vision applications, made it clear that the system would have to be especially robust against external variations.

At first, a *segmentation* based method was considered either from an image taken of the conveyor belt (location shown in Fig. 3.4) or of the falling ore at the end of the belt (see right part of Fig. 4.1). Segmentation is a method which divides an image into several regions of interest based on the problem at hand. In this case relevant regions would be individual rock particles. However, as Gonzalez and Woods [23] state: *"Segmentation of nontrivial images is one of the most difficult tasks in image processing. Segmentation accuracy determines the eventual success or failure of computerized analysis procedures. For this reason, considerable care should be taken to improve the probability of rugged segmentation. In some situations, such as industrial inspection applications, at least some measure of control over the environment is possible at all times"*. This implies that segmentation in itself is an excellent method to accomplish certain image analysis tasks, but it is vulnerable to undesired variation in the source data. In practice, this means that the imaging conditions must be kept constant, which in this case would be difficult because of dusting and lamp aging, for example.

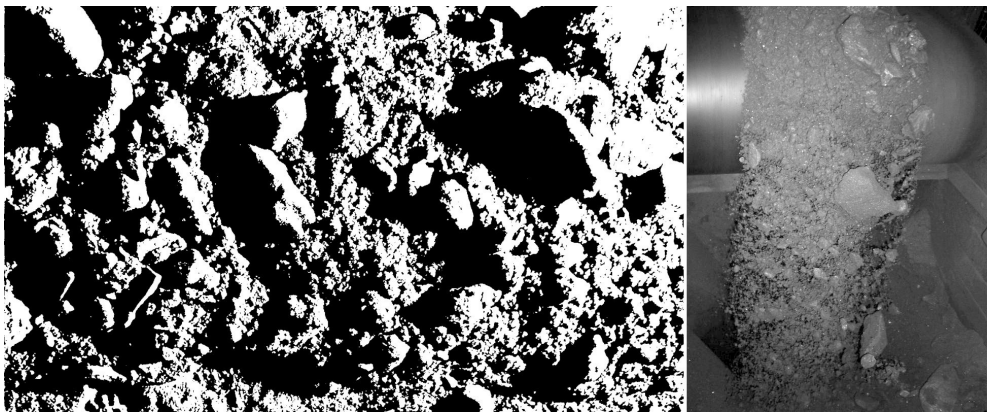

Fig. 4.1 The two approaches considered; shadow lengths (left) and segmentation from falling ore (right).

When considering these issues, another novel idea was proposed by Hyötyniemi [36]. It was based on a simple idea that, if illuminated with a single light source at a relatively shallow angle, the larger particles will throw longer shadows than the smaller particles, as illustrated in the left part of the Fig. 4.1. And since there would be large amounts of image data available, a calibration model could be taught to grasp the particle size information from this statistical data. The best thing in this approach was robustness to external conditions. This was because the only thing needed was information from each location (i.e. pixel) of the image stating whether that location had shadow in it or something else. This information could be obtained by a simple *thresholding* operation as shown below.

$$I_{binary}(i,j) = f_b\left(I(i,j),K\right) = \begin{cases} 1, & if \quad I(i,j) < K \\ 0, & if \quad I(i,j) \geq K \end{cases} \quad \forall \quad i,j \begin{cases} i \in \{1,\ldots,N_R\} \\ j \in \{1,\ldots,N_C\} \end{cases} \tag{4}$$

where I is a two dimensional greyscale image and K is the thresholding value. N_R and N_C are number rows and columns in the image, respectively. Since there are clear intensity changes between dark shadows and other illuminated areas, as can be seen in the left part of the Fig. 4.1, it is easy to find a fixed value for K so that it will be valid in all operating conditions.

4.2. Shadow Based Analysis

Since the shadow based approach seemed so well suited and promising for the problem at hand, it was decided that such a system would be constructed and tested in Pyhäsalmi mine. Installation was decided to reside on top of the HKU2 conveyor belt located just after the primary crusher, as indicated in Fig. 3.4. However, the shadow based approach was first tested with a portable halogen lamp and a digital camera. The digital images were analyzed by thresholding them into binary images and by calculating their shadow length histograms (in a similar manner as to be explained later in Subsection 4.2.3). The histograms were then analyzed against the

captured images to gain a subjective impression of whether or not the approach would be feasible.

4.2.1. Selected System Setup

Once the feasibility study confirmed that there exists a strong enough correlation between the shadow lengths and the particle size distribution, a fixed system setup was designed and implemented in the mine. The system consists of a monochrome camera installed on top of a conveyor belt and a light source illuminating the ore bed at a shallow angle from the side, as shown in Fig. 4.2. A halogen lamp (1000W) was selected as a light source, and imaging was carried out with a Sony XC-55 monochrome CCD camera that supports *progressive scanning*.

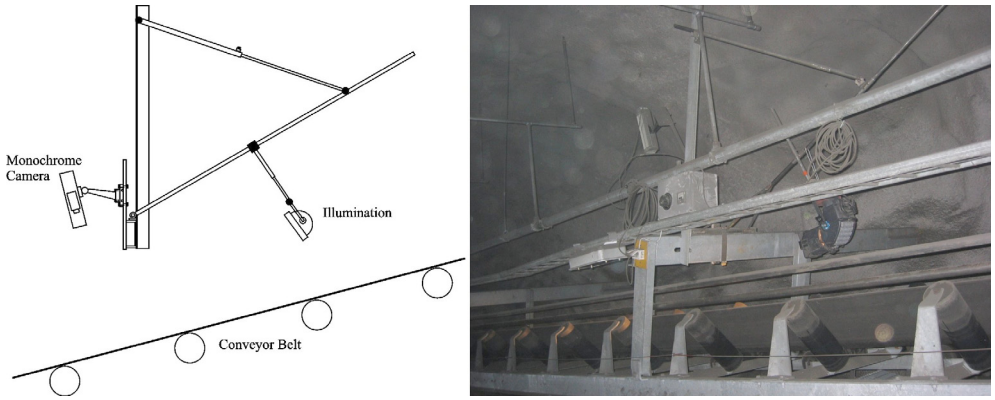

Fig. 4.2 Original system setup for the shadow based analysis.

Progressive scanning is an imaging method, where the CCD cell of the camera is read in one sequence as opposed to conventional *interlaced scanning* where odd lines and then even lines of each frame are read consecutively. Progressive scanning ensures sharp images when imaging moving objects, as in this case. Even though the speed of the belt is only 1 m/s, it can still introduce an error of 2-3 pixels with interlaced cameras. The shutter time of 1/2000 seconds was used, which means that the belt moved 0.5 mm while integrating an image to the CCD cell. The intensity fluctuations of the 50 Hz alternating current driving the halogen lamp caused intensity variations in the captured images depending on the phase of the sine wave, in which the imaging happened to take place. This could have been compensated for by synchronizing image capture with the phase changes of the alternating current or by calculating an individual thresholding value for every captured image. However, synchronization was thought to be too complex (although it eventually had to be done, as shown later) and individual thresholding was also a feature that was not desired. Therefore, stable illumination was realized with an adjustable direct current converter.

4.2.2. Image Analysis

The images were captured in a CCIR-format, which is a greyscale image standard similar to the PAL standard that is commonly used for colour images. The image grabbing was carried out with a Matrox Meteor II Multichannel™ grabber card that was attached to a standard desktop PC running Windows NT 4.0™ operating system. This resulted in 640x480 sized images with a colour depth of 8 bits (i.e. 256 different greyscale values for each pixel). An example of such an image is shown in Fig. 4.3 below.

As can be seen, the image is fairly sharp and there is a good contrast between the shadows and other elements in the image. Furthermore, because of the stabilized illumination there were no fluctuations in intensity between consecutive images. This was a good starting point for further image analysis.

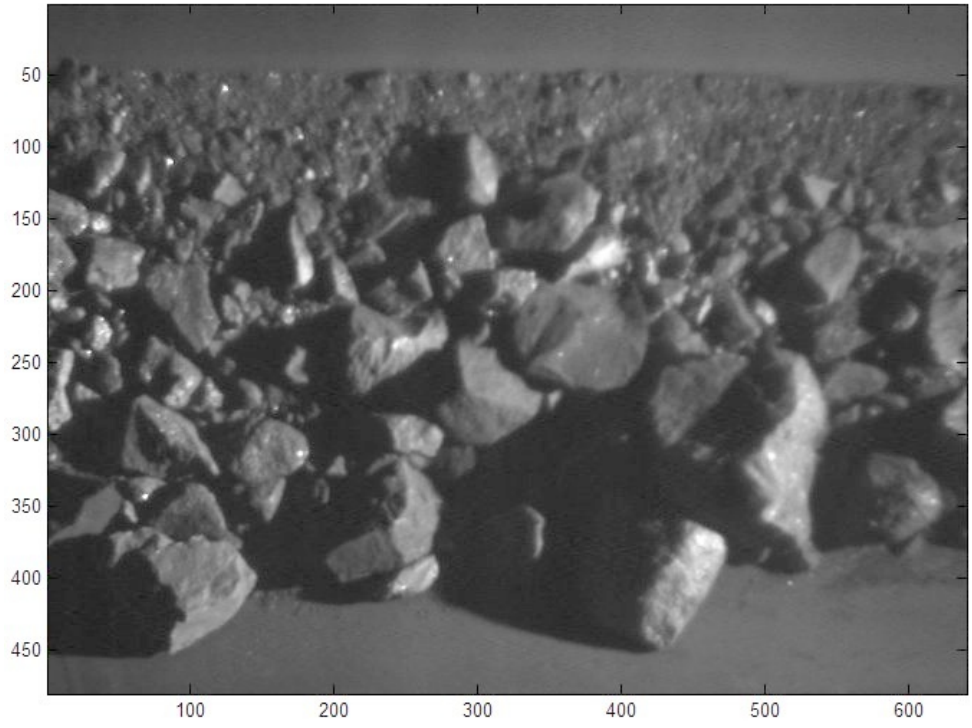

Fig. 4.3 Grabbed shadow image.

The next step was to emphasize the shadows, which was carried out by thresholding the image (see left part of Fig. 4.4). Although the intensity variations were dealt with, there were still the effects of dusting and lamp aging to be taken into consideration in order to achieve reliable long term operation. These two contribute to a slow drift in image intensity and, if a fixed thresholding value would have been used, also to diminished robustness. To compensate for this, a

threshold adaptation method was devised. Adaptation is based on the fact that, due to the cross sectional shape of the conveyor belt (see e.g. Fig. 4.18), the upper and lower parts of the image are always free of ore particles and can be used as a reference area for illumination intensity. Thus, small bands (see Fig. 4.4) were selected as a calibration area I_C and the thresholding value K was selected so that it fulfilled the equation

$$\frac{\sum_{i=1}^{N_R}\left(\sum_{j=1}^{N_C} f_b\left(I_C(i,j),K\right)\right)}{N_R N_C} < 0.02, \quad \begin{cases} i \in \{1,\ldots,N_R\} \\ j \in \{1,\ldots,N_C\} \end{cases} \tag{5}$$

where N_R and N_C are number of rows and columns, respectively, and the function f_b is defined as in (4). Since the illumination in the images is coming from the right, this leads to black pixels emerging from the left, as can be seen in the upper left part in Fig. 4.4.

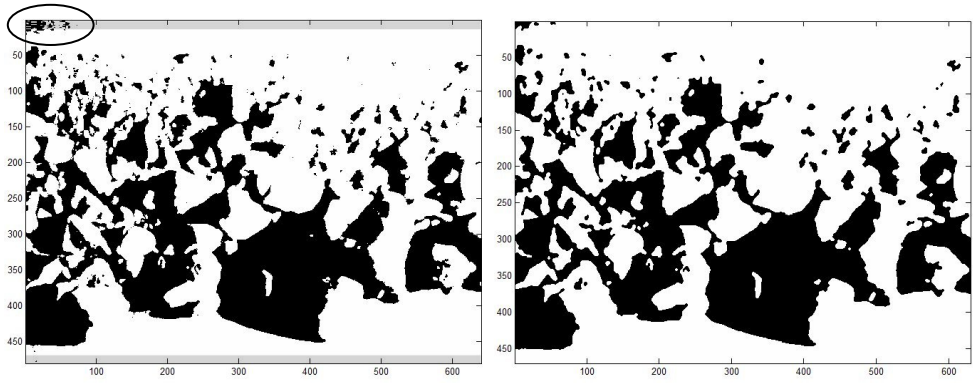

Fig. 4.4 Thresholded (left) and median filtered (right) images. Threshold adaptation areas (light grey) are shown in the left image, where the emerging black pixels are circled.

In order to get rid of noise in the image, median filtering was applied three times in a row with a mask size of 3x3. Median filtering for a binary image can be done by running the centre point of the mask over every pixel in the image and calculating the sum of pixels under the mask. If the sum is greater than 4, the centre pixel in the filtered image will have a value of 1, otherwise it will have the value 0 [23]. A nice feature of the median filtering algorithm is that it converges to a final image. In this case, it was simply a question of selecting the number of rounds needed for satisfactory results (here, three was found sufficient). A bigger mask would "clean out" larger areas, but again, a mask of size 3x3 was found to be best for this application.

A final step, before calculation of the shadow histogram, was to detect the edges of the ore bed. This was carried out by a heuristic algorithm that is illustrated in Fig. 4.5.

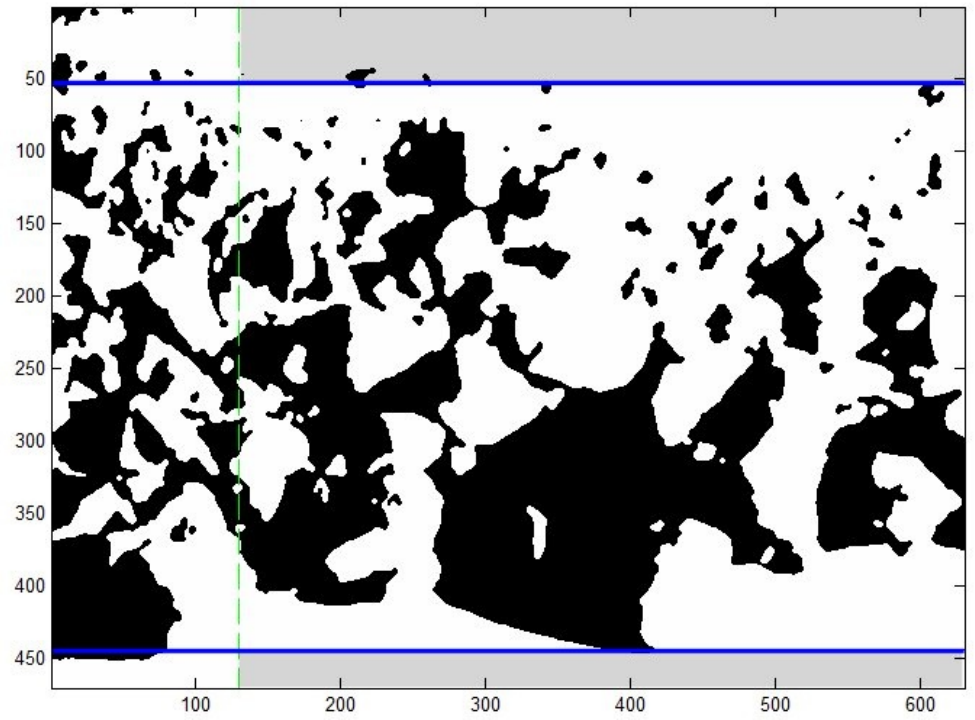

Fig. 4.5 Ore detection areas (light grey). Detected ore borders are indicated with the blue lines.

Consider the detection of the upper boundary (the lower is similar). The algorithm starts to slide a horizontal line (blue) from the top dividing the image into two parts. The upper part is further divided by a vertical line (dashed green) in order to get rid of the previously mentioned emerging black areas caused by the threshold adaptation algorithm. Now, the emphasized (light grey) area is what is left and this area grows as the blue line moves down. The area of shadows (i.e. black pixels) is calculated in a similar fashion as in (5) and once it reaches 4%, the edge of the ore bed is found.

4.2.3. Shadow Histogram Calculations

The shadow lengths of the resulting manipulated image are calculated and stored to a vector $\mathbf{v}_S = 0$ of length N_C by traversing each horizontal line and searching for continuous black pixels. Once a shadow of length l is found, its length is compensated for by

$$l_C = \frac{l}{1 + \frac{L_2}{L_1} x_R} \tag{6}$$

where $L_1 = 122\,\text{cm}$ is the distance between the lamp and the upper edge of the imaging area, $L_2 = 110\,\text{cm}$ is the length of the imaging area and x_R is the place of the rock in the image, as illustrated in Fig. 4.6 below.

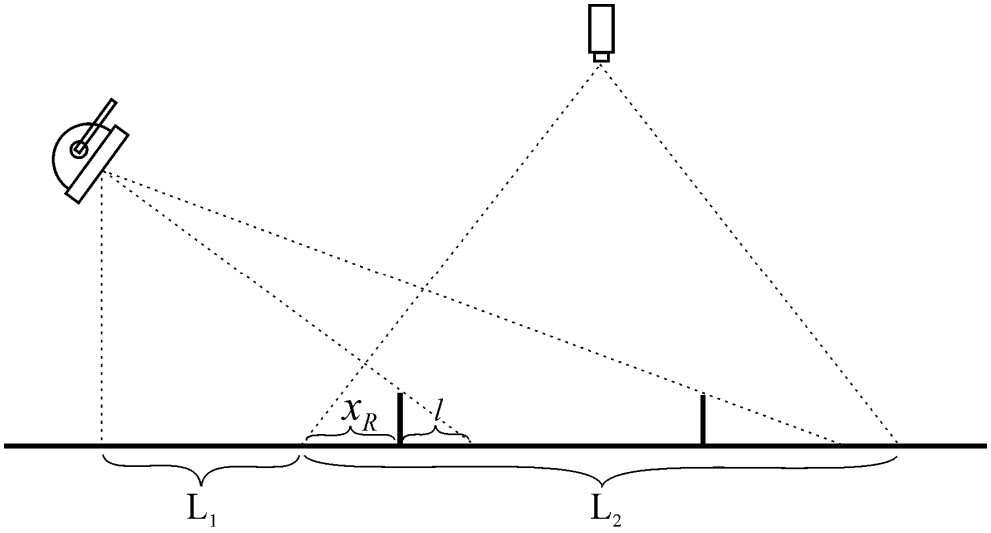

Fig. 4.6 An illustration of the shadow length distortion effect.

The compensated length l_C is then rounded to the nearest integer and stored to the shadow length distribution by

$$\mathbf{v}_{S,new}(l_C) = \mathbf{v}_S(l_C) + 1 \tag{7}$$

4.2.4. Data Collection & Modelling

In order to get a mapping between the shadow distribution and real life particle size proportions, a calibration model was needed. And before such a model could be estimated, a data set describing these dependencies would have to be available. There was no easy way to get this type of data since – at least in Pyhäsalmi – it is quite difficult to get a side stream of the material flow for analysis. And furthermore, even if such an ore stream would be available, the volume and tonnage would quickly become very large, and there would have to be synchronized image data describing its appearance on the conveyor belt. This is why the calibration data had to be collected manually.

A separate stand was built next to the conveyor belt and data points were collected by stopping the conveyor belt, storing a shadow image, shovelling the ore under the imaged area into buckets, weighing the sample and screening it to acquire size class proportions (Fig. 4.7).

Two different data sets were collected in this manner. The first data set consisted of 100 samples that were obtained by running the crusher jaws in five different settings and collecting 20 samples with each setting. The average sample size was 150 kg, resulting in 15 tons of processed ore. The second data set, obtained at a later stage and used for *neural network* modelling, contained another 150 samples.

Fig. 4.7 A "data mining" campaign in the spring of 2004.

After the data was acquired, two different modelling approaches were tested, namely *Partial Least Squares* (PLS) and a neural network. The first intuition was that PLS would be appropriate modelling technique for this application, but in order to test this hypothesis, a neural network model was obtained and the results were compared to those obtained by the PLS method. In the following sections, these two approaches are discussed.

Partial Least Squares Model

Partial Least Squares (PLS) regression was first introduced by the Swedish statistician Herman Wold. It is a linear method that attempts to find factors that capture variance in the *predictor variables* $\mathbf{X}$ and at the same time achieve correlation with the *predicted variables* $\mathbf{Y}$. Typically, the PLS model projects the $\mathbf{X}$ data into lower dimensional Z^1 oriented *subspace* in a similar manner as in *Principal Component Analysis* (PCA) method, that will be used later in this thesis. However, instead of maximizing the *variance* with respect to the predictor variables $\mathbf{X}$, the internal structure of the $\mathbf{Y}$ block is also searched for [37].

The PCA and PLS analysis in this thesis was carried out by using the MATLAB™ software and an additional PLS toolbox provided by Eigenvector Research Inc. For the PLS part, a commonly used SIMPLS algorithm, developed by Sijmen de Jong [15] was used. However, even though the algorithm is superior in performance, it is highly non-intuitive. Thus, the introduction to the PLS method is given through a description of the NIPALS (Non-Iterative Partial Least Squares) algorithm that gives exactly the same results in the case of a univariate $\mathbf{Y}$ block (i.e. y-side is a column vector $\mathbf{y}$) and slightly different results for the general multivariate case. The introduction is adopted from [113]. For a more thorough review of the subject, the reader is referred to [19], [43], [66], [69], [114], [115] and [116].

Since both PCA and PLS are used in this thesis, the introduction is started with PCA and then extended to cover PLS.

In the PCA method, the data matrix $\mathbf{X}$ (with *m* rows and *n* columns, containing the measurements and the variables, respectively) is decomposed into *sum of the outer product* of vectors $\mathbf{t}_i$ (row vector of *m* elements) and $\mathbf{p}_i$ (row vector of *n* elements), plus a *residual matrix* $\mathbf{E}$ as follows

$$\mathbf{X} = \mathbf{t}_1\mathbf{p}_1^T + \mathbf{t}_2\mathbf{p}_2^T + \mathbf{t}_3\mathbf{p}_3^T + \ldots + \mathbf{t}_k\mathbf{p}_k^T + \mathbf{E} \tag{8}$$

where *k* corresponds to the dimension of the reduced subspace, or the number of *latent variables* and $k \le \min\{m,n\}$. The $\mathbf{t}_i$ vectors contain information on how the *samples* relate to each other and are known as *scores*. The $\mathbf{p}_i$ vectors, on the other hand, contain information on how the *variables* relate to each other and they are called *loadings*. Loadings are *eigenvectors* of the *covariance matrix* of $\mathbf{X}$, i.e. for each $\mathbf{p}_i$

$$\mathrm{cov}(\mathbf{X})\mathbf{p}_i = \left(\frac{\mathbf{X}^T\mathbf{X}}{m-1}\right)\mathbf{p}_i = \lambda_i\mathbf{p}_i \tag{9}$$

where λ_i is the *eigenvalue* of $\mathrm{cov}(\mathbf{X})$ associated with the eigenvector $\mathbf{p}_i$. Note that $\mathbf{X}$ is assumed to be adjusted to *zero mean* and to *unit variance*, i.e. the mean value of each column is subtracted and the variance set to one by dividing each column by its standard deviation.

The $\mathbf{t}_i$ vectors form an *orthogonal* set, meaning that

$$\mathbf{t}_i^T\mathbf{t}_j = 0 \quad \forall \quad i \ne j \tag{10}$$

and the $\mathbf{p}_i$ are *orthonormal*

$$\begin{cases} \mathbf{p}_i^T\mathbf{p}_j = 0 & \forall \quad i \ne j \\ \mathbf{p}_i^T\mathbf{p}_j = 1 & \forall \quad i = j \end{cases} \tag{11}$$

Furthermore, for any $\mathbf{t}_i$, $\mathbf{p}_i$ pair

$$\mathbf{X}\mathbf{p}_i = \mathbf{t}_i \tag{12}$$

saying that the score vector $\mathbf{t}_i$ is a linear combination of the original $\mathbf{X}$ data defined by the loadings vector $\mathbf{p}_i$. This means that the score vectors are a projection of $\mathbf{X}$ into a lower dimensional Z^1 oriented subspace spanned by the loading vector $\mathbf{p}_i$.

The $\mathbf{t}_1, \mathbf{p}_1$ pairs are arranged in descending order of λ_i, meaning that the first pair captures the greatest amount of variation present in the data, the second pair

captures the second largest amount of variation in an orthogonal direction with respect to $\mathbf{t}_1, \mathbf{p}_1$ and so on. Since variance in the data can be considered as information, this method effectively captures the most relevant information present in the data while reducing its dimension.

In the PLS case, similar scores $\mathbf{T} = [\mathbf{t}_1, \mathbf{t}_2, \cdots, \mathbf{t}_k]$ and loadings $\mathbf{P} = [\mathbf{p}_1, \mathbf{p}_2, \cdots, \mathbf{p}_k]$ are calculated, as well as an additional set of *weights* $\mathbf{W}$ ($n \times k$ matrix) that are required to maintain orthogonal scores. However, the $\mathbf{T}$ and $\mathbf{P}$ do not have exactly the same meaning as in the PCA case. Instead, they can be thought of as PCA scores and loadings that have been rotated to be more relevant for predicting $\mathbf{Y}$ (i.e. for obtaining the estimate $\hat{\mathbf{Y}}$).

The NIPALS algorithm works also for multivariate $\mathbf{Y}$ and, therefore, the scores $\mathbf{U}$ and the loadings $\mathbf{Q}$ are also calculated for the $\mathbf{Y}$ block. In addition, a vector of *inner relationship coefficients* $\mathbf{b}$ is calculated. This relates the $\mathbf{T}$ and $\mathbf{U}$ scores.

The algorithm is started by selecting one column of $\mathbf{Y}$, usually the one with the highest variance, as the starting estimate $\mathbf{u}_1$. Then for the $\mathbf{X}$ side, the weight $\mathbf{w}_1$ and score $\mathbf{t}_1$ are updated:

$$\mathbf{w}_1 = \frac{\mathbf{X}^T \mathbf{u}_1}{\left\| \mathbf{X}^T \mathbf{u}_1 \right\|} \tag{13}$$

$$\mathbf{t}_1 = \mathbf{X}\mathbf{w}_1 \tag{14}$$

Similarly for the $\mathbf{Y}$ side:

$$\mathbf{q}_1 = \frac{\mathbf{u}_1^T \mathbf{t}_1}{\left\| \mathbf{u}_1^T \mathbf{t}_1 \right\|} \tag{15}$$

$$\mathbf{u}_1 = \mathbf{Y}\mathbf{q}_1 \tag{16}$$

These values are updated in sequence by using $\mathbf{u}_1$ from (16) in the next round of (13). Once $\mathbf{t}_1$ in (14) converges to a constant value (within a rounding error), the $\mathbf{X}$ loadings are calculated and the scores and weights are rescaled:

$$\mathbf{p}_1 = \frac{\mathbf{X}^T \mathbf{t}_1}{\left\| \mathbf{t}_1^T \mathbf{t}_1 \right\|} \tag{17}$$

$$\mathbf{p}_{1,new} = \frac{\mathbf{p}_1}{\left\| \mathbf{p}_1 \right\|} \tag{18}$$

$$\mathbf{t}_{1,new} = \mathbf{t}_1 \left\| \mathbf{p}_1 \right\| \tag{19}$$

$$\mathbf{w}_{1,new} = \mathbf{w}_1 \left\| \mathbf{p}_1 \right\| \tag{20}$$

Then the regression coefficient for the inner relation is calculated as

$$b_1 = \frac{\mathbf{u}_1^T \mathbf{t}_1}{\mathbf{t}_1^T \mathbf{t}_1} \tag{21}$$

Now, the scores and loadings are calculated for the first factor, commonly called a *latent variable* (LV). The residuals for $\mathbf{X}$ and $\mathbf{Y}$ blocks are calculated as

$$\mathbf{E}_1 = \mathbf{X} - \mathbf{t}_1 \mathbf{p}_1^T \tag{22}$$

$$\mathbf{F}_1 = \mathbf{Y} - b_1 \mathbf{t}_1 \mathbf{q}_1^T \tag{23}$$

For the following latent variables, the $\mathbf{E}_1$ and $\mathbf{F}_1$ are used in place of $\mathbf{X}$ and $\mathbf{Y}$, respectively, the subscripts are incremented by one and the entire procedure is restarted from (13).

The final goal is to find a *regression matrix* $\mathbf{B}_R$ containing the weights used for the linear combination of $\mathbf{X}$ in order to produce an estimate of $\mathbf{Y}$:

$$\hat{\mathbf{Y}} = \mathbf{X}\mathbf{B}_R \tag{24}$$

It can be shown [113] that, based on the calculations above, $\mathbf{B}_R$ can be calculated as

$$\mathbf{B}_R = \mathbf{W}\left(\mathbf{P}^T \mathbf{W}\right)^{-1} \left(\mathbf{T}^T \mathbf{T}\right)^{-1} \mathbf{T}^T \mathbf{Y} \tag{25}$$

For the practical implementation, the number of latent variables has to be fixed before the final model is obtained. Therefore, the selection was carried out with the *leave-one-out* cross validation method. This means that a separate PLS model is constructed for every single data point so that the data point in question is not included in the model, being left for *prediction error* calculations. If the prediction errors are then summed for each output channel the *cumulative predictive residual error sum of squares* (CUMPRESS) can be obtained.

To implement the particle size estimation, the shadow length distribution $\mathbf{v}_S$ was used as $\mathbf{X}$ and the hand-screened samples as $\mathbf{Y}$. The CUMPRESS values were calculated for the first three latent variables and the results are shown in Fig. 4.8. Based on this, the number of latent variables was fixed to two, as it produced the smallest error.

Once the number of LVs was fixed, the $\mathbf{X}$ side of the analysis was optimized by testing several parameters of the image analysis part. At the same time, the dimension of $\mathbf{X}$ was reduced by grouping shadow lengths into classes. The number of these classes and their border values were obtained by manually selecting a different number of classes and a starting point for the borders, and then iterating around those points in order to get the best fit. The error on the $\mathbf{Y}$ side was weighted by $\mathbf{w}_y = [3,1,1,2]$ where the importance between the classes (from

the smallest to the largest, smallest is on the left) is expressed. This information was obtained from the mine personnel.

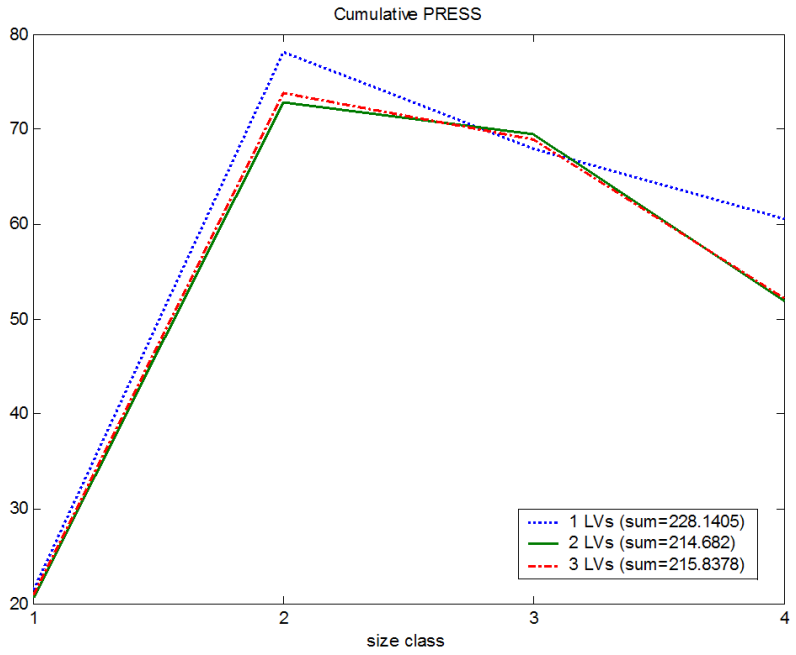

Fig. 4.8 Cumulative predictive residual error sum of squares.

The fitting resulted in the following four shadow length classes: 0-17, 18-31, 32-56 and 57+ pixels. The results for the finest (and most important) class are shown in Fig. 4.9, where it can be seen that a relatively good correlation exists; the *correlation coefficient* R for the fitting being 0.89 (equivalent R^2 value is 0.79, where R^2 is the *coefficient of determination*). The other classes could not be estimated so accurately with the selected method; the correlation for pebbles, middle fraction and lumps were 0.54, 0.53 and 0.61, respectively [60]. Therefore, it was clear that the results achieved for the fine ore were acceptable, but further improvements were needed for the estimation of the other fractions.

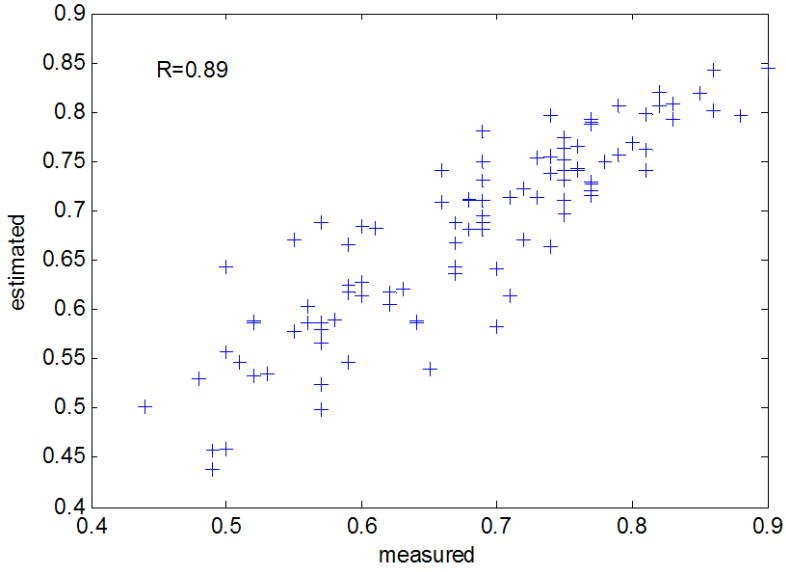

Fig. 4.9 Validation of fines.

4.2.5. Improvements & Neural Network Validation

Even if the shadow based analysis had worked perfectly, it would only have predicted the relative proportions of different size classes present on a conveyor belt. However, as the total mass flow varies, it would not be possible to turn this information into absolute values (e.g. into tons/h) without the total mass flow information. This was part of the motivation for purchase of a belt weigher for the HKU2 belt.

Another issue was that the mass flow information could be incorporated into the calibration model, and thus the results could be expected to be more accurate. Consequently, a belt weigher was purchased by Pyhäsalmi Mine Oy and installed near (11 m before) the analysis point of the previous system. This made it possible to make new models; the only cost, besides the cost of the belt weigher, was that another 150 samples had to be shovelled in order to get the mass data included in the samples. Also, since the previous analysis had shown that the middle fraction caused trouble for the analysis due to its small size range (and since it was combined with pebbles in any case), it was decided that the middle fraction should be combined with pebbles also in the analysis.

A new PLS model was made with 100 data points as the training data, while the remaining 50 points were saved for validation. The results obtained with the improved version are shown in Fig. 4.10; the correlation coefficients are shown in graph titles. As can be observed, the model is much more accurate, especially with fine ore and lumps.

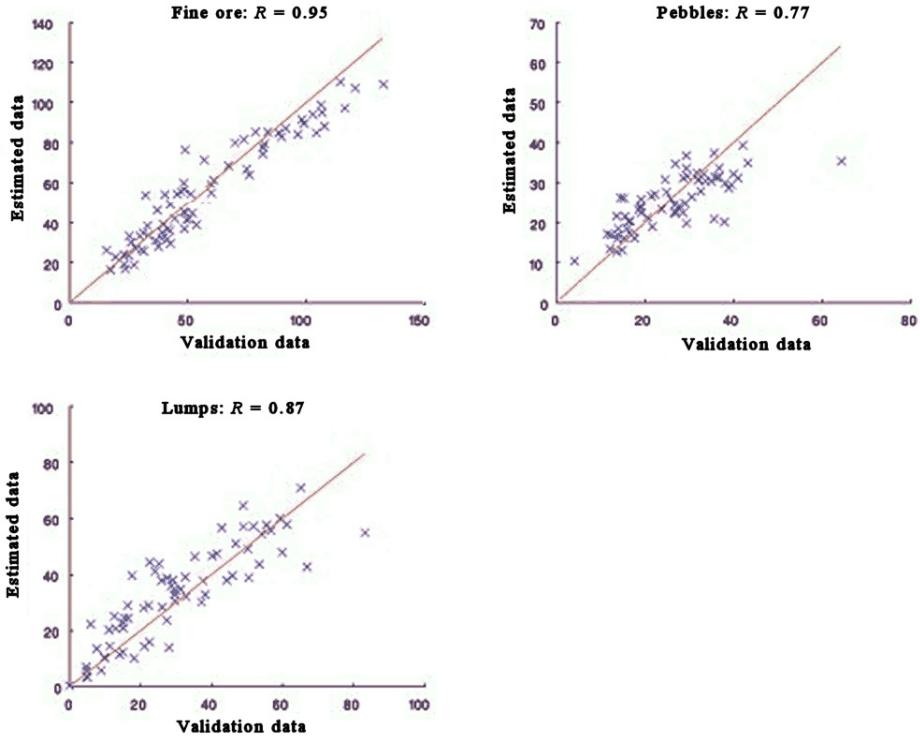

Fig. 4.10 Improved PLS model results.

Finally, a back-propagation neural network [33] was tested in order to see whether or not the modelling method had a significant effect on the results. As shown in Fig. 4.11, the neural network approach gave slightly better but similar results.

Since the non-linear neural network approach did not give significantly better results, it was a natural choice to go with the simpler and robust linear PLS version, especially when the number of data points reserved for training was relatively low.

Further details of the improved PLS model and the neural network validation are given in [61].

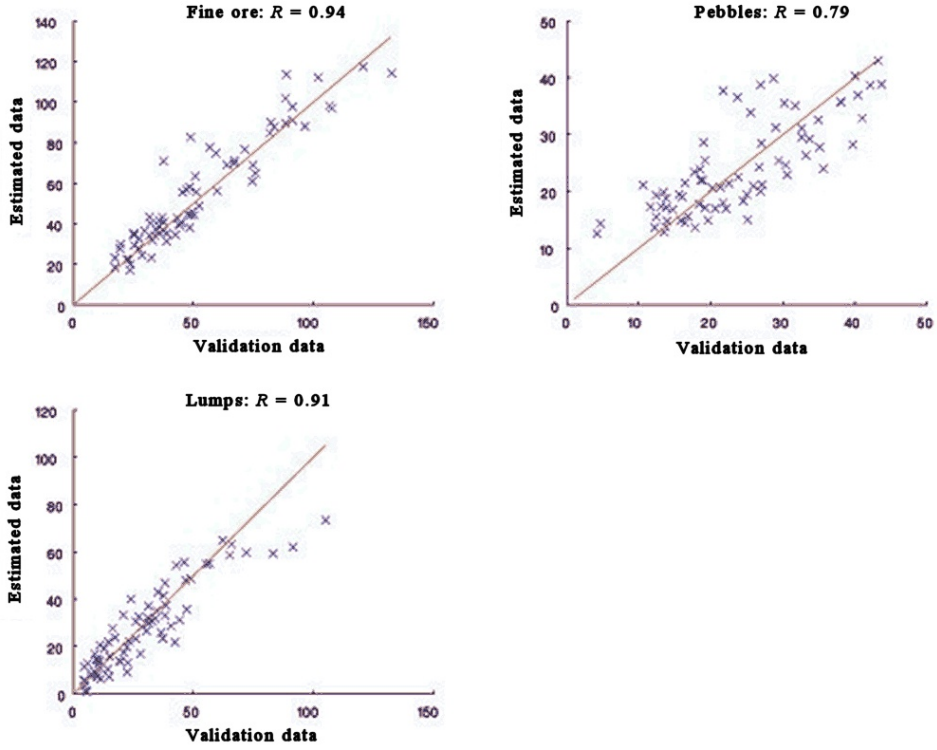

Fig. 4.11 Comparison with a neural network.

4.2.6. Software Components

As mentioned earlier, the algorithms were realized with MATLAB™ and there was a need for dedicated software that would tie the image grabbing, belt weigher communication, analysis and distribution of results together.

At first, there was a separate MATLAB™ installation communicating with another program via an ActiveX® connection mechanism. At a later stage, the architecture shown in Fig. 4.12 was adopted from the results obtained while developing the new *FrothEye*-software for flotation analysis (see Subsection 5.3.2). The idea behind this architecture is to design the software components to be as modular as possible in order to isolate the development of the algorithms. This makes it possible to code the supporting parts of the software separately (hopefully only once) and the iterative work of algorithm development can be isolated into a calculation kernel. Furthermore, the kernel is implemented as a COM (Component Object Model) object [6] that can be generated automatically with the tools of the MATLAB™ environment. This enables *rapid prototyping*, i.e., extremely flexible and powerful development of the analysis routines, since all new ideas can be coded and tested with MATLAB™. After testing, the final version can easily be converted into a COM object and uploaded to the analysing computer.

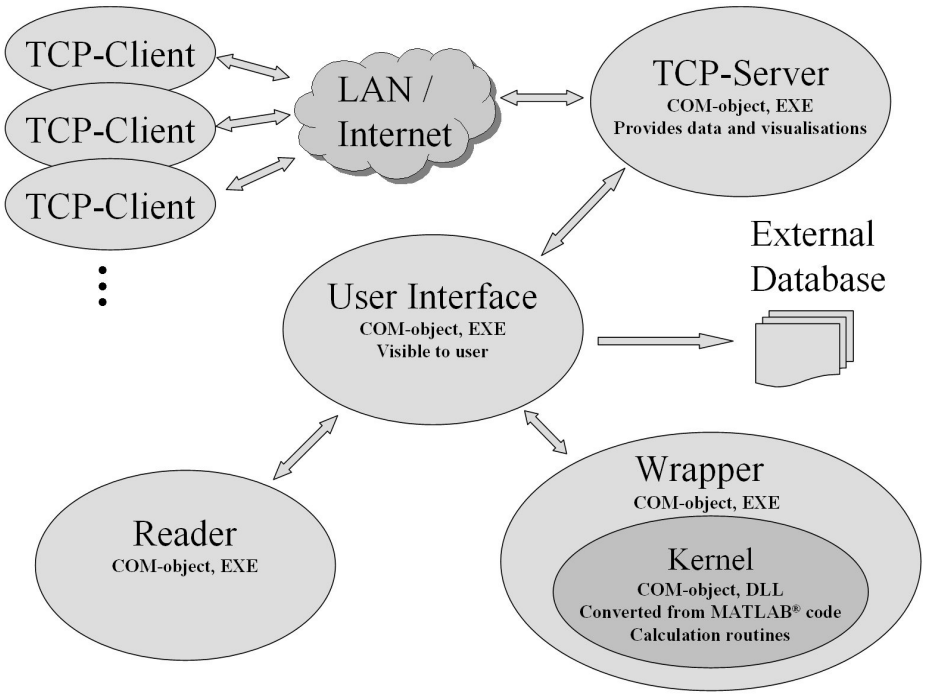

Fig. 4.12 An overview of the software architecture.

The individual components are introduced in the following.

- *User Interface (UI):* Provides run time access to the analysis. Enables the user to modify the laser scanner and belt weigher settings and provides feedback from the analysis kernel. Provides a connection to an external database.
- *Reader:* Provides data for analysis. Returns collected data to the data buffer of the user interface component.
- *Wrapper / Kernel:* All the calculation routines are implemented in the Kernel component, which is automatically generated from MATLAB™ code. Since the MATLAB™ compiler only generates in-process components (i.e. DLL-files) the Kernel is encapsulated into another COM-EXE component (Wrapper) which provides the necessary interface for the UI component.
- *TCP-Server:* Keeps a local database containing the numerical results as well as images. The server is designed to be connected with TCP-Client(s) (see Fig. 4.13). The client(s) can connect through a local area network (personnel working at the plant) or via Internet (remote monitoring).

A dedicated protocol was developed by the author to serve the communication between the TCP-Server component and the TCP-Client program(s). The protocol

enables a reliable transfer of compressed image and control data through a single TCP/IP socket (socket is an end-point in the IP networking protocol). The client software shown in Fig. 4.13 was designed to be the main tool in utilizing the results of the particle size analysis on site and remotely by the researchers. It displays the calculation results for the particle size analysis, as well as silo levels after the screening station. The user can view history trends of desired length and see visual appearance of the conveyor belt. The database contains one minute data for the last 30 days. There is also a password protected mechanism for the power users to set the target levels for different particle size classes.

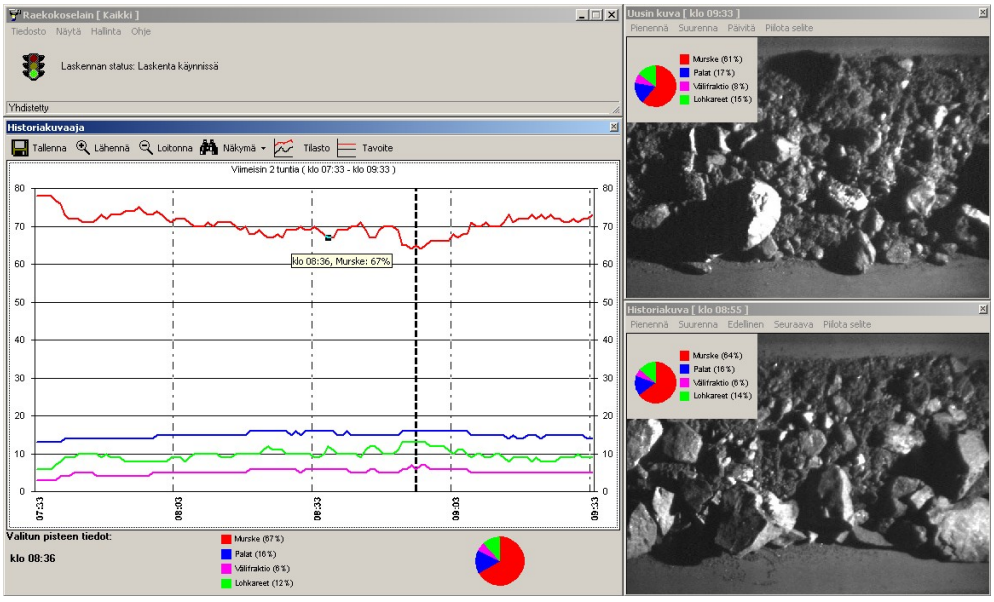

Fig. 4.13 TCP-Client Software. The pie-charts display different particle size proportions for fines (red), pebbles (blue), middle fraction (violet) and lumps (green).

4.2.7. Reasons for the Shift to 3D Analysis

Although the improved PLS model gave satisfactory results, there were problems with the life span of the halogen lamps used in the analysis. Different lamp types were tested, but they lasted typically only 4-5 weeks of continuous operation. Since the analysis point was 1410 meters below ground level in a relatively isolated place, this was not acceptable.

After searching for a durable high power halogen lamp without success, a decision was made to switch to long lasting metal halide lamps, which last over a year of continuous operation. The drawback was that the metal halide lamps cannot be run with DC (Direct Current) and an electronic circuit capable of detecting the phase of the AC (Alternating Current) sine wave had to be designed to compensate for that. Furthermore, for external triggering to work with the selected camera, an external trigger signal with a desired shutter time, as well as horizontal (HD) and vertical

(VD) drive signals needed to be generated for the camera (see Fig. 4.14). All this was accomplished with a phase detection circuitry that was combined with a programmable microcontroller, achieving stable image intensity despite the AC based illumination.

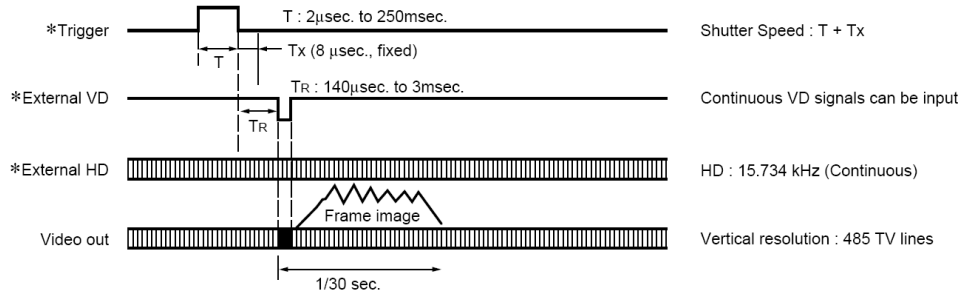

Fig. 4.14 External triggering. [101]

However, even if this problem was solved, the intensity pattern of the new metal halide lamp was not very even. This caused thresholding problems that needed to be solved with a local thresholding approach introduced by Larinkari [60]. Furthermore, since the shadow based approach required illumination from a shallow angle, it meant that the illuminating lamp had to be quite near the belt.

Although there is a magnetic separator preceding the analysis point, which is supposed to remove any unwanted metallic objects such as wire cable stubs that are used in rock bolting, it was often the case that such cables hit the lamp window and tilted the illuminating lamp. Again, this probably could have been solved, but once it was noticed that the German manufacturing company *Sick AG* was bringing a reasonably priced 3D imaging scanner to the market, and since they offered to test their upcoming product in advance, a decision was made to investigate this possibility.

The scanner approach seemed to have many benefits; the 3D scanner would measure real life physical dimensions directly and, more importantly, it would provide accurate information on the height of the ore bed that is very difficult to estimate from a traditional greyscale image, although there are few examples in the literature where it has been done (see e.g. [59] and [78]). Furthermore, the scanner is housed in a protective chamber and can operate for long periods of time without maintenance.

This was known in advance since the mine used another (similar type, same brand) scanner to measure the approaching edge of the ore bed on a weighing belt feeder that is used to measure 21 ton batches of ore for the hoist. Thus, it seemed that the 3D scanner technology would provide better data with the same, or even better, level of robustness when compared to the shadow based technique.

4.3. 3D Height Measurement Based Analysis

The improved particle size distribution analysis is currently carried out with an imaging laser scanner (Sick LMS-400, see [96]) that is located on the same cross-directional axis as the belt weigher (Milltronics Accumass BW100, see [97]), as indicated in Fig. 4.15. The belt weigher comes with a speed sensor so that the device is able to calculate (and output) the mass flow information in tons per hour. An additional speed sensor was also installed to obtain speed information for the segmentation analysis. This was needed to get the dimensional information in the direction of the belt; the other two directions were covered by the scanner. These two are routed as standard 4-20 mA signals to an external A/D-board of the analysing computer. The laser scanner is connected with a single cross-cable to an additional *network interface card* (NIC) of the computer, which in turn is connected to the mill's network. Reliable operation is further ensured with an *uninterruptible power supply* (UPS) and external watch-dog circuitry monitoring the system. Monitoring is carried out via the serial port of the analysing computer; if the *data terminal ready* (DTR) signal is not updated (with a dedicated piece of software) for a pre-determined period of time, the circuitry will force a boot-up procedure for the computer.

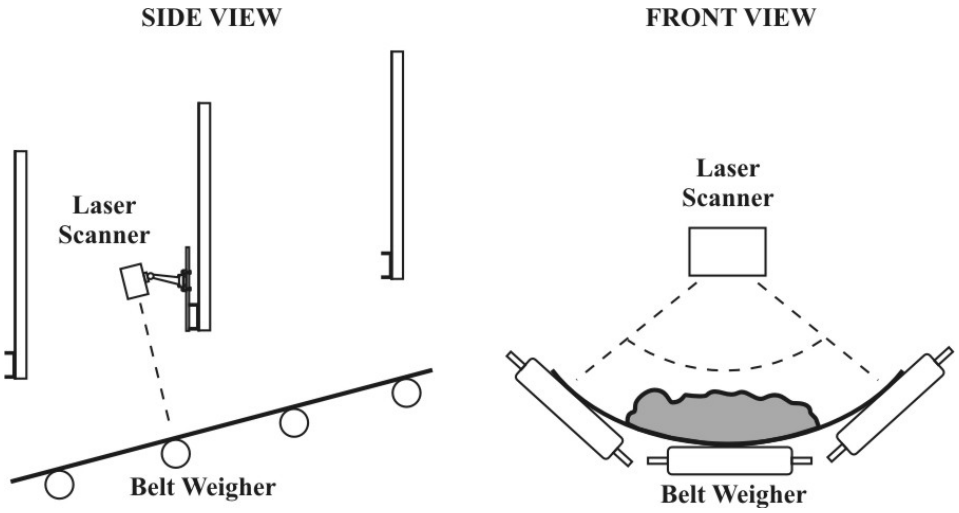

Fig. 4.15 Laser scanner based measurement setup.

4.3.1. The New Data

The LMS-400 is based on a single laser point (wavelength $\lambda = 650\,\text{nm}$) with an output power of 7.5 mW. The laser point is diverted by a rotating polygon-shaped mirror to cover a maximum angle of 70°. The distance measurement can be done in the range of 70 cm – 3 m, and is based on measurement of the phase shift caused by the propagation time differences of the laser light [96]. The standard deviation of the distance measurement depends on the physical distance and on the measured

material. For this application, the standard deviation of the distance measurement was approximately 6 mm, which was acceptable, although slightly better results could be expected with a more accurate instrument. Such equipment does exist, but comes at a considerably higher price.

The scanning rate is set to 360 Hz, meaning that the device produces 360 cross-sectional lines $\mathbf{v}_c$ per second, each line consisting of 240 points. Since the belt speed is 1 m/s, this means that successive cross-sections are 3 mm apart. However, the $\mathbf{v}_c$ vectors are measured by linearly increasing the measurement angle, which leads to non-uniform spacing between the samples. This distortion is rectified by a simple geometry correction combined with the nearest neighbour interpolation, yielding to a uniformly distributed grid with 3x3 mm spacing.

The moving ore bed is imaged in 3 m batches and topographic images are produced for the segmentation stage.

4.3.2. Segmentation

The segmentation method is based on the well-known *watershed* segmentation routine (see e.g. [111]). It starts from local minima in a 3D landscape and "fills up" the areas, commonly called *catching basins*, until common borders are reached. It is typically used for greyscale images and has been applied also for rock segmentation, as shown by Farfán *et al.* [18], but it can just as well be used for a true 3D landscape, as is the case here. A common modification of the algorithm is called the *marker controlled watershed algorithm*, where the starting points can be freely defined.

The segmentation routine in this application uses both of these versions for differently pre-processed data and then combines the results. The idea is to have the first routine separate the particle clusters from the background and the other to separate the individual particles. By dividing these two tasks into separate threads, the need for compromises in algorithm design is avoided. The overall segmentation process is outlined in Fig. 4.16, and explained in the following.

In order to reduce measurement noise, the segmentation process is started with an analogous median filtering procedure as explained in Subsection 4.2.2. The missing measurements are replaced with the mean of the neighbouring measurements.

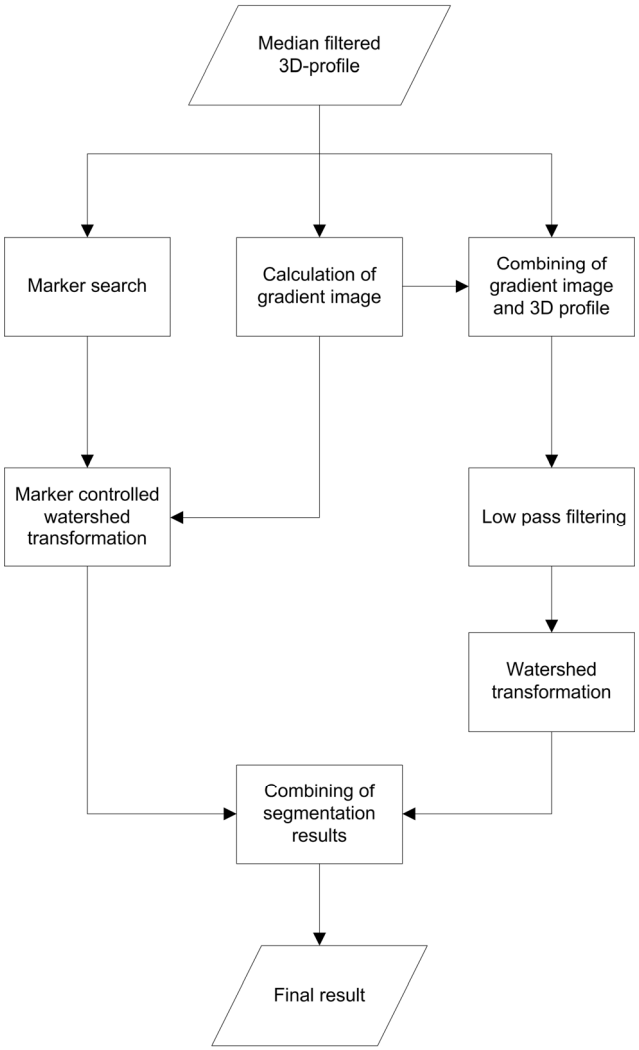

Fig. 4.16 The segmentation algorithm.

The left branch in Fig. 4.16 shows the segmentation routine that separates the particle clusters from the background. It is based on a marker controlled watershed algorithm that uses a *gradient image* f calculated from the 3D profile by using a standard 3x3 *Prewitt operator* [100], where the gradient images f_x are estimated by *convolving* eight different directional kernels $\{h_1, h_2, \ldots, h_8\}$ with the original image *g*:

$$f_x(i,j) = g * h_x = \sum_{m=1}^{3}\left(\sum_{n=1}^{3} g(i-m, j-n)\, h_x(m,n)\right), \quad \begin{cases} i \in \{1,\ldots,N_R\} \\ j \in \{1,\ldots,N_C\} \\ m,n \in \{1,2,3\} \end{cases} \tag{26}$$

where N_R and N_C are the number of rows and columns in the image, respectively, and by selecting the convolution result of the greatest magnitude as the direction of the gradient. The first three directional kernels are given as an example:

$$h_1 = \begin{bmatrix} 1 & 1 & 1 \\ 0 & 0 & 0 \\ -1 & -1 & -1 \end{bmatrix} \quad h_2 = \begin{bmatrix} 0 & 1 & 1 \\ -1 & 0 & 1 \\ -1 & -1 & 0 \end{bmatrix} \quad h_3 = \begin{bmatrix} -1 & 0 & 1 \\ -1 & 0 & 1 \\ -1 & 0 & 1 \end{bmatrix} \tag{27}$$

The rest can be obtained by simple rotation.

The markers for the particles are calculated by similarly convolving a *Gaussian filter* $G(i,j)$, given by

$$G(i,j) = e^{-\frac{i^2+j^2}{2\sigma^2}} \tag{28}$$

where *i* and *j* are the image co-ordinates of the kernel and σ is the standard deviation. This leads to a smoothed image from which the second derivative is calculated with the *Laplace operator* Δ, defined by

$$\Delta f(i,j) = \frac{\partial^2 f(i,j)}{\partial i^2} + \frac{\partial^2 f(i,j)}{\partial j^2} \tag{29}$$

And finally, the *Laplacian of Gaussian* (LoG) is calculated as follows

$$\mathrm{LoG} = \Delta\left[G(i,j,\sigma) * g(i,j) \right] \tag{30}$$

From this, large continuous areas with negative values are searched. These correspond to convex shapes in the rock mass.

The markers for the background are set to mark the flat areas in the 3D profile. These are extracted by *top hat transformation*, which is a simple tool for extracting objects from an uneven or slowly changing background [100].

The right branch in Fig. 4.16 shows the segmentation routine for individual particle segmentation, where the 3D profile *g* and the gradient image *f* are scaled to the interval [0,1] and summed together. The resulting image is then low pass filtered with a 12x12 *mean filter* (by using a similar procedure as with the median filter, only now the mean value is calculated) and finally, the areas corresponding to shallow minima in the image are removed by using *H-minima transformation*, described in [99].

The final segmentation result is obtained by combining the resulting images from the two branches. This is done by simply discarding the erroneous particle borders that are formed in the particle detection phase and located outside the cluster borders defined by the clustering branch.

An example of the segmentation results is shown in Fig. 4.17, where four different images are shown; the original median filtered image *g*, the resulting image of the left branch, the resulting image of the right branch and the final segmentation result (from the left, respectively).

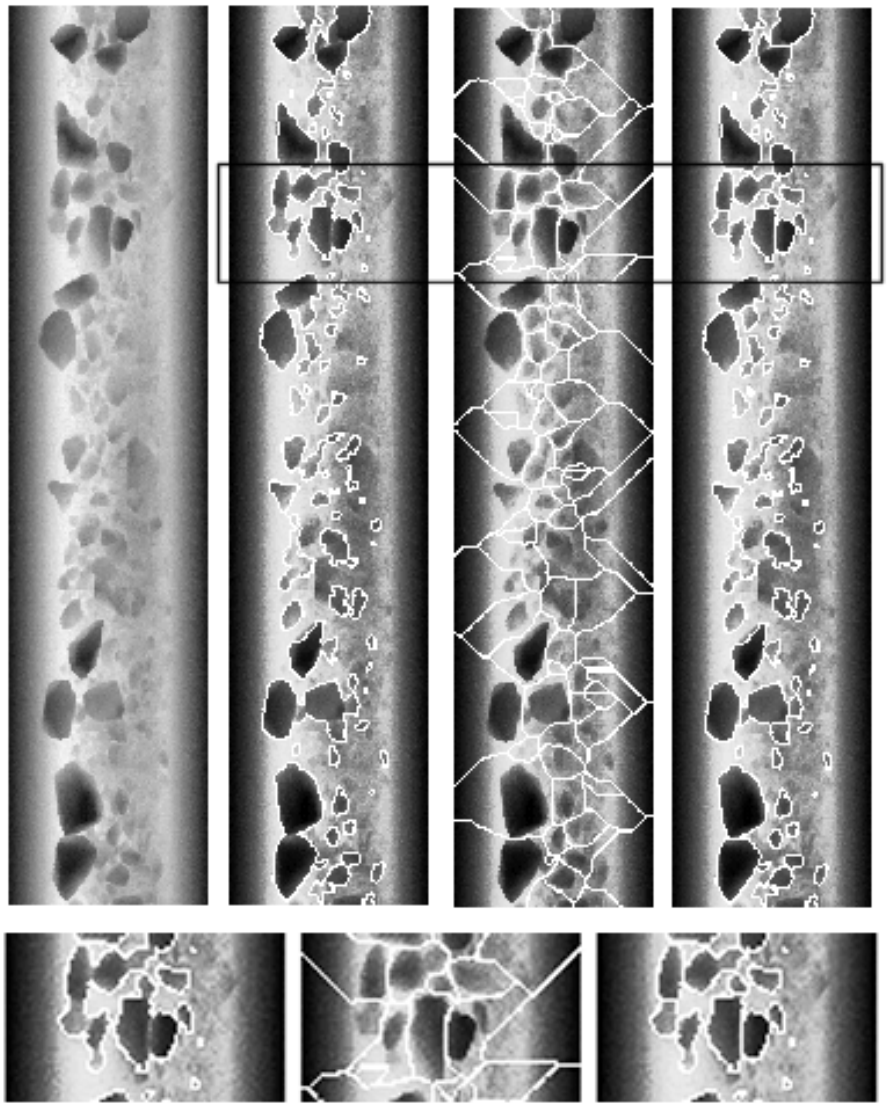

Fig. 4.17 Segmentation results, images from the left: original median filtered 3D profile, segmentation into particle clusters, segmentation of individual particles and final segmentation result. The emphasized rectangular area is shown at the bottom to provide more detailed view.

The detailed view in Fig. 4.17 shows an example of the advantage of having these two branches; the clustering part recognizes the large areas and the particle part

separates individual rocks inside those areas. Furthermore, the idea behind the segmentation is to recognize only the large particles, since the volume of the fines can be estimated by subtracting the volume of the recognized particles from the total volume of the ore. This justifies the use of the LMS-400 scanner, even if its measurement accuracy is not the best possible.

4.3.3. Virtual Sieving and Volume Estimation

The large particles recognized in the segmentation process go through a *virtual sieving* procedure, i.e. their size classes are determined by the shortest edge of their bounding box. This simulates the process of real life sieving. The height information is not used in this process; the largest particles are assumed to have fallen in a way that the height would be smaller than the other two dimensions, which is a fair assumption when considering the rocks on a conveyor belt. The height is not included because it is difficult to measure it for an individual particle when only the surface can be seen. The particles are most often sunken to the bed of fine ore, as illustrated in Fig. 4.18, and the shape of the sunken part is unknown.

This is why, at each point, the height of a given particle is calculated by subtracting the height of the estimated ore bed from the total height. This approach will disregard the sunken part and will introduce a small error to the volume estimation. On the other hand, the imprecise estimation of the unknown part would do so in any case. This error is, however, taken into account by introducing non-linearity to the calibration model, as described in the following section.

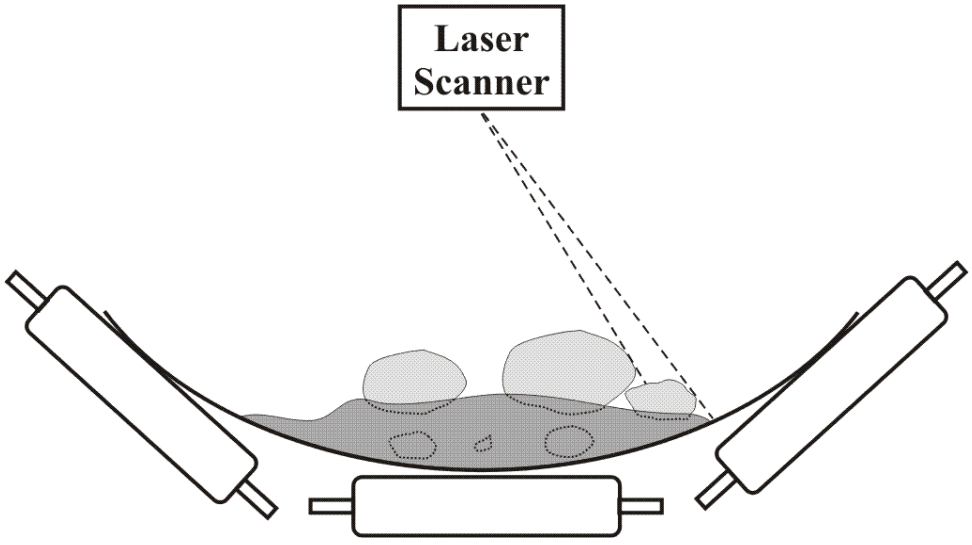

Fig. 4.18 Illustration of the areas not visible to the scanner.

4.3.4. Calibration Models

There are also other sources of error and non-linearities in measuring the particle size distribution from the surface of the ore bed. Firstly, it is possible that segregation has happened due to vibration and multiple conveyors, which often are at a 90° angle. Secondly, the larger particles have a higher probability of being visible on the surface, as can easily be seen when examining the illustrated particles in Fig. 4.18. This phenomenon is studied in detail and a model for the stack structure is given by Thurley in [105]. Thirdly, the measurement technique used prevents the scanner eye from seeing all the parts of the otherwise visible area, which is also illustrated in Fig. 4.18.

A neural network model would be a good choice for this type of modelling problem, since it is naturally capable of dealing with non-linearities. However, neural networks typically need quite a lot of training data, and since additional shovelling was required – again, this was not an option. Instead, these non-linearities were compensated for by generating additional non-linear input variables to the $\mathbf{X}$ data of a linear PLS model (see Subsection 4.2.4). This leads to the following $\mathbf{X}$ data block:

$$\begin{cases} \mathbf{x}_1 = \text{volume of ore not recognized as an particle} \\ \mathbf{x}_2 = \text{volume of ore classified to size class } 50\text{-}75\ mm \\ \mathbf{x}_3 = \text{volume of ore classified to size class } 75\text{-}100\ mm \\ \mathbf{x}_4 = \text{volume of ore classified to size class } 100\text{-}135\ mm \\ \mathbf{x}_5 = \text{volume of ore classified to size class } > 135\ mm \\ \mathbf{x}_6 = \left(\text{volume of ore classified to size class } 0\text{-}50\ mm\right)\mathbf{x}_1 \\ \mathbf{x}_7 = \mathbf{x}_2\mathbf{x}_1 \\ \mathbf{x}_8 = \mathbf{x}_3\mathbf{x}_1 \\ \mathbf{x}_9 = \mathbf{x}_4\mathbf{x}_1 \end{cases} \tag{31}$$

From this, the particle sizes are estimated with three different models. The amount of fines is estimated by doing a standard least squares fit for $\mathbf{x}_1$. The amount of pebbles is estimated from $\mathbf{x}_{\{6-9\}}$ with one PLS model and the amount of lumps from $\mathbf{x}_{\{2-5,7-9\}}$ with another PLS model.

4.3.5. Results & Considerations

The three models mentioned above were obtained by manually collecting 32 data samples, each 1.5 m long. These were weighed and screened into the same particle size classes as before and the middle fraction was combined with pebbles. Along with these samples, the scanner data, speed sensor data and mass flow data were recorded. The average sample size was 143 kg.

The modelling results can be seen in Fig. 4.19 and they indicate that the selected method outperforms the previous shadow based analysis method. A similar leave-one-out cross-validation method was used as in Subsection 4.2.4.

The current versions of the models do not take the mass flow information as their input; the final size class flows are calculated after class estimation. If this information would be included already in the training phase, even better results could be obtained.

Another revelation was encountered when trying to take advantage of the particle size distribution measurement; as mentioned earlier, the final goal was to be able to predict the future situation in the silos of the flotation plant. However, it was noted that the particle size distribution changes (more than expected) on the way up, due to abrasion in the ore transportation chain [61]. Therefore, in order to be able to predict the silo level at the surface, a model describing the ore transportation chain would be needed.

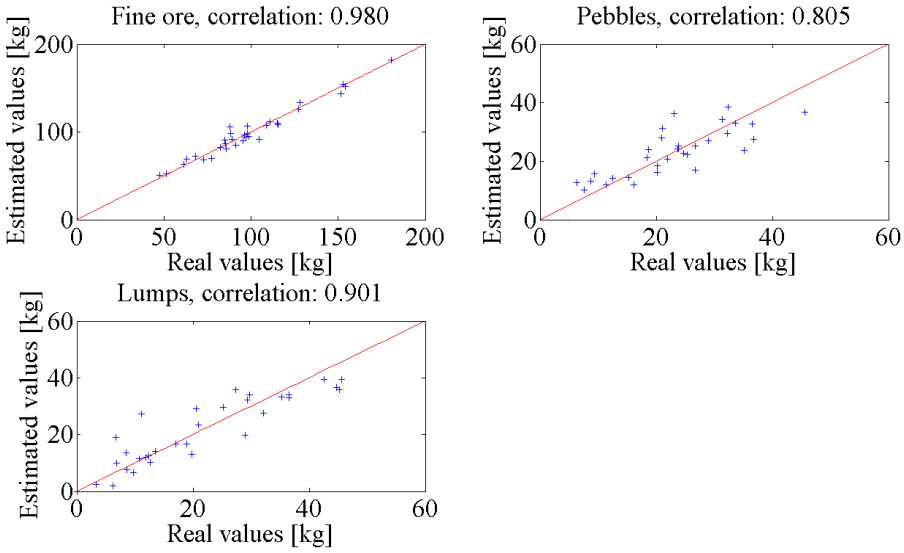

Fig. 4.19 Analysis results of 32 hand screened samples.

To get this model, the analysis station was duplicated and installed on a conveyor belt just before the mechanical screening station on the surface. The installation points of both analysis stations are indicated in Fig. 3.4. The required transportation chain model is fairly simple and it was thought to be obtained quite easily but, as it turned out, there are no reliable instruments that are capable of measuring the necessary silo levels and material flow rates accurately – not within a feasible price range at least. The uncertainties in these measurements have caused problems for modelling, but work is still being done to address this issue.

5. Flotation Froth Analysis

This chapter describes the research related to flotation froth analysis in Pyhäsalmi and is based on the publications [P1], [P3], [P4] and [P5]. First, the original single cell analyzer that was built for the zinc rougher circuit is introduced. Then, its extension to a multi-camera analysis system, covering several flotation cells, is discussed and finally the results achieved are presented.

The work carried out in image analysis of the flotation froths, especially the dependency found between the colour and the grade, motivated the continuation of the research with another approach, based on spectral measurements and described in Chapter 6.

5.1. Motivation

It is a well known fact that the visual appearance of the flotation froth is a good indicator of the state of the process. This information has been utilized in the past decades by the process operators simply by walking periodically down to the flotation cells and making conclusions based on the froth appearance. Naturally, these conclusions are subjective and depend on several things, such as the operator's experience and motivational level, as well as colour temperature and intensity changes of the illumination. Nevertheless, an experienced operator is able to determine many things based on bubble size, colour, speed and other froth characteristics. Two images taken from the zinc rougher circuit at different times, illustrating the noticeable differences that occur during normal operation of the plant, are shown as an example in Fig. 5.1.

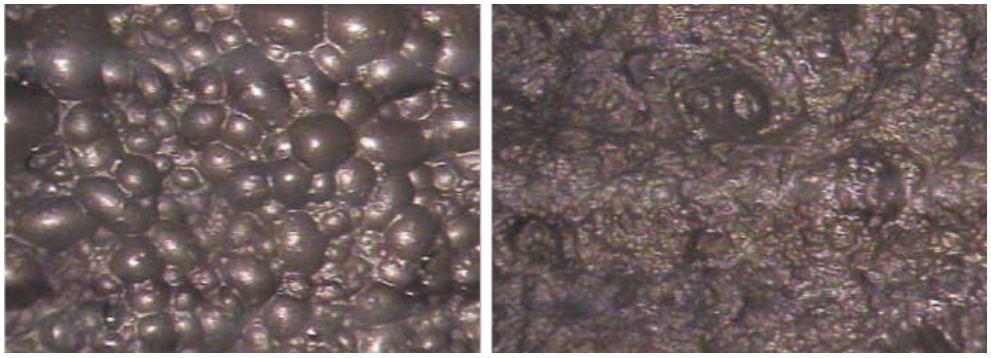

Fig. 5.1 An example showing two images of zinc froth with different image characteristics.

As the rapid development in camera and computer technology has allowed machine vision techniques to cover an increasing range of applications, the possibility to use image analysis in the control of mineral flotation created a lot of interest in the mineral engineering community in the 90's (e.g. [8], [24] and [74]). While most such developments took place in the laboratory, some instrument systems were tested on line in flotation plants (e.g. [24], [73]) and were reported to be applicable to the classification of froths or to the extraction of physical features, such as average bubble size, size distribution and shape parameters of the bubbles, speed of the froth as well as colour parameters.

Motivated by these findings, a European Union funded research project called *"Characterization of Flotation Froth Structure and Colour by Machine Vision (ChaCo)"* was launched in 1997, which initiated the development of a flotation froth analyzer for the Pyhäsalmi mine. The development of the image analysis system, its expansion into multi-camera system and the achieved results are described below.

5.2. Single Cell Analysis

In the following, a brief introduction to the original image analysis station that was built for the concentrator plant of Pyhäsalmi Mine Oy is given and the calculated image variables are introduced. A thorough and detailed description can be found in [40] and [48].

5.2.1. Froth Analyser

It was decided to install the image analysis station on top of the first rougher cell in the zinc circuit (see Fig. 3.15 and Fig. 5.2), because the rougher bank was known to have the greatest effect on the overall performance of the zinc circuit.

Fig. 5.2 Froth analyzer installed on the rougher bank of the zinc circuit.

The installation point had to be near the edge of the cell in order to have a constant flow under the imaging area. The architecture of the developed analysis station is shown in Fig. 5.3, in which the camera is located inside a protective hood and illumination is carried out with an adjustable halogen lamp. The analysis station included also a *spectrophotometer* that was used to investigate the colour properties of the froth with a more accurate instrument than a regular RGB colour camera, which was used for the image analysis part. Unfortunately, the physical arrangement for the spectral measurements was not suitable for continuous operation and these measurements were eventually dropped from the next version of the analysis station. However, the initial spectral analysis done at the time (see [48] and [98]) partly motivated the re-introduction of spectral measurements as a descriptor of grade, which will be discussed in Chapter 6.

The purpose of the protective hood was to act as a supporting structure, as well as a protective element against ambient light coming from the flotation hall. Great care was taken to remove any disturbing light and for ensuring stable illumination from the lamp. This was especially important when analysing image variables simultaneously from several cameras (this topic is covered later in this thesis), because it was noticed – after a relatively intensive investigation – that the voltage changes in the electrical network of the mill caused simultaneous fluctuations to the image variables, ruining the correlation analysis. Consequently, a powerful *uninterruptible power supply* (UPS) was installed to provide regulated power for the analysis equipment. This solved the problem and the cross-correlation analysis started to give meaningful delay estimates.

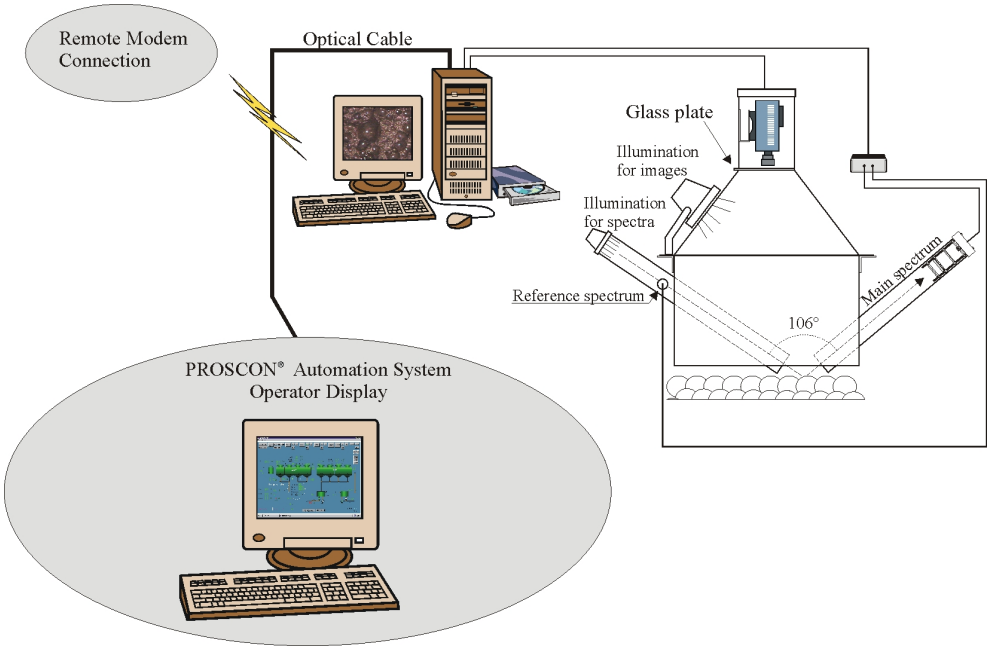

Fig. 5.3 System architecture for the single cell analysis.

In the analyzer, the imaging geometry is arranged so that a single bright spot, called the *total reflectance point*, is formed on top of each bubble. This is an important property since many of the image analysis algorithms utilize segmentation results, which are obtained with a similar watershed algorithm as described in Subsection 4.3.2. The algorithm uses these bright spots as starting points for bubble border detection (since they correspond to local minima in inverted image). An example of the segmentation results obtained this way is illustrated in Fig. 5.4. Further details of the algorithm are given in [5].

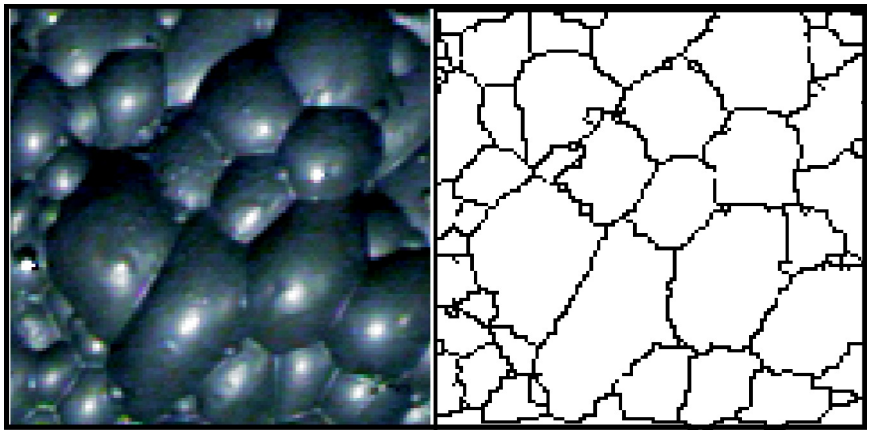

Fig. 5.4 An example of the segmentation results.

5.2.2. Calculated Variables

The philosophy with the original image analyzer was: "Calculate everything that can be calculated and then pick the most interesting variables for analysis". Consequently, it was possible to get approximately 60-70 different variables from a single cell. However, there was redundancy in these measurements. A good example is the different colour plane representations of the image; the grabbed image was presented both in RGB (red, green, blue) and HSV (hue, saturation, value) colour planes, and for all these six variables, the first four moments of their distribution were calculated separately. Thus, there was a need to pick out only the most important variables for further analysis. This was done by step change tests, by correlating the image variables against other process variables and by conducting an operator inquiry (see [31] and [40] for details). The purpose of the inquiry was to leverage the process knowledge of the operators in finding the froth characteristics that reflect the flotation performance. The following five variables were selected as the most important image variables:

1. *Froth colour:* During the operator inquiry, the operators pointed out that the colour of the froth correlates with the mineral concentration of the froth. Therefore, the mean and standard deviation for the R, G, and B values are calculated over the image plane. In order to avoid the effect of total reflectance points and shadows, both extremely dark and bright intensity values are excluded from the calculation.

2. *Bubble size distribution:* In the operator inquiry, the operators pointed out that bubble size can be used to find the optimal amount of frothing reagent. In some cases the bubble size is also correlated with the *mineral load* of the froth. The bubble size is calculated by using the watershed segmentation algorithm mentioned earlier.

3. *Froth Speed:* The froth speed reflects the production rate and therefore is an important variable. The speed is calculated from an image pair, where the sampling interval between the two images is 20 milliseconds. The algorithm calculates the 2D correlation matrix of the image pair, and the highest peak of the correlation matrix determines the amount of pixels the froth has moved during the sampling time (see Fig. 5.5). The actual implementation of the algorithm is done in the *Discrete Fourier Transform* (DFT) domain in order to minimise computational burden. For a more detailed description, see [40].

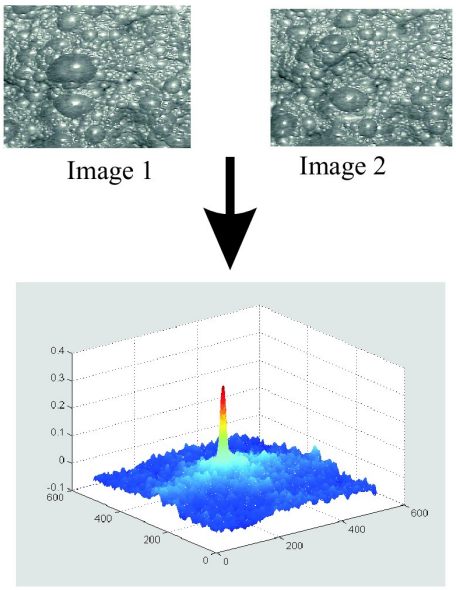

Cross-correlation matrix

Fig. 5.5 Froth speed calculation.

4. *Bubble Collapse Rate:* According to the operators, bubble collapse rate behaves in a similar manner as the bubble size. The bubble collapse rate is calculated as follows: by using the speed information, the latter image in the image pair is translated back to the same position as the first one. After that, the difference image between the first image and the translated image is calculated. Now, the number of pixels above a given threshold gives an estimate of the bubble collapse rate.

5. *Bubble Load:* A visual inspection of the froth images has revealed that bubbles with high mineral load do not have a total reflectance point. Consequently, this algorithm calculates the combined area of bubbles that do not have total reflectance points, i.e. saturated pixel values (under proper lighting conditions), in percentages of the whole image area as:

    1) Go through each pixel of the froth image. If the value of the pixel is equal to (255,255,255) then mark this pixel as a wet pixel.

    2) By using the labelled image from the segmentation algorithm, check which bubbles have pixels marked as wet pixels in the previous step. Mark these bubbles as wet bubbles.

    3) Calculate the total number of pixels that are classified as belonging to wet bubbles. Divide this number with the total number of pixels in the image and multiply it by 100%. This number (which takes values between 0% and 100%) is the outcome of the algorithm, which is called the *load variable*.

5.3. Extension to Multi-Camera-Analysis

The original single cell analysis system was built to provide a *proof of concept*, and after very encouraging results (as will be reported in Section 5.4), a natural step was to extend the system to cover several flotation cells. Five additional cameras were installed in the roughing-, scavenging-, mid-roughing-, mid-scavenging- and to cleaning-sections of the zinc circuit [49]. The camera locations as well as analysis points for the X-Ray Fluorescence (XRF) analyzer are indicated in Fig. 5.6. The XRF method is commonly used in industrial flotation plants for elemental analysis of flotation slurries. The analyzer used in Pyhäsalmi is Outotec Courier® 6 SL [82] (more detailed description of the analyzer is given in Chapter 6) and it was used in the image analysis research mainly for providing grade measurements for validation purposes.

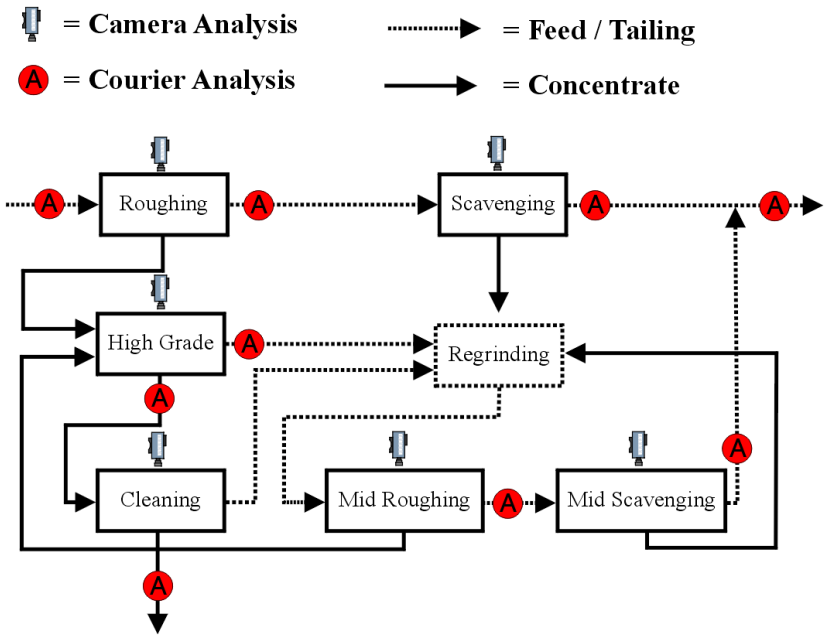

Fig. 5.6 Camera locations and analysis points in the zinc circuit.

Shortly after the installation of these five cameras, a sixth camera was installed to measure the final copper product in the copper circuit. The installation point is indicated in Fig. 3.14.

5.3.1. Froth Image Analyser-software

After the decision for the extension to cover multiple cameras was made, it was clear that the analysis software for the initial prototype would have to be either re-coded or replaced altogether. The original software was a combination of LabVIEW™, MATLAB™ and other calculation routines such as DLL files coded in FORTRAN or in C/C++ programming languages [48].

Since one of the people closely related to the ChaCo project founded a company called IMSOC and implemented the algorithms for a commercial multi-camera capable package, a decision was made to use this software package as a basis for further research. The software was called *Froth Image Analyser* (FIA) and it contained essentially the same functionality as the original analysis system did, with the exception that the FIA software was capable of analysing images from up to 12 cameras sequentially. The FIA software was implemented with LabVIEW™ and compiled into a self executable component that could be installed on a stand-alone computer. An example of the user interface of the FIA software is shown in Fig. 5.7 below.

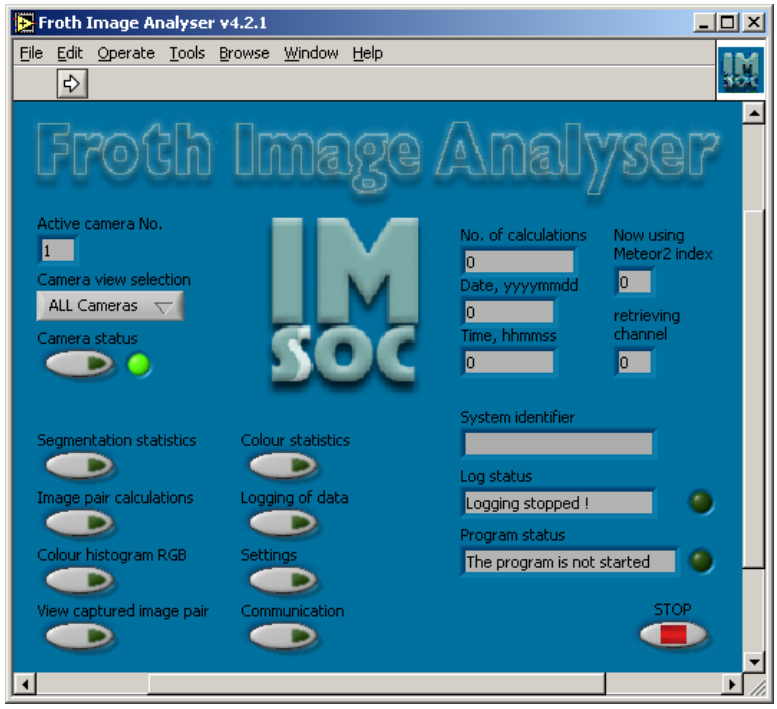

Fig. 5.7 User interface of the FIA software. [44]

However, some obstacles were encountered with this type of approach. While the FIA software in itself was working almost perfectly, the problem was with the original assumption that the ground work laid in the earlier phases of the research would be mature enough to be used as a fixed basis for higher level analysis. This assumption was motivated by a rather idealistic view, claiming that the image analysis part was ready, and the new research should concentrate on utilizing the image variables at a higher level. Unfortunately, this was not the case and, in retrospect, it is only natural that in this type of research new ideas emerge and often the algorithms need adjusting or even completely new algorithms need to be introduced. Since the FIA software was now a commercial and rather closed product (although the research team had a good understanding of the inner

workings of it), it meant that the changes and modifications had to be requested from Sweden and the time schedule for the implementation was now dependent also on IMSOC.

The hardest part was the introduction of the new laser based froth height measurement (introduced later in Subsection 5.3.3), which required several iteration rounds and still the results were not satisfactory. Therefore, this part of the analysis was tested separately with an off-line implementation, based on MATLAB™ and its Image Analysis Toolbox. The implementation was then compared against the FIA software and it showed much better results. During this process, an idea for a new versatile image analysis system for multi-camera analysis was conceived, which resulted in a new image analysis platform called *FrothEye* that is presented in the next subsection.

5.3.2. FrothEye-software

FrothEye was developed mainly by the author to serve as a powerful image analysis tool for doing on-line analysis of flotation froths. However, the software architecture is general enough for its use to be expanded into other image processing tasks also. In fact, the architecture of the system is one of the key points that make it versatile and extremely powerful for the type of research that was carried out in this thesis. An example showing the FrothEye software running in Pyhäsalmi is shown in Fig. 5.8.

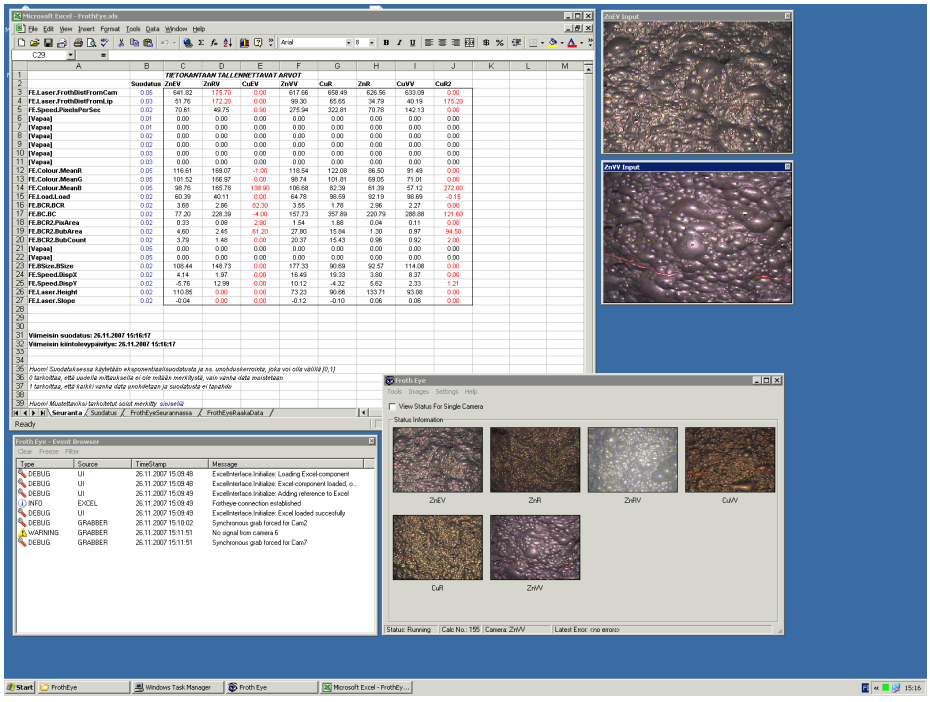

Fig. 5.8 An example of the FrothEye user interface during normal operation.

The basic philosophy in FrothEye's design has been the ease of use and especially the ease of development/debugging. Thus, it is not an overstatement to say that new algorithms and ideas can be tested in a matter of hours. This would not be possible if the program was coded by using traditional methods. The flexibility of the programming environment is achieved by using modular design and code generation. The core of the program where all the calculations are performed (a.k.a. kernel) is created from MATLAB™ code (i.e. from M-files generated with MATLAB's scripting language) with a single push of a button. Once the kernel is created, it can be moved to the plant and run without any modifications to the pre-compiled FrothEye-software. This helps tremendously in the development work since only the kernel code needs to be modified and re-compiled. Furthermore, debugging can be done in the MATLAB™ environment by using a custom made debugger that simulates normal operation and runs the un-compiled kernel code in exactly the same way as the user interface in the plant will. In this way errors can be isolated and removed already in the design phase and the debugger will indicate the exact position (as well as values for local variables) where the error occurred.

The general layout of the software architecture is shown in Fig. 5.9. There are three main components that are started when the application is run. These are: *User Interface (UI)*, *Grabber component* and *Wrapper component*. All these components are coded with Microsoft Visual Basic® and they are ActiveX®-components, i.e. they comply with the component object model (COM), see [6] for details on COM.

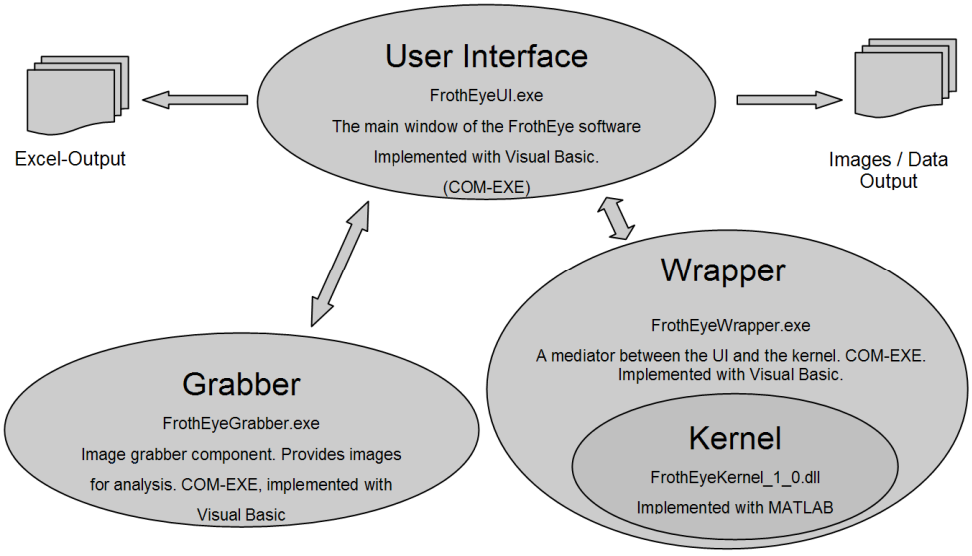

Fig. 5.9 Software architecture of the FrothEye platform.

The idea behind this type of arrangement is modularity as well as improved performance. Modularity is achieved by dividing different tasks into separate components that can be maintained independently. Improved performance is

achieved by compiling each component as a COM-EXE, meaning that each will have its own thread of execution. The user interface loads and unloads all the components automatically during start-up / shutdown and is the only visible part of the software (if the Excel output is not enabled). Another important point is that all components, except for the kernel, are designed to be coded once – and only once. This applies even if new algorithms are added or inputs and/or outputs of existing algorithms are modified. The only component that needs to be recompiled is the kernel (i.e. a single DLL file). And since the kernel component is maintained and developed completely with MATLAB™, this means that algorithm development of the FrothEye software is made extremely easy and powerful. On the MATLAB™ side, the kernel code is made in such a way that the compiled component can tell the user interface about itself: it can tell (via an XML-communication scheme) what algorithms it can calculate, what are the inputs and outputs of those algorithms and what are their default values. With this information, the UI component accommodates itself automatically to the new kernel version during start-up. As mentioned, this architecture was utilized also in the design of the software for particle size analysis (see Subsection 4.2.6).

All image algorithms (except for the laser detection algorithm, see Subsection 5.3.3) introduced in this thesis, and a few experimental ones, were re-designed and re-coded. For example, four new ways of calculating bubble collapse rate were tested and all of them are currently implemented in the FrothEye kernel.

Further details of the platform will be given in an upcoming publication [50].

5.3.3. Froth Height Measurement

A typical case with instrumentation in flotation circuitry is that the pulp level can be measured accurately but the thickness of the froth layer on top of the pulp is more difficult to assess. For example, Pyhäsalmi Mine Oy has used instruments based on capacitance measurements, which are relatively inaccurate as they can provide only a few discrete height readings. According to the plant personnel, they are having reliability problems with them.

An additional result of the research was a new way of measuring the froth height and froth thickness. The measurement is based on evaluating the distance between the camera and the froth surface. From this measurement, when combined with the pulp level measurement, the froth thickness can be calculated. The need for this type of measurement came when the intensity variations caused by the changing distance between the camera and the froth were investigated.

The measurement is based on a laser triangulation method, meaning (in this case) that a laser line is projected to the froth surface at a 45° angle. Thus, the height fluctuations will cause the line to change its position in the image. Since the imaging area is near the edge of the flotation cell, the angular changes of the projected line tell about the changes of the froth slope near the edge.

To obtain the position of the projected line, a laser detection algorithm was developed and added to the kernel of the FrothEye software. As can be seen in Fig. 5.10, the laser line is missing from the middle part of the image, as it is shaded out so that the red laser line in the image would not interfere with other image processing algorithms. Other algorithms have configurable *region of interest* (ROI) areas that can be selected to be in the middle part of the image.

The development of the measurement, as well as research on the intensity variations, is ongoing and will be reported in [89].

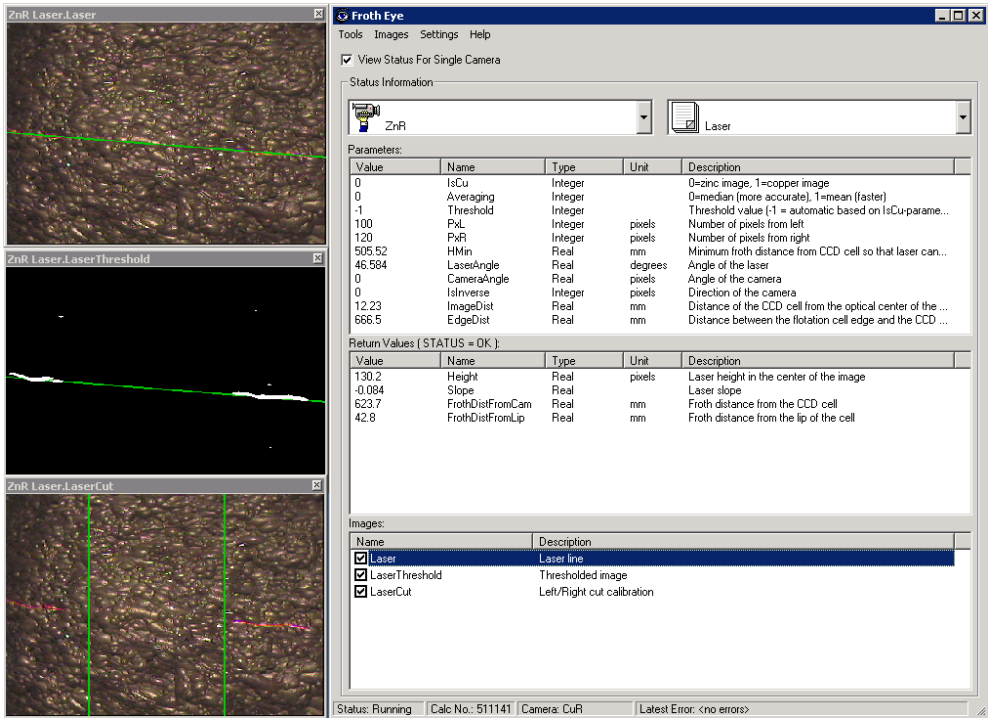

Fig. 5.10 Froth height calculated with the laser detection algorithm incorporated into FrothEye. The *LaserCut*-image shows the region of interest (ROI), *Threshold*-image shows the recognized laserpoints and *Laser*-image shows the final result.

5.4. Results

This section introduces the results obtained by using the described image analysis approach. First, the observed dependencies between the image characteristics and the process variables are discussed both for the single- and multi-camera settings. Then, closed loop control for the zinc rougher and for the copper cleaner banks is discussed. Finally, additional ways to support the operators in their daily work are introduced.

5.4.1. Dependencies

As explained earlier, as much information as possible was extracted from the images obtained with the image analyzer. Thus, the dependencies between the new image variables and traditional process variables had to be studied, and eventually five image variables were selected as the most important ones. During this selection process, many different comparison tasks were carried out and new dependencies were found. The most important findings are presented in the following.

Single Camera Analysis

The analysis for the single camera part was done for data collected from the rougher bank of the zinc circuit. It would have been interesting to compare the image variables against the XRF results from the same bank, but unfortunately there was no sampling point for the rougher concentrate (see Fig. 5.6). Consequently, comparison was made against the XRF analysis of the final concentrate, which is known to depend mainly on the zinc grade of the rougher concentrate. The following analysis was originally reported in [72].

The graphs in the following sections are based on 35 days of data, collected at one minute intervals during February and March 2001. The data collection resulted in a relatively large amount of data with a short sampling interval with respect to the time constants of the process. Thus, for noise and dimension reduction purposes, the data was first classified and the graph points present the mean values of those classes.

The bubble load variable has proven to be the best indicator of the flotation performance and, based on recent discussions with the operators of Pyhäsalmi Mine Oy, it has become an important asset in the daily operation of the flotation plant. Fig. 5.11 shows zinc recovery, zinc feed grade and froth speed as a function of froth transparency, which is the opposite of load.

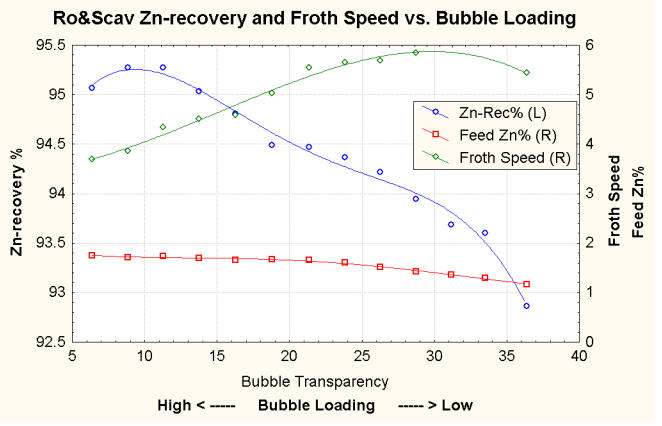

Fig. 5.11 Zn recovery (L), Zn grade of feed (R) and froth speed (R) vs. froth load.

It can be seen that zinc recovery reaches an "optimum" value when the transparency is around 10. In this range the feed grade, which is known to have a significant effect on the image variables, is almost constant and therefore is not causing this phenomenon. Another finding is that this "optimal" froth type is associated with low froth speed values, small bubbles (Fig. 5.12) and low bubble collapse rate readings (Fig. 5.13). This conjecture is supported by subjective observations made in Pyhäsalmi mine, and by expert knowledge on the subject.

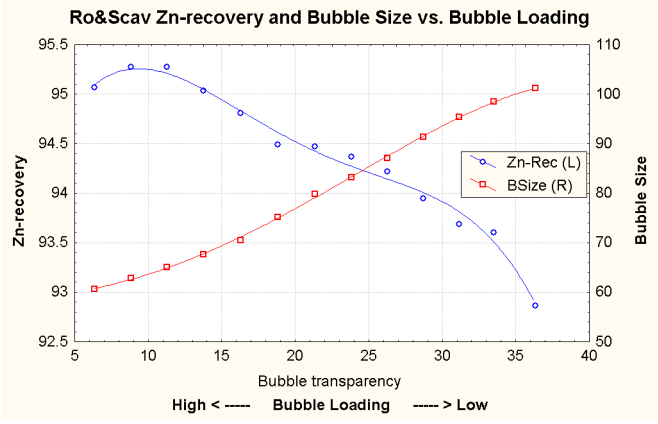

Fig. 5.12 Zn recovery (L) and bubble size (R) vs. bubble load.

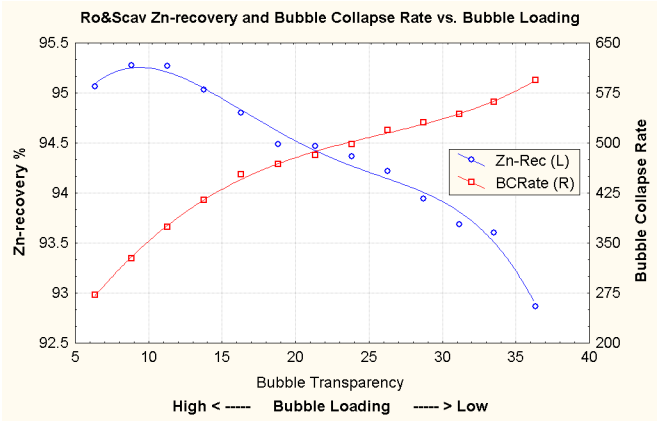

Fig. 5.13 Zn recovery (L) and bubble collapse rate (R) vs. bubble load.

The following three figures illustrate the dependencies between the image variables of the rougher bank and the final zinc concentrate grade. Fig. 5.14 shows a strong correlation between the red colour component and the zinc concentrate grade. Furthermore, it can be seen that the froth speed has negative correlation with grades, which implies that froth rich in zinc moves slower than a low grade froth.

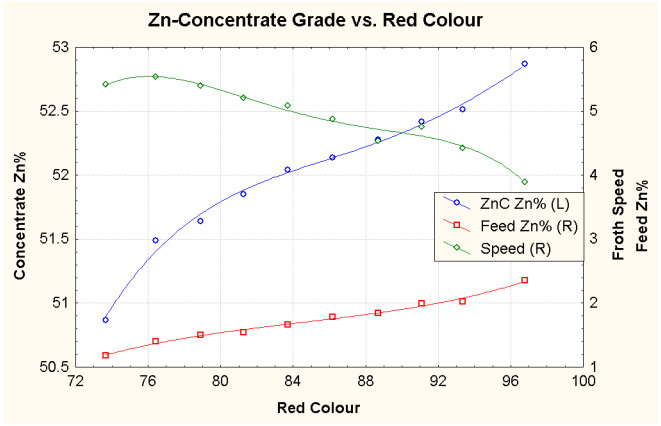

Fig. 5.14 Zn concentrate grade (L), Zn feed grade (R) and froth speed (R) vs. red colour.

And finally, rich froth is associated with small bubbles and low bubble collapse rate, as indicated in Fig. 5.15 and in Fig. 5.16, respectively. Again, this result is supported by observations.

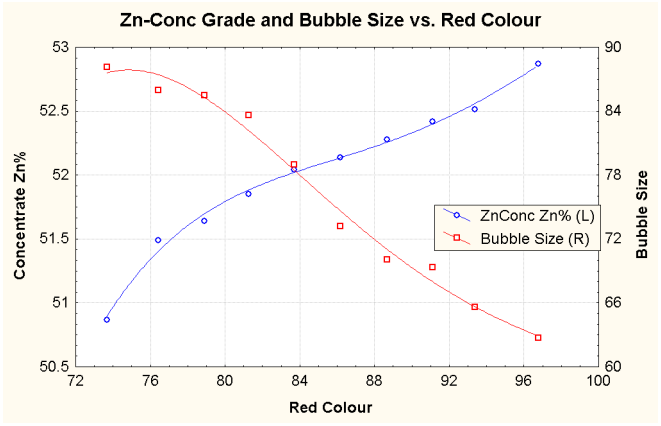

Fig. 5.15 Zn concentrate grade (L) and bubble size (R) vs. red colour.

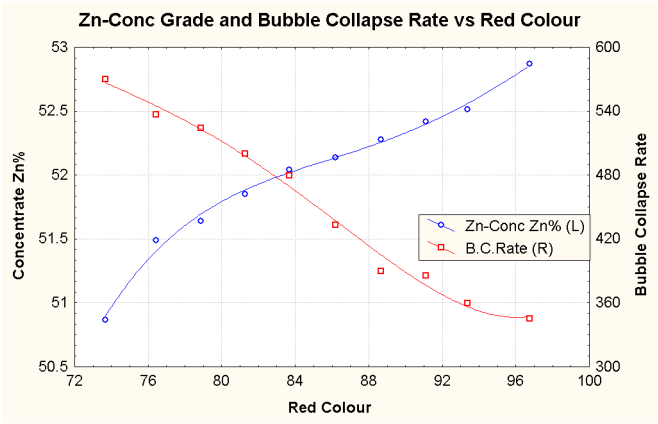

Fig. 5.16 Zn concentrate grade (L) and bubble collapse rate (R) vs. red colour.

Multi-Camera Analysis

The purpose of the multi-camera analysis was to determine whether the image variables obtained from different cells would behave in a consistent manner, and to see how well the zinc content of the final zinc product could be predicted by using these variables only.

The analysis was performed with two independent data sets from Aug. 26, 2004 – Sep. 1, 2004 (*data1*) and Sep. 6, 2004 – Sep. 10, 2004 (*data2*). The data was collected in one minute intervals and averaged into six minute data sets. Three cells were included in this study: roughing, mid-roughing and cleaning (see Fig. 5.6). The high grade cell was intended to be part of this study, but unfortunately the camera location in the cell was such that there was no continuous flow under the imaging area. Therefore, the calculated image variables had to be discarded. From each of these three cells, six image variables were selected and they are presented in Table 5.1 below.

Table 5.1 Image variables.

Variable	**Description**
Correlation	Peak value of cross correlation matrix of an image pair, see Fig. 5.5
Redness	Mean-value of Red-component of an RGB-image
Load	Load-variable that estimates the mineral content in the surface of the bubble, see Subsection 5.2.2
Speed	Speed of the froth, see Subsection 5.2.2
Bubble Size (BS)	Mean bubble size, see Subsection 5.2.2
Intensity	Mean intensity of the image

The analysis was carried out with linear multivariate methods. Therefore, the time delays between different cells were estimated and removed. It should be noted that, due to the nature of the flotation process, the delays are time-varying and assuming them fixed does introduce some errors in the results. The delays were estimated mainly based on cross correlation analysis and partly by process knowledge of the plant personnel. The delays were (*in 6 minute time steps*): from rouging to mid-roughing, *4*, from roughing to cleaning, *4*, and from roughing to measured zinc content of the final product, *6* time steps.

The consistency among different cells was analysed with Principal Component Analysis (PCA, see Chapter 4). By using the image variables described above, the first and second principal components (PCs) were calculated separately for each cell. The idea was to compare the different cells and to see if they would behave in a systematic fashion. The analysis showed that, mathematically speaking, the three cells work similarly. This is illustrated in Fig. 5.17, where the loadings of the first two principal components are shown.

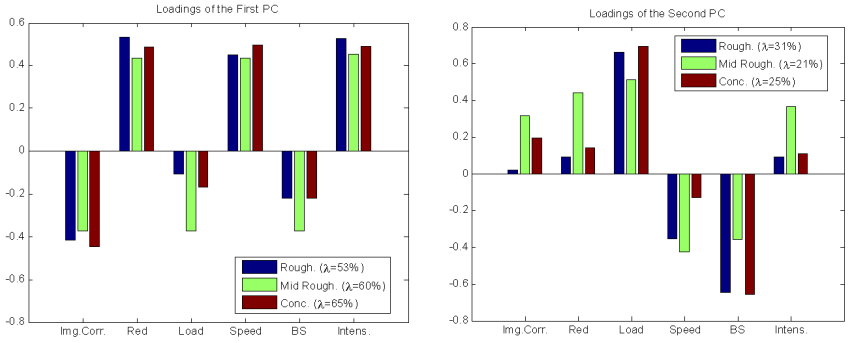

Fig. 5.17 Loadings of the first PC (left) and second PC (right) for *data1*.

The first PCs show consistent results in all three cells, where the loads of each image variable (between different cells) are roughly the same. The second PCs show consistent correlation directions, but not as identical loadings as in the first PCs.

The second data set (*data2*) shows similar results (see Fig. 5.18), with the exception of image correlation of the cleaner cell in the first PC and the bubble size of the mid-roughing cell in the second PC. However, both results clearly show consistent behaviour in the image data taken from different cells.

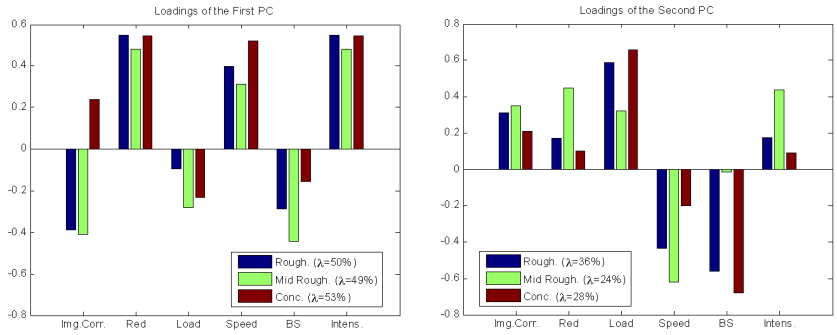

Fig. 5.18 Loadings of the first (left) and second (right) PC for *data2*.

The next step was to predict the zinc grade of the cleaner cell (ZnR Zn%) by using only the image variables as predictors.

Three recursive prediction methods were used. PCA was used as an *unsupervised* method and *Principal Component Regression* (PCR) and Partial Least Squares (PLS) as *supervised* methods. In the unsupervised methods, only the $\mathbf{X}$ data block is used in training and the $\mathbf{Y}$ data is reserved for validation. The supervised methods take advantage of both $\mathbf{X}$ and $\mathbf{Y}$ data in the teaching phase. The PCA and PLS are already covered in Subsection 4.2.4. Thus, a short introduction to PCR, based on [113], is given in the following.

Let a single image data point be denoted by a row vector $\mathbf{x}$ and the predicted concentrate grade value with a scalar y. Then one would like to obtain a *regression vector* $\mathbf{b}_R$ containing the weights used for the linear combination of the image variables in order to produce y:

$$\mathbf{x}\mathbf{b}_R = y \tag{32}$$

However, for a meaningful fitting, several measurements $\mathbf{X}$ and the corresponding grade vector $\mathbf{y}$ are needed. In theory, *Multiple Linear Regression* (MLR) would suffice and $\mathbf{b}_R$ could be solved by calculating the *pseudoinverse* of $\mathbf{X}$, denoted by $\mathbf{X}^+$ as

$$\mathbf{X}^+ = \left(\mathbf{X}^T\mathbf{X}\right)^{-1}\mathbf{X}^T \tag{33}$$

and then $\mathbf{b}_R$ would be obtained by

$$\mathbf{b}_R = \mathbf{X}^+\mathbf{y} \tag{34}$$

In practice however, there (almost) always exists *collinearity* in the $\mathbf{X}$ data, i.e. some columns are linear combinations of other columns, which is not tolerated by this approach since then $\left(\mathbf{X}^T\mathbf{X}\right)^{-1}$ would not exist. Thus, the data is said to be *ill-conditioned*.

PCR is a way to deal with ill-conditioned matrices. The idea is simply to use principal component scores of the measured variables as predictors. Since the score values are orthogonal by definition, they are always well conditioned and $\mathbf{X}^+$ can be calculated as

$$\mathbf{X}^+ = \mathbf{P}\left(\mathbf{T}^T\mathbf{T}\right)^{-1}\mathbf{T}^T \tag{35}$$

where $\mathbf{P}$ is the loadings matrix and $\mathbf{T}$ the score matrix of the PCA model, as described in Subsection 4.2.4.

The PCA estimate values (i.e. score vectors) were obtained by sliding a 48 hour history window, for which the PCA model was updated at each step. After the model was calculated, the last values of the score vectors of both principal components were stored and the analysis was advanced by one step.

The analysis cycle is presented below:

1. Take the last 480 points of history data.
2. Calculate the first two principal components for that data.
3. Calculate the score vectors of those principal components.
4. Store the final values of the score vectors.
5. Wait for the next data point, slide the history window and go to 1.

The score values obtained in this way followed the cleaner grade with a very good accuracy, as shown in the left part of Fig. 5.19, where R^2 is the *coefficient of determination*. This was a good proof of the power of image analysis in the context of mineral flotation since *only* the image variables were used to obtain this result. Also, since the time delay between the image variables of the cleaning cell and the XRF analysis of the final concentrate is on average 12 minutes, this means that the PCA approach is able to predict the zinc content in advance.

For the PCR case; *data1* was used for training and *data2* for validation. Since the PCR approach utilizes the y-data, one would expect far better correlation, especially with the training data that is shown on the right part of Fig. 5.19. However, there was only minor improvement with the training data and, for the validation data the PCR gave worse results than PCA. This means that it is essentially the first principal component alone that correlates with the output concentration. The results for *data2* are shown in Fig. 5.20.

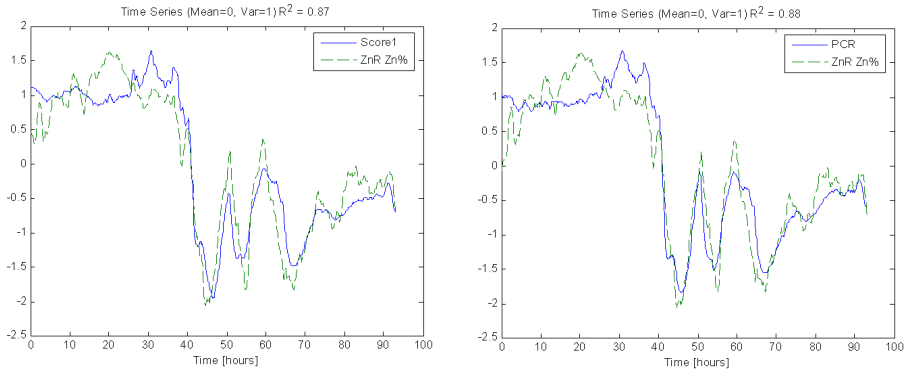

Fig. 5.19 *Data1*: Score values of the first PC in PCA approach (left) and fit for PCR teaching data (right).

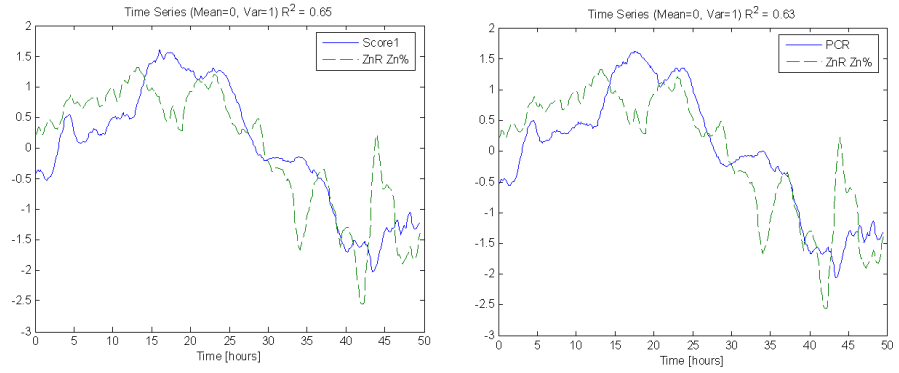

Fig. 5.20 *Data2*: Score values of the first PC in PCA approach (left) and fit for PCR validation data (right).

Finally, a PLS model was tested in a similar fashion as the PCA and PCR models (same 48 hour sliding history window was used) and the results are shown in Fig. 5.21. One interesting finding is the degradation in the correlation with the first data set since one would assume improvement, at least when compared to PCA approach, because of the additional y-side information. This is due to the changes in the time delay between the image variables and the XRF analysis of the final product.

Also, for the second data set the results are improved only slightly. However, even if the improvement is clear in terms of R^2, it is still only a minor improvement when compared to the PCA approach, which accomplished more or less the same thing completely without the aid of the *y*-side data.

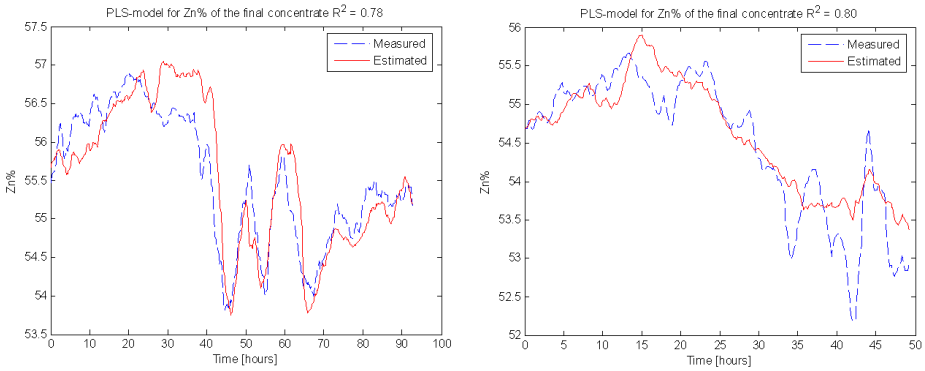

Fig. 5.21 PLS fit for *data1* (left) and *data2* (right).

5.4.2. Closed Loop Control

As stated earlier in this thesis, there is solid evidence that the calculated image variables are able to reflect the state of the flotation process. Thus, a natural step was to take advantage of this with automatic control. Several tests were carried out during the research. The most successful ones will be presented in detail in the following sections.

Copper Sulphate Controller of the Zinc Rougher Bank

Dedicated expert controllers have been used in Pyhäsalmi for a long period of time and the controller implementation had to be done in that domain. The controllers are based on prioritized *if-then* rules that are executed periodically from top down. Once a matching rule is found, the control action associated with that rule is executed and the rest of the rules are discarded. This type of rule based approach tries to mimic the logical thinking of an experienced operator in a given situation.

Such a controller had been used for controlling the copper sulphate ($CuSO_4$) feed rate for the zinc rougher circuit. Copper sulphate is used to activate the *sphalerite mineral* ((Zn,Fe)S) and is the main control variable in the zinc circuit of Pyhäsalmi mine (see e.g. [31] and [57]). The fundamental idea of the controller is to keep the operating point in a feasible area by utilizing standard process measurements, as well as XRF analysis results. The main features of the controller are:

- If two rules are activated simultaneously, the control action for the rule with a higher priority is executed.
- The controller has two possible control actions: either to increase or to decrease $CuSO_4$ by a fixed step.
- The controller is executed every 60^{th} second. This delay allows process transients, caused by the corrective step-changes, to die away before any new corrective actions are made. Consequently, the controller is only compensating for steady-state disturbances of the process.

- Set points, low alarms and high alarms can be changed by the operators. This allows them to re-tune the controller if there are considerable changes in the ore quality.

Since the new image variables were available, they were introduced to the control logic as shown in Fig. 5.22. The controller rules and limit values are largely based on the knowledge of the process experts at the flotation plant.

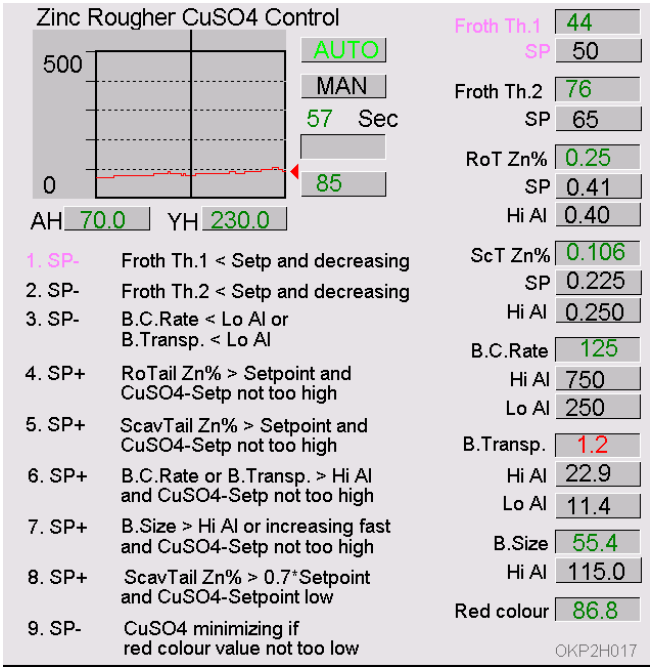

Fig. 5.22 The user interface of the copper sulphate controller.

The introduced image variables were (the names used in the controller's user interface are shown in parenthesis): bubble collapse rate (*B.C.Rate*), bubble transparency (*B.Transp.*) i.e. the load variable, bubble size (*B.Size*) and mean of the red component of the image (*red colour*).

The controller performance evaluation is a difficult task since so many variables influence the achieved flotation performance. However, based on long term data collection campaign (2000-2004) and on comparison of the flotation results during the years 1995-2004, the mill management has estimated that the controller accounts roughly for an improvement of 1.3 percentage units in zinc recovery. This in turn yields 200 000-300 000 € annual increase in profit [P5].

Cyanide Controller of the Copper Cleaner Bank

A similar controller modification to the cyanide[2] set-point in the cleaner bank of the copper circuit is reported in [P4]. It was motivated by a PLS analysis that was done on: froth speed, bubble collapse rate, bubble size distribution, froth load and the red colour component of the froth. The initial idea was to use the PLS technique for predicting the zinc grade in the final copper product, since the plant had experienced problems in minimizing its value and since it was found out that the image variables reacted to process disturbances roughly 30-40 minutes earlier that the XRF analysis did. Note that after copper flotation the next phase is zinc flotation (see Subsection 3.3.2), and therefore zinc should be depressed in the copper flotation stage.

Unfortunately, relatively poor results were obtained with the PLS approach. However, when studying the loadings of the PLS model, they indicated that the load variable and bubble collapse rate had the highest values. When investigating these two variables in detail, it was found that they were able to indicate undesired operating points of the process. This conclusion was made based on cluster analysis, where the first step was to divide zinc concentrate readings into three classes, namely to *good*, *neutral* and *bad* (see Table 5.2). The class borders for these classes were defined by the plant engineers.

Table 5.2 Classes for zinc concentration in the final copper product.

Class	**Range [Zn% in copper product]**
Good	< 1.75
Neutral	1.75 - 2.5
Bad	> 2.5

The next step was to plot the classified image data on *froth load – bubble collapse rate plane*, as shown in Fig. 5.23. As seen, the good and bad classes are separated reasonably well. This property was then utilized in the control logic for the cyanide set-point, by introducing the following rule:

IF *load* > 62 AND *bubble collapse rate* < 4.5 THEN

Increase cyanide set-point to reduce Zn%.

END IF

The purpose of the rule is to prevent the process from entering the undesired operating area that is illustrated by the square in the lower-right corner of Fig. 5.23.

[2] Cyanide is used as a depressant. Its purpose is to prevent the activation of the sphalerite mineral, because it is flotated in the following zinc circuit.

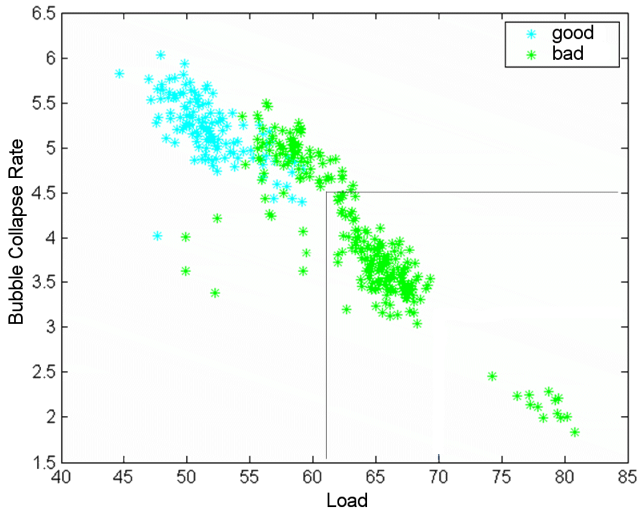

Fig. 5.23 Cluster analysis of the image data.

The controller performance was evaluated with four data sets where in two of them the new controller was used, whereas the old controller was used in the other two. The results showed a decreased mean value and standard deviation for the zinc percentage in the final copper product when the new controller was utilized, as illustrated in Fig. 5.24. The comparison was done to gain a first indication whether or not the new rule was working and the results obtained can only be considered preliminary. Similar long term evaluation as in the previous case should have been carried out to get a clearer picture of the effects of this new rule. Unfortunately, this was never done due to the limited resources of the research group.

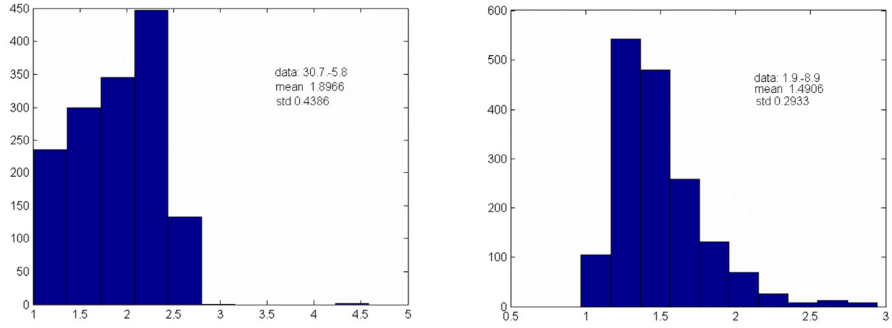

Fig. 5.24 Controller performance comparison. The histograms show the Zn% in the final copper concentrate (x-axes). New controller (right) shows decreased mean and standard deviation.

5.4.3. Support for the Operators

One important aspect of the research was to help operators in their daily work and in decision making. Consequently, the most important image variables are utilized in control, and the operators can fine-tune the set-points and alarms, as described

earlier. Another valuable task is to include the most important variables in the namespace of the automation system, which in turn makes it possible to display them on the screens in a similar manner as any other process variable. This means that history trends are automatically calculated for these variables and are available for the operators.

To further leverage the usage of image information, an *image history database* was implemented by the author so that the operators (both experienced and newer recruits) can not only see the current state of the process, but can also go back in history (see Fig. 5.25). This is especially useful if there is something out of the ordinary in the history trend curves – say a peak in XRF measurement(s). In the case of such a problem, the operator can use the visual changes in the froth appearance together with the numerical values of other process data to get a clearer picture of the situation.

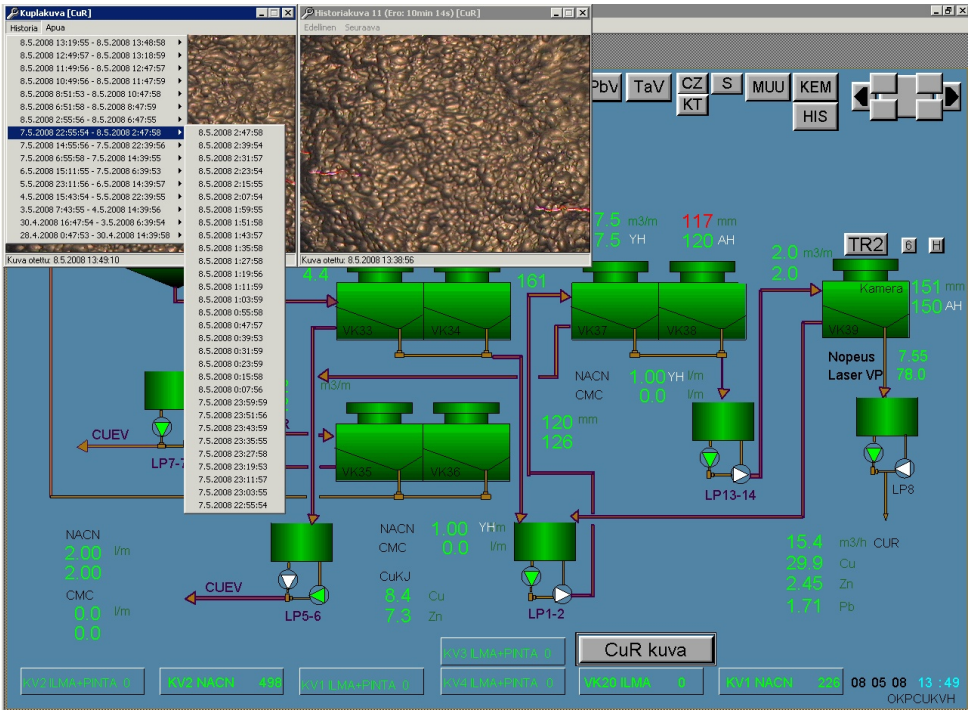

Fig. 5.25 Image history for operators.

The image history is collected from each camera at a one minute interval for the first 30 minutes, at a two minute interval for the second 30 minutes and so on. In this way, more frequent information is available from the recent history but, if needed, froth images are available also for older events. Furthermore, in the current setting, the camera signals are routed to a video multiplexer located in the control room and one of the monitors is reserved for live video feed coming from the cameras.

6. Grade Estimation with Colour and Spectral Analysis

This chapter describes the research regarding spectral measurements and their utilization, and it is based on the publications [P5] and [P6]. It is a natural continuation of the work described in Chapter 5.

The research done with the image analysis of flotation froths provided strong evidence on the importance of the froth colour as an indicator of grade. This motivated the continuation along this path and the next step was to study whether or not a traditional RGB camera – designed to operate on the same wavelength range as the human eye (λ=380-760 nm) – actually would be an instrument accurate enough for colour measurements. This question had been asked before and was studied with spectral measurements as stated earlier in Subsection 5.2.1, but at that time sufficient long-time data collection was not possible and only preliminary results were therefore obtained (see [48] and [98]). The main reason for this was that the total reflection points caused problems, and the modifications to the physical setup required to compensate for these resulted in new problems with respect to reliable on-line operation [48].

Once reasonably priced *imaging spectrographs* became available, the research on spectral analysis was continued with such a device, operating in the visible and near-infrared (VNIR) range (λ=400-1000 nm). The VNIR range was selected because previous laboratory experiments indicated that there, in fact, was correlation between the grade and the spectrum beyond the wavelength range of the human eye. This was reported by Sirén in [98], where two wavelength areas were identified around 500 nm and 820 nm.

The spectrograph (Specim Imspector V10, λ=400-1000 nm, 5 nm spectral resolution, see [102] for further details) is mounted to a monochrome CCD-camera (see [3] for details), and the spectral images are formed by passing light from imaging optics to the spectrograph through an *entrance slit*. The obtained line (light) is transformed into a 2D-image (spectrum) by passing the light through a

prism-grating-prism (PGP) component. The line spectra obtained in this way makes it possible to cancel out the undesired total reflectance points simply by discarding the saturated values, as will be shown in the following.

6.1. Froth Analysis

This section describes the method that was used for comparison between an RGB camera and a spectrophotometer. The results obtained from this analysis gave motivation for further studies that are explained later, starting in Section 6.2.

6.1.1. Prototype for On-Line Measurements

In order to be able to compare the measurement capabilities of an RGB Camera and a spectrophotometer, an enclosure was designed, which made it possible to obtain both image- and spectral data simultaneously from the same location. Fig. 6.1 shows the enclosure where the RGB camera and the spectrophotometer are mounted side by side. On the right there is an illustration of the line that is "seen" by the spectrophotometer.

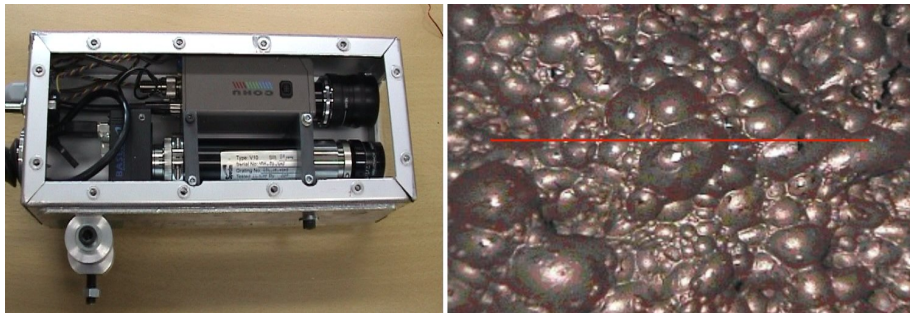

Fig. 6.1 RGB- and spectral data was obtained from same location simultaneously. The imaged line position is illustrated on the right (not in scale).

When considering the image, it is easy to see that in different positions of the line there will be total reflection points (high intensity values) as well as bubble borders (low intensity values). An example of such spectra along the line is shown in Fig. 6.2, where the peak values correspond to total reflection points, which can be removed by a simple pre-processing algorithm.

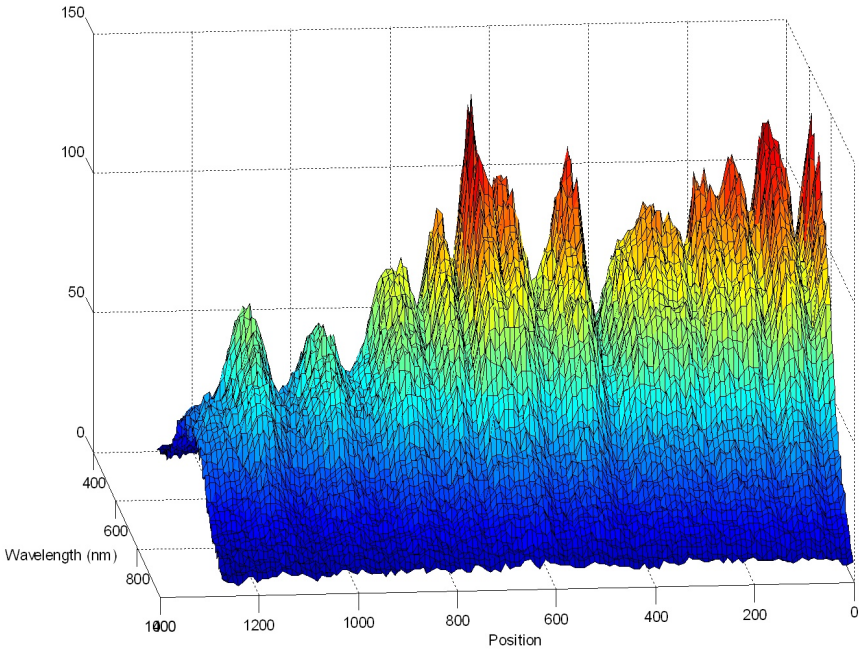

Fig. 6.2 An example of the line spectrum.

The RGB camera and spectrophotometer were installed on the last cell of the zinc cleaner circuit (see Fig. 5.6), which produces the final concentrate. Data was collected from both devices and XRF results for the cleaner bank were recorded. The recorded variables were the mean values of R, G, B components, the mean intensity of the RGB image, line spectra and the zinc, copper and iron contents of the concentrate flow.

After this, the collected data was synchronized in time and modelled. A standard Multi Linear Regression (MLR, see Subsection 5.4.1) model was used for the well conditioned RGB data. The spectral data, however, is highly collinear and, therefore, the MLR approach would not suffice [37]. Thus, a PLS (see Subsection 4.2.4) model was used, since it is known to cope well with collinearity and is a commonly used method when analysing spectral data [113].

6.1.2. Results

The prediction results for the two models are shown in Fig. 6.3. They were obtained by using independent validation data and, as can be seen, both models give satisfactory results. However, based on the images, it seems that the PLS model gives slightly better results.

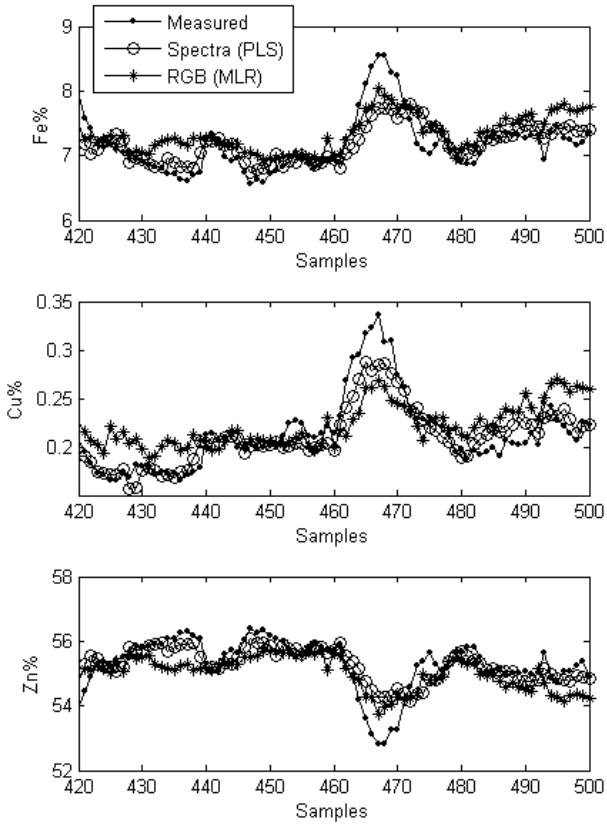

Fig. 6.3 Prediction results for RGB- and spectral-data. Sampling interval is one minute.

This was confirmed by correlation analysis, which indicated that the PLS model can outperform the MLR model in the prediction of all three grades. The correlation coefficients are shown in Table 6.1.

Table 6.1 Correlation coefficients of the predicted and measured metal contents.

Model/Metal	**Fe**	**Cu**	**Zn**
PLS (Spectrophotometer)	0.78	0.92	0.80
MLR (RGB Camera)	0.71	0.87	0.75

6.2. Slurry Analysis

After it was shown that spectral analysis is a powerful technique in grade prediction, a novel idea for its utilization in the mineral processing industry was conceived by Saloheimo [92]. The innovation was to make the spectral analysis

from slurries instead of the froth and to combine the information with the XRF analysis in order to obtain almost continuous estimates of the grades.

There was a real need for this type of fast measurement since the XRF analyzers typically provide accurate but relatively sparse measurements. This is due to the fact that these analyzers are bulky and expensive and are thus used to process several different flows sequentially. The sample time obviously depends on the number of lines to be analyzed. If a more frequent analysis is required for a given flow line, the sampling frequency is typically (almost) doubled by duplicating the flow in the multiplexed sample ring. However, this approach works only if there are a small number of such lines. There are also approaches for improved accuracy, for example, by means of data reconciliation (see [28]). A typical sampling interval in Pyhäsalmi is about 18 minutes for a line and even though the process is relatively slow, there are still situations where a more rapid analysis would be desirable. A sudden process disturbance is an example of such a situation. Furthermore, it was thought that the prediction accuracy of the XRF analyzer could be improved with this technique.

Since Outotec Minerals Oy (formerly Outokumpu Technology Minerals Oy) had a long experience regarding the XRF analysis, they offered a *jet flow cell* similar to the one that is used in the Courier® XRF analyzers (see [82]) to be used in this study. The cell is designed to give a representative sample of the material flow and seemed to be well suited for the spectral analysis.

6.2.1. Initial Laboratory Tests

In order to get assurance on whether or not the slurry analysis approach would work, it was thought that a small scale laboratory experiment should be conducted. This was carried out by collecting samples from the natural overflow of the rougher, scavenger and cleaner banks of the zinc circuit (see Fig. 5.6). In addition to this, other samples were also collected from the copper circuit, and the very first laboratory tests were carried out with different mixtures of *Magnetite* (Fe_3O_4) and *Hematite* (Fe_2O_3) minerals, but the results of these experiments are omitted here, because they would bring no additional value to the following discussion.

The samples were divided into two containers; one for spectral analysis and one for laboratory analysis. The results of the laboratory analysis for the three samples are shown in Table 6.2 below. As seen, there are large variations especially in zinc and iron contents, which were expected to be seen in the spectra.

Table 6.2 Laboratory analysis for zinc circuit samples.

Bank	**Zn%**	**Cu%**	**S%**	**Fe%**	**Pb%**
Rougher	45.39	0.29	31.3	12.0	0.20
Scavenger	12.43	0.71	29.7	26.0	0.22
Cleaner	56.44	0.32	32.5	8.5	0.22

The samples reserved for spectral analysis were approximately 5 litres in volume and they were circulated continuously in a *pilot test system* consisting of a small tank, adjustable pump and a jet flow cell (Fig. 6.4). Different setups with respect to illumination, imaging conditions and different jet flow cell window materials were tested and the analysis showed that once the basics are in order, the results are consistent. In other words, the spectrum of the illuminating lamp must be wide enough and the illumination geometry must be selected in a way that the total reflection from the window is minimized. Consequently, the analysis was carried out with a single halogen lamp (12V, 50W, 4700K) as a light source, and a clear 50 μm mylar film was used as a jet flow cell window.

The samples were analyzed by preparing a batch for circulation and measuring the spectra while diluting the sample with water. This made it possible to obtain different *solids content* (SC) values. Once the sample was processed, the system was washed thoroughly with water and the same sequence was repeated for the next sample.

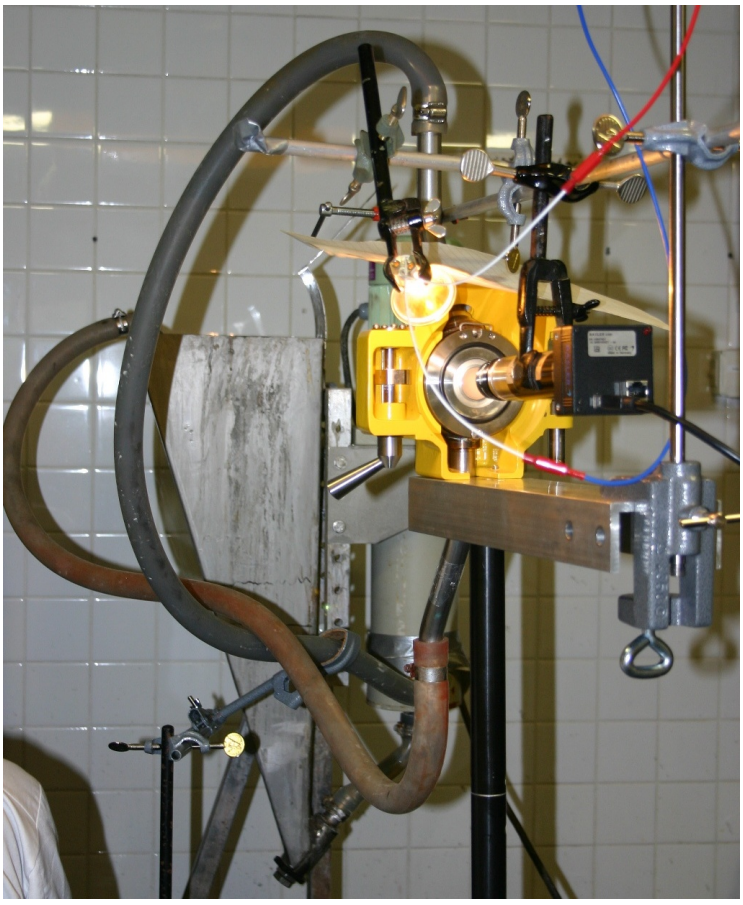

Fig. 6.4 Pilot test equipment for slurry X-Ray Fluorescence analysis.

The results of the analysis are shown in Fig. 6.5, where there are 11 spectra drawn with different line types depending on the origin of the sample. The SC values for each sample are shown in the legend texts. When comparing the spectral responses to the laboratory analysis results, it can be seen that the mineral content dominates the shape of the spectrum and changes in SC cause only minor variation. This is emphasized in the small sub-figure.

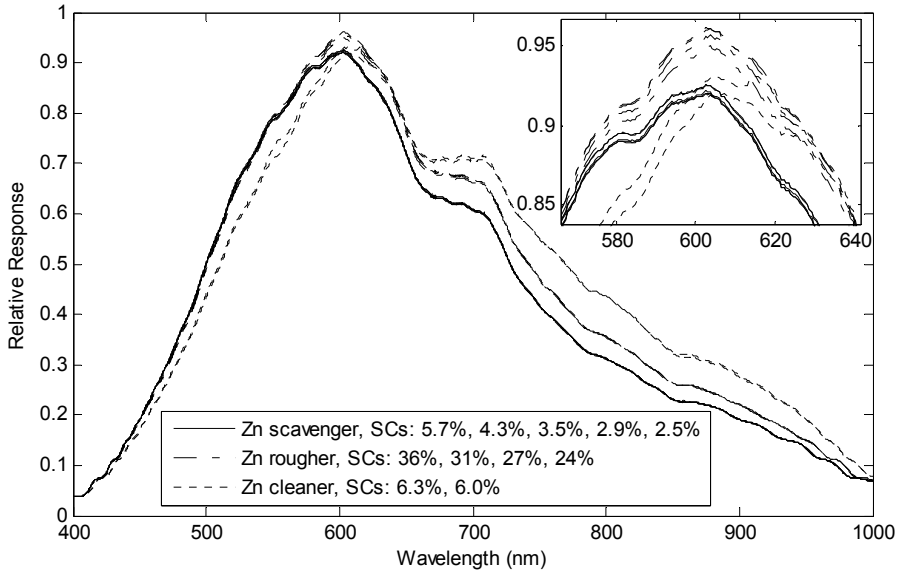

Fig. 6.5 Spectral responses for different flotation cells and solids contents (SC). The peak area is emphasized at the top right hand corner.

6.2.2. Prototype for On-Line Measurements

Since the pilot test suggested that the varying mineral content of the slurry causes changes to the spectra, a prototype capable of performing continuous on-line measurements was built. The prototype realized the same measurement setup that was used in the pilot test, except for the thin film-window which must be used in XRF analyzers to pass X-ray radiation through. Since the film is thin, it is easy to imagine that it does not last very long in the "liquid sandblasting" that it is subjected to. Fortunately, in the case of spectral measurements done in the VNIR range, there are no such restrictions and, consequently, the thin film could be replaced with a durable *sapphire window*, rendering the system practically maintenance free.

The prototype is illustrated in Fig. 6.6. It included a desktop PC for data acquisition and analysis purposes. The PC was connected to the plant's automation system via a wireless local area network (WLAN) connection. All analysis equipment was placed in a slightly pressurized protective housing in order to keep the instruments

clean. To prevent condensation, an additional dried instrument air flow was directed to the jet flow cell window.

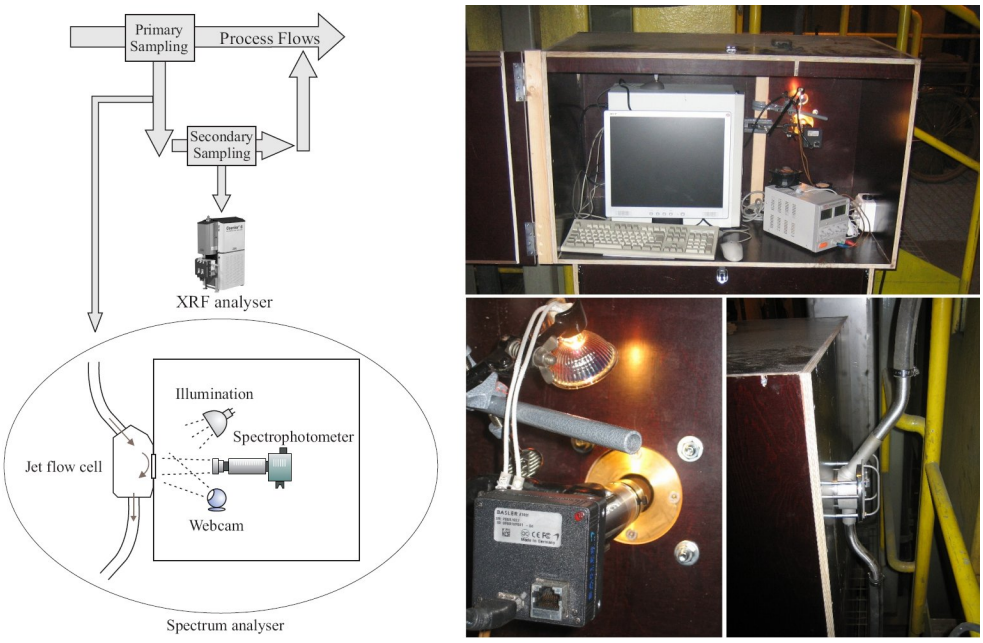

Fig. 6.6 Prototype of the analyzer measuring the concentrate flow of the zinc cleaner circuit. The sample is taken from the primary sampling line of the XRF analyzer.

The prototype was equipped with remote operating capabilities, which made it possible to do research work remotely at the university. There was also a web-camera monitoring the cell window.

A continuous sample flow was needed for the analysis, which was conveniently obtained from the primary sampling line of the XRF analyzer, as indicated in Fig. 6.6 above. The plant personnel selected the concentrate flow of the zinc cleaner circuit as the most interesting place to start this type of study.

6.2.3. Modelling & Results

As explained earlier, a Partial Least Squares (PLS) model was a natural choice for modelling this type of spectral data. However, as expected, a standard PLS model would not suffice because of the changes in the operating point of the process (these are mainly due to variation in the properties of the incoming ore). Indeed, the tests showed that a static PLS model calculated from a fixed data set remained valid for about an hour [P8].

Fortunately, in this setting the purpose was to be able to predict the grades while waiting for a fresh XRF sample. Therefore, all the previous XRF samples could be used to improve this estimate. A modelling method called *recursive Partial Least*

Squares (rPLS, see [14], [34], [85] and [86] for details) is a modification of the standard PLS algorithm. In rPLS the model is updated recursively with new data points and usually a forgetting scheme is used to emphasize the latest measurements. Based on the literature, this was an excellent method for this particular application and thus the *fast kernel-based rPLS* algorithm, presented by Dayal and MacGregor [14], was used to test it.

The results obtained with this approach were very good; the rPLS approach was able to predict the elemental and solids content accurately. This proved that the method could be applied as a supplement to XRF analysis. The *root mean square* (RMS) values for 15 hours of spectral data at a sampling interval of 10 seconds are given in Table 6.3. As can be seen, the prediction errors are only a few percents, except for the 18.4% error in the estimation of the low grade copper.

Table 6.3 Root mean square error of the rPLS analysis. Mean values and standard deviations for grades and SC value are shown for comparison.

	Error (RMS)	**Mean**	**Std**
Fe	0.33	9.91	1.27
Cu	0.16	0.87	0.78
Zn	0.56	52.39	2.17
S	0.14	34.16	0.52
SC	1.39	36.43	2.42

Further details of the modelling and of the results are given in [P8] and [29]. Also, a separate model for estimating low grade values is introduced in [26].

As shown, the introduction of this new technique provided an answer to the need for fast grade measurement. An example of the possibilities of this technique in the context of sudden process disturbance (discussed in the beginning of this section) is shown in Fig. 6.7. It can clearly be seen, that the rPLS estimate is able to indicate the drop in the zinc content almost immediately, giving the plant operators the possibility to react sooner than before, which in turn decreases the negative influence of the disturbance.

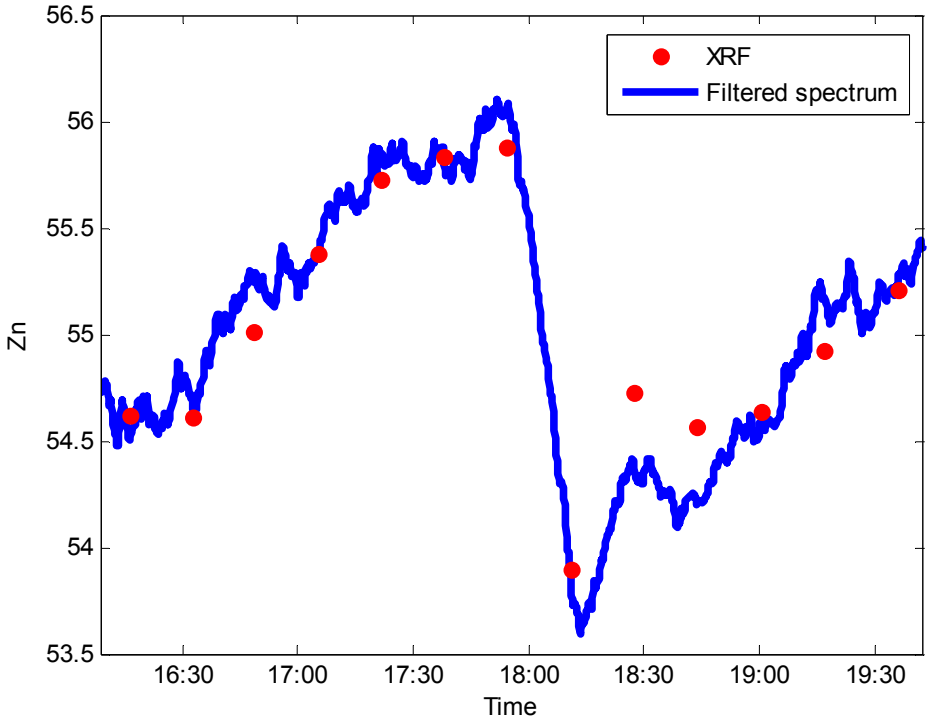

Fig. 6.7 An example of the measurement capabilities of the spectrum approach; the process disturbance can be detected earlier from the new estimate.

6.3. Current Status of the Research

Based on the favourable results obtained, the slurry analysis prototype was extended into a multichannel version [27]. This natural continuation of the research was already taken into account when the spectrophotometer was purchased; the selected device makes it possible to replace the imaging optics with a fibre optics bundle that divides the imaged line into segments, corresponding to spectra obtained from each fibre optics cable. The amount of lines is configurable and up to 150 lines can be connected to a single spectrophotometer. Obviously this has advantages; the price of the multichannel version remains low, even if the number of lines increases; and the data acquisition can be done with a single image grab, just as before, so the complexity of the algorithms does not increase notably.

At its current state the multichannel version is running on 7 lines in Pyhäsalmi and the results are being integrated to the automation system for evaluation purposes. This is illustrated in Fig. 6.8, in which the traditional XRF results (updated every 18 minutes) are shown on the left and the nearly continuous spectral analysis results on the right.

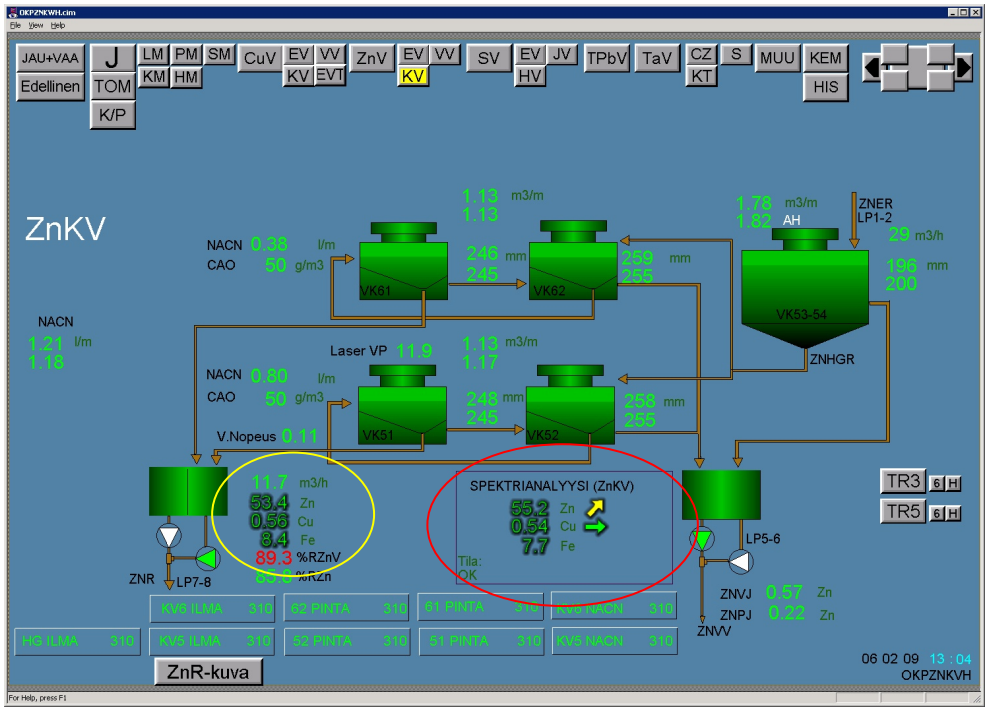

Fig. 6.8 The new estimates (red circle) are integrated into the automation system where the operators can compare the performance with the traditional XRF measurements (yellow circle).

The idea is to gather operator experience on the usefulness of these new measurements in the control of the flotation process. To help the operators detect sudden disturbances, an animated arrow estimating the gradient direction is shown next to the numerical values. In the case of sudden disturbance, like the one presented in Fig. 6.7, the yellow arrow next to Zn reading would quickly turn to point downwards and its colour would change to red.

7. Conclusions

The mining, mineral and metal industry (MMMI) might be considered rather conservative in many respects. However, since the amount of ore processed on a yearly basis is typically expressed in millions or tens of millions of tons, even a slight improvement in performance – say a 1% increase in recovery – can lead to substantial economical benefits. For example, in the case of Pyhäsalmi mine, which processes "only" 1.4 million tons of ore per year, this 1% increase in copper recovery alone would amount to roughly 500 000 € increase in annual profit with the current metal prices.

This has motivated equipment vendors, researchers and plant personnel to develop new technologies that will get them closer to the optimum. This thesis contributes to this development with an application oriented approach, in which machine vision technologies have been utilized in the context of a mineral concentration process.

Chapter 4 of the thesis presents a new approach to particle size analysis done from a moving conveyor belt. Although the system is applied to a mining process, the results may be generalized to other types of processes also; from the image analysis point of view it is irrelevant what the imaged material is.

Then, the benefits of image analysis of flotation froths are studied and the results presented in Chapter 5. The research was started with a single imaging station, installed in the rougher cell of the zinc flotation circuit, and already with that single installation very good results were obtained. Later on, the system was extended to cover more cells in the zinc and copper circuits, and the obtained data was used in many ways beneficial both to controlling of the plant and to scientific research. This thesis has increased the knowledge of flotation processes and possibilities of utilizing image analysis in them. One of the results shown, namely the introduction of image variables into one of the closed loop control algorithms of the zinc rougher circuit, could also be evaluated in economic terms; the estimated yearly benefit was 200 000-300 000 €.

Furthermore, the investigations with respect to colour and grade led to a completely new way of integrating the traditional X-Ray Fluorescence (XRF)

analysis and spectral measurements. The resulting system is a supplement to the existing XRF analyzers, enabling them to provide nearly continuous grade measurements as opposed to the sparse values that were obtained every 10-20 minutes before this improvement. The research and the results related to this are reported in Chapter 6 and, even though the work is still in progress, the results obtained so far (and reported in this thesis) confirm its usefulness in the context of mineral flotation. In fact, the excellent results obtained during this study have motivated Outotec Minerals Oy to consider commercialization and it is likely that these measurement capabilities will be available in future versions of Courier® XRF analyzers.

The work presented in this thesis will continue; as mentioned, the results presented in Chapter 6 are likely to be commercialized, the usage of the FrothEye software and the supporting tools will continue in Pyhäsalmi and new application areas for the machine vision platform will be sought. Furthermore, modelling of the ore transportation chain will continue and the benefits of spectral measurements will be studied with the current particle size analysis system (actually, spectral measurements have already been integrated with other measurements). The spectral data obtained from the ore can be combined with the segmentation results and thus each identified particle can be complemented with the new data. This can then be used in the identification of invaluable particles and, possibly, in ore type detection. The first results of this approach will be reported in an upcoming publication by Pietilä and Haavisto [84].

Finally, a quote[3] describing the author's state of mind when writing this final chapter: *"That's pretty much all that I have to say about the subject"*.

[3] From the movie *Forrest Gump*.

References

[1] Aldrich C., Moolman D. W., Gouws F. S., Schmitz G. P. J., "Machine learning strategies for control of flotation plants", Control Engineering Practice, Vol. 5, Issue 2, 1997, pp. 263-269.

[2] Bartolacci G., Pelletier P., Tessier J., Duchesne C., Bosse P.-A., Fournier J., "Application of numerical image analysis to process diagnosis and physical parameter measurement in mineral processes – Part I: Flotation control based on froth textural characteristics", Minerals Engineering, Vol. 19, Issues 6-8, 2006, pp. 734-747.

[3] Basler Vision Technologies, "Basler A102f - User's Manual", 2005.

[4] Bonifazi G., Massaci P., Meloni A., "3d froth modelling by digital image processing", In Proceedings of the XXI international mineral processing congress (IMPC), Rome, Italy, 2000.

[5] Bonifazi G., Serranti S., Volpe F., Zuco R., "Flotation froth characterisation by optical-digital sectioning techniques", In Proceedings of the international conference on quality control by artificial vision (QCAV98), Takamatsu, Kagawa, Japan, 1998.

[6] Box D., "Essential COM", Addison-Wesley, ISBN 0-201-63446-5, 1998.

[7] Brown N., Dioses J., van Olst M., "Advances in flotation process control at Cadia Hill gold mine using froth imaging technology", In Proceedings of the SME annual meeting, Denver, USA, 2001.

[8] Cipriano A., Guarini M., Vidal R., Soto A., Sepulveda C., Mery D., Briseno H., "A real time visual sensor for supervision of flotation cells", Minerals Engineering, Vol. 11, Issue 6, June 1998, pp. 489-499.

[9] Clark R. N., "Chapter 1: Spectroscopy of Rocks and Minerals, and Principles of Spectroscopy", in Manual of Remote Sensing, Vol. 3, Remote Sensing for the Earth Sciences, (A.N. Rencz, ed.) John Wiley and Sons, New York, 1999, pp. 3-58.

[10] Crida R.C., de Jager G., “Multiscalar rock recognition using active vision”, Proceedings of the IEEE International Conference on Image Processing, September 1996.

[11] Cocanour J.B., Harbuck D.D., Odekirk S.B., "Real Time Process Control Using Video Photometry", Annual TMS Meeting, San Francisco, USA, 1994.

[12] Crida R.C., de Jager G., "Rock recognition using feature classification", In: Communications and Signal Processing (COMSIG-94), Stellenbosch, South Africa, 1994, pp. 152-157.

[13] Crozier R.D., “Flotation: Theory, Reagents and Testing”, Pergamon Press, Oxford, 1992.

[14] Dayal B., MacGregor J., "Recursive exponentially weighted pls and its applications to adaptive control and prediction", Journal of Process Control 7 (3), 1997, pp. 169–179.

[15] de Jong S., “SIMPLS: an alternative approach to partial least regression”, Chemom. Intell. Lab. Syst., Vol. 18, 1993, pp. 251-263.

[16] de Waal P., Du Plessis F.E., "Automatic Control of a High-Tension Roll Separator", In: Heavy Minerals Conference 2005, Society for Mining, Metallurgy, and Exploration, Florida, 16–19 October 2005, pp. 241–249.

[17] de Waal P., "Tomorrow's Technology - Out of Africa - Today", In: Africa's Base Metals Resurgence 2007, The Southern African Institute of Mining and Metallurgy, Namibia, 23-25 July, 2007.

[18] Farfán c., Salinas R., Cifuentes G., "Rock segmentation and measures on gray level images using watershed for sizing distribution in particle systems", Revista Eletrônica Ciencia Abierta, 2006.

[19] Geladi P., Kowalski B. R., “PLS Tutorial”, Anal. Chim. Acta, 185(1), 1986.

[20] Girdner K., Handy J., Kemeny J., “Improvements in fragmentation measurement software for SAG mill process control”, SAG2001 Conference, Vancouver, Canada, 2001, 2, pp. 270-281.

[21] Girdner, K., Kemeny, J., Strikant, A., McGill, R., "The Split system for analyzing the size distribution of fragmented rock", Proc., FRAGBLAST-5 Workshop on Measurement of Blast Fragmentation, Montreal, Quebec, Canada, 1996, pp. 101–108.

[22] Glembotskii V.A., Klassen V.I., Plaksin I.N., “Flotation”, McGraw-Hill, New York, 1972.

[23] Gonzalez, R. C., Woods, R. E., "Digital image processing", Prentice-Hall, 2002, ISBN 0-201-18075-8.

[24] Guarini M., Cipriano A., Soto A., Cueslaga A., "Using image processing techniques to evaluate the quality of mineral processing", In Preprints of the sixth international conference on signal processing, applications and technology, Boston, USA, 1995.

[25] Guyot O., Monredon T., LaRosa D., Broussaud, A., "VisioRock, an integrated vision technology for advanced control of comminution circuits", Minerals Engineering, 2004, 17, pp. 1227-1235.

[26] Haavisto O., Hyötyniemi H., "Recursive Multimodel Partial Least Squares Estimation of Mineral Flotation Slurry Contents Using Optical Reflectance Spectra", Analytica Chimica Acta, doi:10.1016/j.aca.2008.11.017, 2008 (in press).

[27] Haavisto O., Kaartinen J., "Multichannel Reflectance Spectral Assaying of Zinc and Copper Flotation Slurries", International Journal of Mineral Processing. Submitted in 2008.

[28] Haavisto, O., Kaartinen J., Hyötyniemi H., "Improving the accuracy of flotation grade measurements by data reconciliation", The 6th International Conference on Intelligent Processing and Manufacturing of Materials - IPMM-2007, Salerno, Italy, 24-29 June, 2007.

[29] Haavisto O., Kaartinen J., Hyötyniemi H., "Optical spectrum based estimation of grades in mineral flotation", International Conference on Industrial Technology - ICIT 2006, IEEE, Mumbai, India, December 15-17 2006, pp. 2529-2534.

[30] Hahne R., Pålsson B.I., Samskog P.O., "Ore characterization for-and simulation of-primary autogenous grinding", Minerals Engineering, 2003, 16, pp. 13-19.

[31] Hasu V., "Design of experiments in analysis of flotation froth appearance", Helsinki University of Technology, Control Engineering Laboratory, Finland, Report 114, 1999.

[32] Hasu V., Hätönen J., Hyötyniemi H., "Analysis of flotation froth appearance by design of experiments", IFAC Workshop 22- 24 August 2000, Finland.

[33] Haykin S., "Neural networks: A comprehensive foundation", 2 ed., Prentice Hall, Inc., 1999.

[34] Helland K., Berntsen H., Borgen O., Martens H., "Recursive algorithmfor partial least squares regression", Chemometrics and Intelligent Laboratory Systems 14, 1991, pp. 129–137.

[35] Holtham P. N., Nguyen K. K., "On-line analysis of froth surface in coal and mineral flotation using JKFrothCam", International Journal of Mineral Processing, Vol. 64, Issues 2-3, March 2002, pp. 163-180.

[36] Hyötyniemi H., Helsinki University of Technology, private communication.

[37] Hyötyniemi H., “Multivariate Regression – Techniques And Tools”, Helsinki University of Technology, Control Engineering Laboratory, Finland, Report 125, 2001.

[38] Hyötyniemi H., Hasu V., Hätönen J., Ylinen R., "*’Data mining’* for mining data", XXI International Mineral Processing Congress, Rome, Italy, July 23-27, 2000, pp. 39-45.

[39] Hyötyniemi H., Ylinen R., "Modeling of visual flotation froth data", Control Engineering Practice, 8(3), 2000, pp. 313-318.

[40] Hätönen J., “Image analysis in mineral flotation”, Helsinki University of Technology, Control Engineering Laboratory, Finland, Report 116, 1999.

[41] Hätönen J., Hyötyniemi H., Bonifazi G., Serranti S., Volpe F., Carlsson L.-E., "Using PCA in controller strategy design for a flotation process", 14th IFAC World Congress, Beijing, P.R. China, 5th - 9th July, 1999, pp. 385-390.

[42] Hätönen J., Hyötyniemi H., Miettunen J., Carlsson L.-E., "Using image information and partial least squares method to estimate mineral concentrations in mineral flotation", IPMM'99 - The Second International Conference on Intelligent Processing and Manufacturing of Materials, Honolulu, Hawaii, July 10-15, 1999, pp. 459-464.

[43] Höskuldsson A., "Prediction Methods in Science and Technology", Thor Publishing, Denmark, 1996.

[44] IMSOC, "Froth Image Analyser v7.1.0 - User Manual", 2004.

[45] Inmet Mining Corporation, “Pyhäsalmi Annual Review 2007”, <www.inmetmining.com/Theme/Inmet/files/pdf/ 2002_Annual_Report_Pyhasalmi.pdf>, referred Dec 30, 2008.

[46] Inmet Mining Corporation, “Pyhäsalmi Mine”, introductory brochure.

[47] Johnson N.W., Munro P.D., “Overview of Flotation Technology and Plant Practice for Complex Sulphide Ores”, SME Mineral Processing Plant Design, Practice and Control Conference, Vancouver, Canada (Oct.), pp. 1097-1123, 2002.

[48] Kaartinen J., “Data acquisition and analysis system for mineral flotation”, Helsinki University of Technology, Control Engineering Laboratory, Finland, Report 126, 2001.

[49] Kaartinen J., Hätönen J., Miettunen J., Ojala O., "Image analysis based control of zinc flotation - A multi-camera approach", ICARCV 2002 7th International Conference on Control, Automation, Robotics and Vision, Singapore, 2-5 December, 2002, IEEE, 6 pp.

[50] Kaartinen J., Roine T., Hätönen J., "Machine Vision of Flotation Froths with a Rapid-Prototyping Platform", Workshop on Automation in Mining, Mineral and Metal Industry (IFACMMM2009), Viña del Mar, Chile, 14-16 October, 2009, (accepted).

[51] Kaartinen J., Tolonen A., "Particle Size Measurement of Crushed Ore Using 3D-Profile Measurement", Machine Vision News, Vol 12, 2007.

[52] Kim H., Haas C. T., Rauch A. F., Browne G.,"Dimensional Ratios for Stone Aggregates from Three-Dimensional Laser Scans", Journal of Computing in Civil Engineering, Vol. 16, Issue 3, 2002, pp. 175-183.

[53] King, R.P., "The Principles of Flotation", S. Afr. I.M.M., 1982.

[54] Knowledge Scape - PlantVision for Feed Belts, <http://www.kscape.com/downloads/PlantVision%20for%20Feed%20Belts.pdf>, referred Dec 30, 2008.

[55] Knowledge Scape - PlantVision for Feed Flotation, <http://www.kscape.com/downloads/PlantVision%20for%20Flotation.pdf>, referred Dec 30, 2008.

[56] Kongas M., "Mineral slurry on-stream particle size analysis", Filtration+Separation, Sep. 2003, pp. 36–37.

[57] Kuopanportti H., Roikola H., Suorsa T., "Use of froth characteristics in modeling the flotation process. Part I: Model for fine zinc particles", In Proceedings of flotation 2000, Adelaide, Australia, 2000.

[58] Kuopanportti H., Roikola H., Suorsa T., "Use of froth characteristics in modeling the flotation process. Part II: Model for coarse and intermediate zinc particles", IFAC Workshop 22- 24 August 2000, Finland.

[59] Kwan A.K.H., Mora C.F., Chan H.C., "Particle shape analysis of coarse aggregate using digital image processing", Cement and Concrete Research 29, 1999, pp. 1403–1410.

[60] Larinkari, M., "Particle Size Distribution of Crushed Ore - Measurement and Management", Master's thesis, Helsinki University of Technology, 2004.

[61] Larinkari M., Kaartinen J., Hyötyniemi H., "Management of particle size distribution of crushed ore", Process Systems '05, Cape Town, South Africa, November 10-11, 2005.

[62] Latham J-P., Kemeny J., Maerz N., Noy M., Schleifer J., Tose S., "A Blind Comparison Between Results of Four Image Analysis Systems Using a Photo-Library of Piles of Sieved Fragments", Fragblast, Vol. 7, Number 2, 2003, pp. 105-132.

[63] Lee J.R.J., Smith M.L., Smith L.N., "A new approach to the three-dimensional quantification of angularity using image analysis of the size and form of coarse aggregates", Engineering Geology, Vol. 91, Issues 2-4, 2007, pp. 254-264.

[64] Lee J.R.J., Smith M.L., Smith L.N., Midha P.S., "A mathematical morphology approach to image based 3D particle shape analysis", Machine Vision and Applications, Vol. 16, No. 5, 2005, pp. 282–288.

[65] Lin B., Recke B., Knudsen J. K.H., Jorgensen S. B., "Bubble size estimation for flotation processes", Minerals Engineering, Vol. 21, Issue 7, June 2008, pp. 539-548.

[66] Lorber A., Wangen L. E., Kowalski B. R., "A Theoretical Foundation for the PLS Algorithm", J. Chemometrics, 1(19), 1987.

[67] Maerz N. H., "Technical and Computational Aspects of the Measurement of Aggregate Shape by Digital Image Analysis", J. Comp. in Civ. Engrg., Vol. 18, Issue 1, pp. 10-18, 2004.

[68] Maerz, N. H., Palangio, T. C., Franklin. J. A., “WipFrag image based granulometry system”, In Proc. FRAGBLAST 5 Workshop on Measurement of Blast Fragmentation, Quebec, 1996, pp. 91-99.

[69] Martens H., Næs T., “Multivariate Calibration”, John Wiley & Sons, New York, 1989.

[70] Marx T., “Optimization of mineral processes by applying on-line analysis together with expert systems”, a presentation given at Finn Materia 2008 congress, Jyväskylä, Finland, November 13-14, 2008.

[71] McKee, D.J., Chitombo, G.P., Morrell, S., “The relationship between fragmentation in mining and comminution circuit throughput”, Minerals Engineering, 1995, 8, No. 11, pp. 1265-1274.

[72] Miettunen J., Kaartinen J., Hätönen J., "Image analysis based control of zinc flotation", Regional APCOM 2001, Tampere, Finland, 3-5 September, 2001, pp. 267-275.

[73] Moolman D.W., Aldrich C., Van Deventer J.S.J., Bradshaw D.B., "The characterisation of froth surfaces and relation to process performance by using connectionist image processing techniques", Mineral Engineering, 8 (1-2), 1995, pp. 23-30.

[74] Moolman D.W., Aldrich C., Deventer J. V., Bradshaw D., "The interpretation of flotation froth surfaces by using digital image analysis and neural networks", Chemical Engineering Science, 50(22), 1995, pp. 3501–3513.

[75] Moolman D.W., Aldrich C., van Deventer J.S.J., Stange W.W., "The classification of froth structure in a copper flotation plant by means of a neural net", International Journal of Mineral Processing 43, 1995, pp. 193–208.

[76] Moolman D.W., Aldrich C., Schmitz G.P.J., van Deventer, J.S.J., "The interrelationship between surface froth characteristics and industrial flotation performance", Minerals Engineering 9 (8), 1996, pp. 837–854.

[77] Moolman D.W., Eksteen J.J., Aldrich C., van Deventer J.S.J., "The significance of flotation froth appearance for machine vision control", International Journal of Mineral Processing 48, 1996, pp. 135–158.

[78] Mora C.F., Kwan, A.K.H., "Sphericity, shape factor, and convexity measurement of coarse aggregate for concrete using digital image processing", Cement and Concrete Research 30, 2000, pp. 351–358.

[79] Morar S. H., Forbes G., Heinrich G. S., Bradshaw D. J., King D., Adair B. J. I., Esdaile L., "The use of a colour parameter in a machine vision system, Smart-Froth, to evaluate copper flotation performance at Rio Tinto's Kennecott Utah Copper Concentrator", In Centenary of Flotation Symposium, Brisbane, Queensland, 2005, pp. 147–151.

[80] Niemi, A.J., Ylinen, R., Hyötyniemi, H., "On characterization of pulp and froth in cells of flotation plant", International Journal of Mineral Processing 51, 1997, pp. 51–65.

[81] Oestreich J. M., Tolley W. K., Rice D. A., "The development of a color sensor system to measure mineral compositions", Minerals Engineering, Vol. 8, Issues 1-2, 1995, pp. 31-39.

[82] Outotec Courier® 6 SL - The high performance XRF on-stream slurry analyzer, Introductory brochure, <http://www.outotec.com/36260.epibrw>, referred Jan 8, 2009.

[83] Outotec FrothMaster™ 2, Introductory brochure, <http://www.outotec.com/37093.epibrw>, referred Dec 31, 2008.

[84] Pietilä J., Haavisto O., "Reflectance Spectrum Based Classification of Ore", Workshop on Automation in Mining, Mineral and Metal Industry (IFACMMM2009), Viña del Mar, Chile, 14-16 October, 2009, (accepted).

[85] Qin S., "Partial least squares regression for recursive system identification", In: Proceedings of the 32nd Conference on Decision and Control, San Antonio, Texas, USA, 1993, pp. 2617–2622.

[86] Qin S., "Recursive pls algorithms for adaptive data modeling", Computers and Chemical Engineering 22 (4/5), 1998, pp. 503–514.

[87] Rao, S.R., "Surface Chemistry of Froth Flotation", 2nd edition, Kluwer Academic/Plenum Publishers, New York, 2004.

[88] Reyneke L., Du Plessis F.E., van der Westhuizen G., "Development and Evaluation of Technology for Quantifying the Mineral Composition of Process Streams in a Typical Dry Mill in the Heavy Mineral Industry", Heavy Minerals 2003, Johannesburg, South African Institute of Mining and Metallurgy, 2003.

[89] Roine T., "Laser Triangulation Based Froth Level Measurement in Improving Image Analysis of Flotation Process", Helsinki University of Technology, Upcoming Master's thesis work.

[90] Runge K., McMaster J., Wortley M., Rosa D. L., Guyot O., "A correlation between visiofroth measurements and the performance of a flotation cell", In Ninth Mill Operator's Conference, Fremantle, Western Australia, 2007, pp. 19-21.

[91] Salinas, R.A., Raff, U., Farfan, C., "Automated estimation of rock fragment distributions using computer vision and its application in mining", IEE Proc. –Vis. Image Signal Process., 2005, 152, No. 1, pp.1-8.

[92] Saloheimo K., Outotec Minerals Oy, Private communication in a project meeting in Pyhäsalmi, January 15th 2007.

[93] Sanchidrián J. A., Segarra P., Ouchterlony F., López L. M., "On the accuracy of fragment size measurement by image analysis in combination with some distribution functions", Rock Mechanics and Rock Engineering, DOI:10.1007/s00603-007-0161-8, Springer Wien, 2008.

[94] Schleifer, J., Tessier, B., "Fragscan: A tool to measure fragmentation of blasted rock", Proc., FRAGBLAST-5 Workshop on Measurement of Blast Fragmentation, Montreal, Quebec, Canada, 1996, pp. 73-78.

[95] Schleifer, J., Tessier, B., "Fragmentation assessment using the Fragscan system: quality of a blast", In: Explo, 2001. Explosives in Mining Conference, AusIMM, Hunter Valley, NSW, Australia, 2001, pp. 365–372.

[96] Sick AG, "LMS400 Laser Measurement System - Operating Instructions", 2005.

[97] Siemens Milltronics Process Instruments Inc., "Milltronics Accumass BW100 - Instruction Manual PL-531", January 2001.

[98] Sirén A., "VTT's report for the tasks 1.2, 1.3 and 1.4", EU Esprit LTR Project Number 24931, November 15, 1999.

[99] Soille P., "Morphological image analysis: Principles and applications", Springer-Verlag, 1999, pp. 170-171.

[100] Sonka M., Hlavac V., Boyle R., "Image processing, analysis and machine vision", Brooks/Cole Publishing Company, 2nd. ed., 1998, ISBN 0-534-95393-X.

[101] Sony Inc., "Sony XC-55 Application Guide", 2003.

[102] Specim Imspector - Imaging Spectrographs, Introductory brochure, <http://www.specim.fi/media/pdf/product-brochures/imspector-series-ver2-08.pdf>, referred Jan 9, 2009.

[103] Supomo A., Yap E., Zheng X., Banini G., Mosher J., Partanen A., "PT Freeport Indonesia's mass-pull control strategy for rougher flotation", Minerals Engineering, Vol. 21, Issues 12-14, November 2008, pp. 808-816.

[104] Sutherland, K.L., Wark, I.W., "Principles of Flotation", Australian IMM, 1955.

[105] Thurley, M.J., "Three dimensional data analysis for the separation and sizing of rock piles in mining", Doctoral thesis, Monash University, Electrical & Computer Systems Engineering, 2002.

[106] Thurley, M.J., Andersson, T., "An industrial 3D vision system for size measurement of iron ore green pellets using morphological image segmentation", Minerals Engineering, Vol. 21, Issue 5, April 2008, pp. 405-415.

[107] Ylinen R., Miettunen J., Molander M., Siliämaa E-R., "Vision- and model-based control of flotation", IFAC Workshop 22-24 August 2000, Finland

[108] van Olst M., Brown M., Bourke P., Ronkainen S., "Improving flotation plant performance at Cadia by controlling and optimising the rate of froth recovery using Outokumpu Frothmaster™", In Proceedings of the AusIMM seventh mill operators' conference, Melbourne, Australia, 2000.

[109] Wikipedia – Mining, <http://en.wikipedia.org/wiki/Mining>, referred Jan 10, 2009.

[110] Wills, B.A., Napier-Munn, T.J., "Will's Mineral Processing Technology", Seventh Edition, Butterworth-Heinemann, 2006.

[111] Vincent L., Soille P., "Watersheds in digital spaces: An efficient algorithm based on immersion simulations", IEEE Transactions on Pattern Analysis and Machine Intelligence, Vol. 13 No. 6, June 1991, pp 583-598.

[112] WipWare Application Brochure, <www.wipware.com/ download/public/Application%20Brochure.pdf>, referred Dec 31, 2008.

[113] Wise Barry M., Gallagher Neal B., "PLS_Toolbox 2.0 for use with MATLAB™", Eigenvector Research Inc., 1998.

[114] Wold H., "Soft modeling with latent variables: the nonlinear iterative partial least squares approach", In Gani J. (ed.): Perspectives of probability and statistics: Papers in honour of M. S. Barlett, Academic Press, London, pp. 114-142. 1975.

[115] Wold S., Geladi P., Esbensen K., Ohman J., "Multi-Way Principal Components and PLS-Analysis", J. Chemometrics, Vol. 1, 1987, pp. 41-56.

[116] Wold S., Kettaneh-Wold N., Skagerberg B., "Nonlinear PLS modeling", Chemom. Intell. Lab. Syst., Vol. 7, 1989, pp. 53-65.

[117] Woodburn E.T., Stockton J.B., Robbins D.J., "Vision-based characterization of three-phase froths", International Colloquium – Developments in Froth Flotation, vol. 1. South African Institute of Mining and Metallurgy, Gordon's Bay, South Africa, 1989, pp. 1–30.

Appendix: Publications

HELSINKI UNIVERSITY OF TECHNOLOGY CONTROL ENGINEERING

Editor: H. Koivo

Report 147 Mohamed, F.
Microgrid Modelling and Simulation. March 2006.

Report 148 Mäenpää, T.
Robust Model Predictive Control for Cross-Directional Processes. May 2006.

Report 149 Kantola, K.
Modelling, Estimation and Control of Electroless Nickel Plating Process of Printed Circuit Board Manufacturing. March 2006.

Report 150 Virtanen, T.
Fault Diagnostics and Vibration Control of Paper Winders. June 2006.

Report 151 Hyötyniemi, H.
Neocybernetics in Biological Systems. August 2006.

Report 152 Hasu, V.
Radio Resource Management in Wireless Communication: Beamforming, Transmission Power Control, and Rate Allocation. June 2007.

Report 153 Hrbček, J.
Active Control of Rotor Vibration by Model Predictive Control - A simulation study. May 2007.

Report 154 Mohamed, F. A.
Microgrid Modelling and Online Management. January 2008.

Report 155 Eriksson, L., Elmusrati, M., Pohjola, M. (eds.)
Introduction to Wireless Automation - Collected papers of the spring 2007 postgraduate seminar. April 2008.

Report 156 Korkiakoski, V.
Improving the Performance of Adaptive Optics Systems with Optimized Control Methods. April 2008.

Report 157 Al.Towati, A.
Dynamic Analysis and QFT-Based Robust Control Design of Switched-Mode Power Converters. September 2008.

Report 158 Eriksson, L.
PID Controller Design and Tuning in Networked Control Systems. October 2008.

Report 159 Pohjoranta, A.
Modelling Surfactant Mass Balance with the ALE Method on Deforming 2D Surfaces. May 2009.

Report 160 Kaartinen, J.
Machine Vision in Measurement and Control of Mineral Concentration Process. June 2009.

ISBN 978-951-22-9954-6

ISSN 0356-0872

Yliopistopaino, Helsinki 2009